

A Survey of Underwater Wireless Optical Communication

by

Zhaoquan Zeng

B.Eng., Tianjin University, P. R. China, 2013

A THESIS SUBMITTED IN PARTIAL FULFILLMENT OF
THE REQUIREMENTS FOR THE DEGREE OF

MASTER OF APPLIED SCIENCE

in

THE COLLEGE OF GRADUATE STUDIES

(Electrical Engineering)

THE UNIVERSITY OF BRITISH COLUMBIA

(Okanagan)

December 2015

© Zhaoquan Zeng, 2015

Abstract

Underwater wireless communication refers to transmitting data in unguided water environment through the use of wireless carriers, i.e., radio-frequency wave, acoustic wave, and optical wave. We focus, in this thesis, on the underwater wireless optical communication (UWOC) that employs optical wave as the transmission carriers. In comparison to RF and acoustic counterparts, UWOC has a much higher transmission bandwidth, thus providing much higher data rate. Due to this high-speed transmission advantage, UWOC has attracted considerable attention in recent years. Many potential applications of UWOC systems have been proposed for environmental monitoring, offshore exploration, disaster precaution, and military operations. However, UWOC systems also suffer from severe absorption and scattering introduced by underwater channel. In order to overcome these technical challenges, several new system design approaches, which are different from the conventional terrestrial free-space optical communication, have been explored in recent years. In this thesis, we provide a comprehensive survey of the state-of-the-art of UWOC research in three aspects: channel characterization, channel modulation and coding techniques, and practical implementations of UWOC. Based on the comprehensive understanding of UWOC, we also investigate the outage performance for vertical buoy-based UWOC with pointing errors. Closed-form outage probability with zero boresight pointing errors and outage probability bounds with nonzero boresight pointing errors have been derived.

Table of Contents

Abstract	ii
Table of Contents	iii
List of Tables	vi
List of Figures	vii
List of Acronyms	ix
List of Symbols	xiii
Acknowledgements	xiv
Dedication	xv
Chapter 1: Introduction	1
1.1 Overview of Underwater Wireless Optical Communication	1
1.2 Advantages and Challenges of UWOC	7
1.3 Thesis Organization and Contributions	9
Chapter 2: UWOC Channel Modeling	12
2.1 Light Propagation in Water	12
2.2 Modeling of Aquatic Optical Attenuation in UWOC	20
2.2.1 Aquatic Optical Attenuation in LOS Configuration	20
2.2.2 Aquatic Optical Attenuation in NLOS Configuration	25
2.3 Modeling Geometric Misalignment of UWOC	26
2.4 Modeling Link Turbulence of UWOC	28
2.5 Summary	29

Chapter 3: UWOC Channel Modulation and Coding Techniques	31
3.1 Modulation Schemes of UWOC	31
3.2 Channel Coding of UWOC	35
3.3 Summary	37
Chapter 4: Experimental Setups and Prototypes of UWOC	39
4.1 Typical LOS/NLOS UWOC systems	39
4.2 Retroreflectors in UWOC	43
4.3 Smart Transceivers of UWOC	45
4.4 UWOC for Underwater Vehicles	47
4.5 Hybrid Acoustic/Optical UWC Systems	48
4.6 Summary	52
Chapter 5: Outage Performance for Underwater Wireless Optical Links With	
Pointing Errors	54
5.1 Pointing Errors Models	54
5.1.1 Pointing Errors Model with Zero Boresight	54
5.1.2 Pointing Errors Model with Nonzero Boresight	59
5.2 Beam Spread Function	60
5.3 Outage Probability with Zero Boresight Pointing Errors	62
5.4 Bounds of Outage Probability with Nonzero Boresight Pointing Errors	63
5.4.1 Lower Bound of Outage Probability with Nonzero Boresight	64
5.4.2 Upper Bound of Outage Probability with Nonzero Boresight	66
5.4.3 Discussion on the Tightness of the Outage Probability Bounds	68
5.5 Numerical Results	70
5.5.1 Outage Probability with Zero Boresight Pointing Errors	70
5.5.2 Outage Probability Bounds with Nonzero Boresight Pointing Errors	73
5.6 Summary	75
Chapter 6: Conclusions	76
6.1 Summary of Contributions	76
6.2 Suggested Future Work	77
Bibliography	80

TABLE OF CONTENTS

Appendix	100
Appendix A:	101
Appendix B:	102

List of Tables

Table 1.1	Comparison of underwater wireless communication technologies [1].	10
Table 2.1	Summary of absorption and scattering characteristics of seawater [2]	18
Table 2.2	Typical values of $a(\lambda)$, $b(\lambda)$, and $c(\lambda)$ for different water types	19
Table 2.3	Summary of literatures on UWOC channel modeling	30
Table 3.1	Summary of literatures on UWOC modulation schemes	38
Table 3.2	Summary of literatures on UWOC channel coding	38
Table 4.1	Summary of literatures on experimental setups and prototypes of UWOC . . .	53
Table 5.1	Summary of simulation parameters	70

List of Figures

Figure 1.1	The “transparent window” for light aquatic attenuation is shown with blue and green color. Please refer to the colored version of this thesis. Figure 1.1 is adapted from [3].	3
Figure 1.2	An underwater wireless sensor network with aerospace and terrestrial communication. Figure 1.2 is adapted from [4].	4
Figure 1.3	Link configurations of UWOC.	5
Figure 2.1	Geometry of inherent optical properties for a volume ΔV . Figure 2.1 is adapted from [5].	13
Figure 2.2	Optical absorption spectra for different ocean components. The data in Figure 2.2 is from [6–8].	16
Figure 2.3	Optical scattering spectra for different ocean components. The data in Figure 2.3 is from [6–8].	17
Figure 3.1	Illustration of OOK, PWM, PPM and DPIM. Figure 3.1 is adapted from [9].	32
Figure 4.1	A typical laboratory LOS UWOC system based on intensity-modulation direct-detection (IM/DD) technique.	40
Figure 4.2	Demonstration of corner and spherical retroreflectors.	44
Figure 4.3	Modulating retroreflector link.	44
Figure 4.4	Two types of hybrid acoustic/optical UWC links.	50
Figure 5.1	Comparison between corrected and non-corrected PDF of ocean slopes. . . .	56
Figure 5.2	Geometry of the buoy-based UWOC. Figure 5.2 is adapted from [10]. . . .	57
Figure 5.3	PDF of Hoyt distributed radial displacement r with $L = 5m$ and different values of wind speed U	58
Figure 5.4	PDF of Beckmann distributed radial displacement r with $\mu_x = 0.01$, $\mu_y = 0.02$, $L = 5m$ and different values of wind speed U	59

LIST OF FIGURES

Figure 5.5	Geometry for BSF.	60
Figure 5.6	BSF results for $L = 3.63m$ with different attenuation coefficients c . Model results shown as lines. Experimental data shown as points. Relative intensity is the received power with displacement r normalized by the power without displacement $B(L, r)/B(L, 0)$ [11]. Figure 5.6 is reprinted from [11].	61
Figure 5.7	BSF values for $L = 5m$ and $c = 0.3$ with different values of transmission power P_t	61
Figure 5.8	Demonstration of outage region.	63
Figure 5.9	Integrating region for lower bound of outage probability.	64
Figure 5.10	Coordinates of n th circumscribed rectangle on the upper semicircle.	64
Figure 5.11	Divide half of the non-outage region into several rectangles with the same height.	66
Figure 5.12	Coordinates of n th inscribed rectangle on the upper semicircle.	67
Figure 5.13	Demonstration of the area $S_{shade} = \sum 2(S_{LB} - S_{UB})$. A factor of 2 indicates the symmetry of rectangle area in lower and upper semicircles.	69
Figure 5.14	Outage probability of a vertical buoy-based UWOC system with zero boresight pointing errors. Link distance $L = 5m$	71
Figure 5.15	Outage probability of a vertical buoy-based UWOC system with zero boresight pointing errors. Link distance $L = 10m$	72
Figure 5.16	Outage probability and its bound with nonzero boresight pointing errors. $\mu_x = 0.01$, $\mu_y = 0.02$, $U = 2m/s$, $c = 0.3m^{-1}$, $L = 5m$, $D = 5cm$, $\gamma_{th} = 0.01$	74

List of Acronyms

Acronyms	Definitions
AMOUR	Autonomous Modular Optical Underwater Robot
AOPs	Apparent Optical Properties
APD	Avalanche Photodiode
AUVs	Autonomous Underwater Vehicles
BCH	Bose-Chaudhuri-Hocquenghem
BER	Bit-Error Rate
BPSK	Binary Phase-Shift Keying
CDMA	Code Division Multiplexing Access
CDOM	Colored Dissolved Organic Material
CORK-OTS	Circulation Obviation Retrofit Kit Optical Telemetry System
CRC	Cyclic Redundancy Check
CSAIL	Computer Science and Artificial Intelligence Laboratory
DPIM	Digital Pulse Interval Modulation
DPPM	Differential Pulse Position Modulation
DPSK	Differential Phase-Shift Keying
DT	Dynamic Threshold
FEC	Forward Error Correction
FOV	Field of View
FSO	Free Space Optical

Gbps	Gigabit per Second
GMSK	Gaussian Minimum Shift Keying
HDL	Hardware Description Language
HG	Henry-Greenstein
IM/DD	Intensity Modulation/Direct Detection
IOPs	Inherent Optical Properties
ISI	Inter Symbol Interference
Kbps	Kilobit per Second
LD	Laser Diode
LDPC	Low-Density Parity-Check
LED	Light-Emitting Diode
LOS	Line-of-Sight
LT	Luby Transform
MAC	Medium Access Control
Mbps	Megabit per Second
MEMS	Micro-Electromechanical System
MIMO	Multiple-Input Multiple-Output
MIT	Massachusetts Institute of Technology
ML	Maximum Likelihood
MPPM	Multi-Pulse Pulse Position Modulation
NLOS	Non-Line-of-Sight
NRL	Naval Research Laboratory
NRZ-OOK	Non-Return-to-Zero On-Off Keying
OFDM	Orthogonal Frequency-Division Multiplexing
OOK	On-Off Keying

OOK	On-Off Keying
OWC	Optical Wireless Communications
PC	Personal Computer
PDF	Probability Density Function
PIN	Positive-Intrinsic-Negative
PolSK	Polarization Shift Keying
PPM	Pulse Position Modulation
P-PPM	Polarized- Pulse Position Modulation
PSK	Phase-Shift Keying
PWM	Pulse Width Modulation
QAM	Quadrature Amplitude Modulation
QPSK	Quadrature Phase-Shift Keying
RF	Radio Frequency
RF-EM	Radio-Frequency Electromagnetic
ROVs	Remotely Operated Underwater Vehicles
RS	Reed-Solomon
RTE	Radiative Transfer Equation
RZ-OOK	Return-to-Zero On-Off Keying
SIM	Subcarrier Intensity Modulation
SIMO	Single-Input Multiple-Output
SISO	Single-Input Single-Output
SNR	Signal-to-Noise Ratio
SPF	Scattering Phase Function
TDMA	Time Division Multiplexing Access
UTROV	Untethered ROV

List of Acronyms

UWC	Underwater wireless communication
UWOC	Underwater Wireless Optical Communication
UWSNs	Underwater Wireless Sensor Networks
VSF	Volume Scattering Function

List of Symbols

Symbols	Definitions
$a(\lambda)$	The absorption coefficient
$b(\lambda)$	The scattering coefficient
$c(\lambda)$	The attenuation coefficient
$I_0(\cdot)$	The modified Bessel function of the first kind
$J_0(\cdot)$	The Bessel function of the first kind with order 0
$p(\cdot)$	The Hankel transform
$\text{erf}(x)$	The error function
$Q_1(\cdot, \cdot)$	The first order Marcum Q -function
$\ln(\cdot)$	The log function with base e
\lim	The limit of function
$ \cdot $	The absolute value of the argument
∇	The divergence operator

Acknowledgements

I am deeply grateful to my thesis supervisor Dr. Julian Cheng for his enthusiasm, guidance, advice, encouragement, support, and friendship. I will continue to be influenced by his rigorous scholarship, clarity in thinking, and professional integrity.

I owe many people for their generosity and support during my master study at the University of British Columbia. I would like to thank my dear colleagues for sharing their academic experiences and constructive viewpoints generously with me during our discussions. I would also like to thank my dear friends for sharing my excitement and encouraging me when I was in frustration during this journey.

Finally, I would like to thank my parents for their patience, understanding, support, and love over all these years. All my achievements would not have been possible without their constant encouragement and support.

To My Loving Parents

Chapter 1

Introduction

1.1 Overview of Underwater Wireless Optical Communication

Two thirds of the earth's surface is covered with water. During the past thousands of years, humans have never stopped the exploration of the ocean. In recent years, with an increase of globe climate change and resource depletion of land, there has been a growing interest in the research of ocean exploration system. Underwater wireless communication (UWC) technology enables the realization of ocean exploration systems, and thus attracts more and more attention. UWC refers to transmitting data in an unguided water environment through the use of wireless carriers, i.e. radio-frequency (RF) waves, acoustic waves, and optical waves. Considering the limited bandwidth of RF and acoustic methods and the increasing need for high-speed underwater data transmission, underwater wireless optical communication (UWOC) has become an attractive and viable alternative. In fact, light has been used as a wireless communication method for thousands of years in various forms. For instance, the ancient Chinese used beacon towers in order to deliver military information around 1,000 BC, and the ancient Greek and Roman armies used polished shields to reflect sunlight for signaling around 800 BC. In 1880, Alexander Graham Bell developed a new wireless telephone system that used sunlight as the transmission medium. This system is regarded as the first optoelectronic communication system in the world [12, 13]. In the 1960s, the invention of laser as an ideal optical source has changed the future of optical wireless communication (OWC) [14]. From that time on, a flurry of terrestrial OWC applications appeared. But due to the severe attenuation effects of seawater to visible light and the limited knowledge of aquatic optics, the early development of UWOC was far behind the terrestrial free-space optical (FSO) communications.

Based on nearly 20 years experimental and theoretical study of light propagation in the sea, in 1963, Duntley proposed that seawater shows a relatively low attenuation property to light with wavelengths from 450nm to 550nm which corresponds to the blue and green spectrum (Figure 1.1) [15]. This finding was then experimentally confirmed by Gilbert *et al.* [16]. The existence of the blue-green light transmission “window” in water provides a foundation for the development

of future UWOC. The early applications of UWOC are mainly for military purpose, especially in the area of submarine communications. In 1976, Karp evaluated the feasibility of wireless optical communications between underwater and above surface (satellite) terminals [17]. In 1977, the researchers in the Lawrence Livermore Laboratory of the University of California proposed an one-way optical communication system from shore to submarine [18]. The transmitter of the UWOC system employed blue-green laser source to generate light pulses. It was flexible to be carried by a land vehicle or an airplane due to its compact architecture. The transmitter can also focus its output light beam on a relay satellite, which then reflects the beam to a submarine [18]. Other UWOC tests of the plane-to-submarine and satellite-to-submarine topologies were established by US and Russian navy during 1980s and 1990s [19]. Mixed optical communication links with about tens of kilometers FSO link and several tens of meters UWOC link were achieved.

Over the decades, the interest of UWOC is still limited to military applications [18, 20]. The massive market promotion of UWOC has not been achieved so far. Only a few limited UWOC products were commercialized in the early 2000s, such as the BlueComm UWOC system which can achieve 20 Mbps underwater data transmission over 200m distance, and the Ambalux UWOC system which can provide the same data transmission rate in a shorter range of 20m [21]. In order to satisfy the increasing demands for ocean exploration with efficient high bandwidth data transmission, researchers have proposed the concept of underwater wireless sensor networks (UWSNs). The proposal of UWSNs has greatly facilitated the development of UWOC. Thus the market of UWOC has begun to show a future promise. The basic UWSNs consist of many distributed nodes such as seabed sensors, relay buoys, autonomous underwater vehicles (AUVs) and remotely operated underwater vehicles (ROVs) (Figure 1.2). These nodes have capabilities to accomplish sensing, processing, and communication tasks that maintain the collaborative monitoring to the underwater environment [4]. In Figure 1.2, sensors located at the bottom of the seabed collect data and transmit via acoustic or optical links to the AUVs and ROVs. Then, AUVs and ROVs relay signals to ships, submarines, communication buoys and other underwater vehicles. Above the sea surface, the onshore data center processes data and communicates with satellite and ships through RF or FSO links.

Based on link configurations between the nodes in UWSNs, UWOC can be divided into four categories (Figure 1.3) [22]: a) Point-to-point line-of-sight (LOS) configuration, b) Diffused LOS configuration, c) Retroreflector-based LOS configuration, and d) Non-line-of-sight (NLOS) configuration.

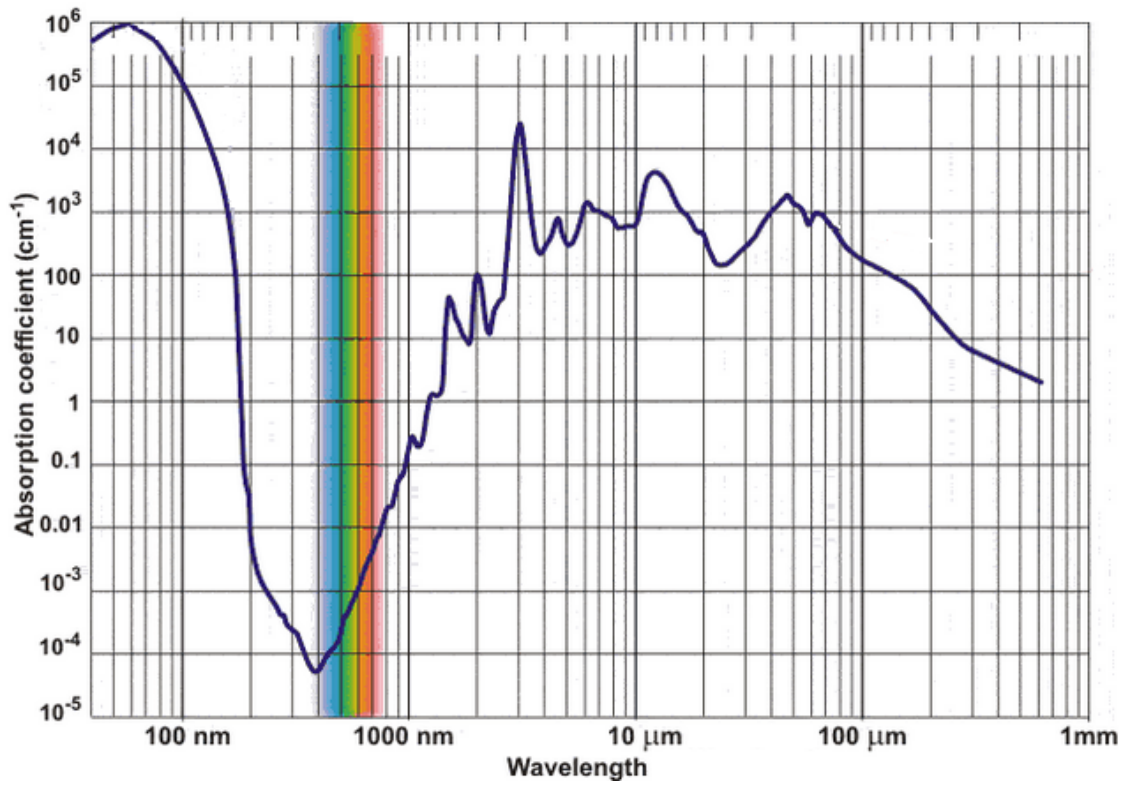


Figure 1.1: The “transparent window” for light aquatic attenuation is shown with blue and green color. Please refer to the colored version of this thesis. Figure 1.1 is adapted from [3].

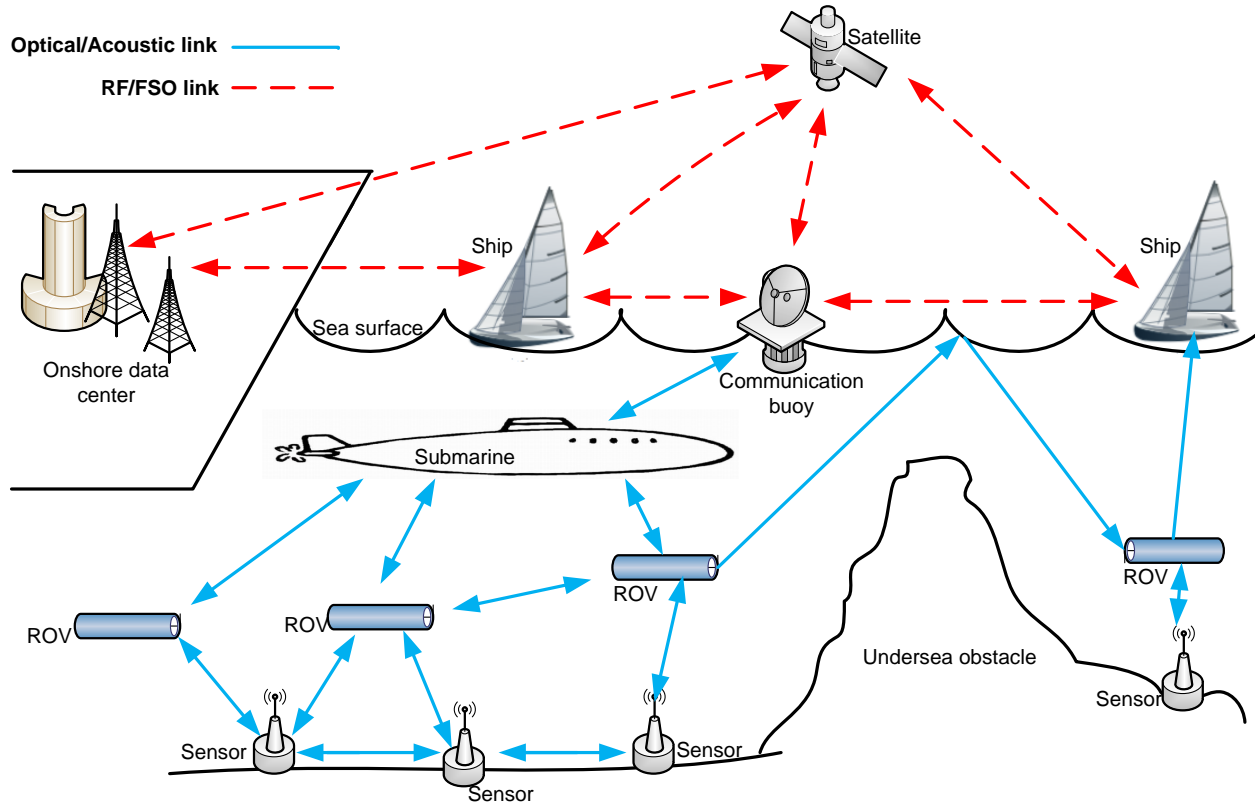
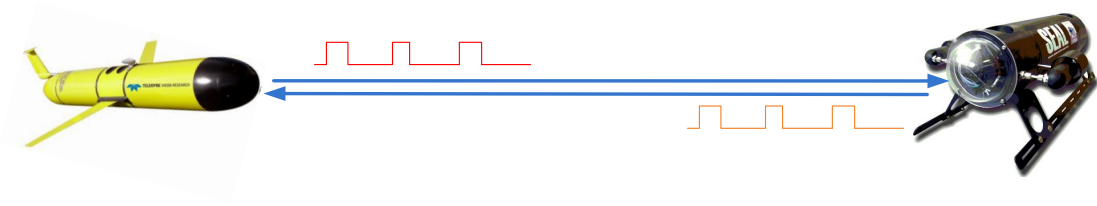
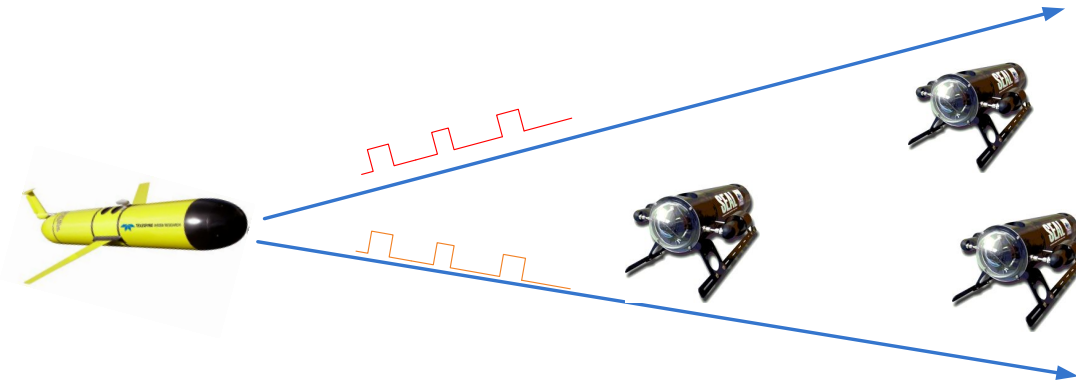


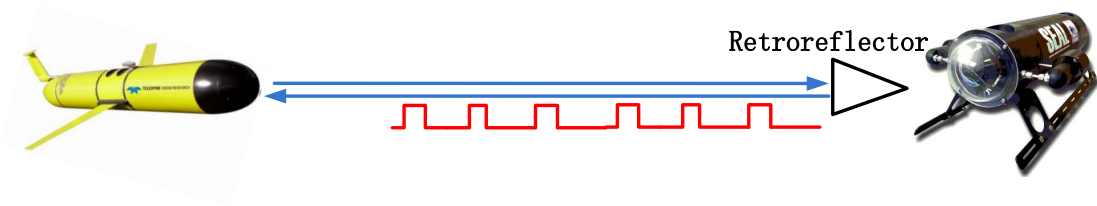
Figure 1.2: An underwater wireless sensor network with aerospace and terrestrial communication.
Figure 1.2 is adapted from [4].



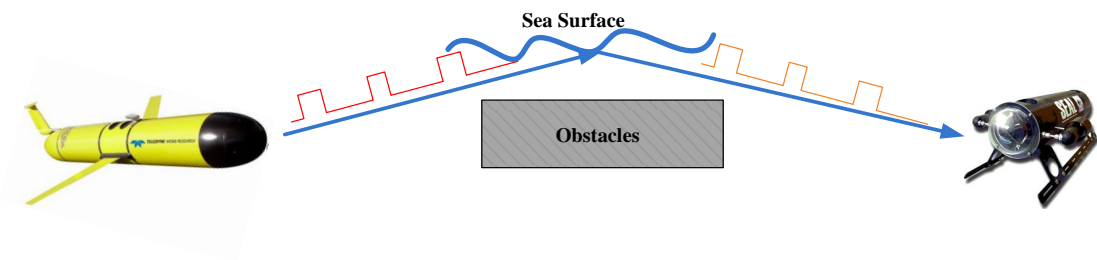
(a) Point-to-point LOS configuration.



(b) Diffused LOS configuration.



(c) Retroreflector-based LOS configuration.



(d) NLOS configuration.

Figure 1.3: Link configurations of UWOC.

- a) Point-to-point LOS configuration (Figure 1.3(a)) is the most commonly used link configuration in UWOC [23]. In point-to-point LOS configuration, the receiver detects the light beam in the direction of the transmitter. Since the point-to-point LOS UWOC system commonly employs light sources with a narrow divergence angle, such as a laser, it requires precise pointing between transmitter and receiver. This requirement will limit the performance of UWOC systems in turbid or turbulent water environments and then becomes a severe problem when the transmitter and the receiver are non-stationary nodes, such as AUVs and ROV [22].
- b) Diffused LOS configuration employs diffused light sources with large divergence angle such as high-power light-emitting diodes (LEDs) to accomplish broadcasting UWOC from one node to multiple nodes (Figure 1.3(b)). Broadcasting method can relax the requirement of precise pointing. However, compared with the point-to-point LOS configuration, the diffused-light based link suffers from aquatic attenuation due to the large interaction area with water. Relatively short communication distances and lower data rates are the two major limitations of this configuration.
- c) Retroreflector-based LOS configuration, as shown in Figure 1.3(c), can be regarded as one special implementation of point-to-point LOS configuration. This configuration is suitable for duplex UWOC systems having limited power and weight budget, such as an underwater sensor node. In modulating retro-reflector link, the transmitted light is reflected back from a modulated retro-reflector. During this process, the information that the retroreflector responses to the transceiver will be encoded on the reflected light. Since there is no laser or other light sources in the retroreflector end, its power consumption, volume and weight will be tremendously reduced. One limitation of this configuration is that the backscatter of the transmitted optical signal may interfere the reflected signal, thus degrading the system signal to noise ratio (SNR) and bit-error-rate (BER). Moreover, since the optical signals will go through the underwater channel twice, received signal will experience additional attenuation.
- d) NLOS configuration (Figure 1.3(d)) overcomes the alignment restriction of LOS UWOC. In this configuration, the transmitter projects the light beam to the sea surface with an angle of incidence greater than the critical angle, so that the light beam experiences a total internal reflection [24]. The receiver should keep facing the sea surface in a direction that is approximately parallel with the reflected light to ensure proper signal receiving. The major challenge of NLOS links is the random sea surface slopes induced by wind or other turbulence sources [25]. These undesirable phenomena will reflect light back to the transmitter and cause severe signal dispersion.

1.2 Advantages and Challenges of UWOC

UWOC systems are used for high speed underwater communications between multiple fixed or mobile nodes. They have great potential for applications in the UWSNs. Conventionally, there are three UWC choices for implementing UWSNs: acoustics, RF and optics [1]. In order to emphasize the unique advantages and characterizations of UWOC, we will compare the UWOC with RF and acoustic methods in the following of this section.

The acoustic method is the most widely used technology in UWC. It has a long application history that can be dated to late 1800s. After an extensive expansion of military applications during the two World Wars, underwater acoustic communication system has become a popular proven technology that has been applied to almost every aspect of UWSNs [26]. Considering the extreme broadness of ocean and the strong attenuation effect of seawater to other transmission sources like optical wave and RF wave, the most attractive advantage of underwater acoustic communication is that it can achieve a long link range up to several tens of kilometers [27]. Although acoustic method is the most popular method to achieve UWC, it also has certain intrinsic technical limitations. Firstly, since the typical frequencies associated with underwater acoustics are between 10 Hz and 1 MHz, the transmission data rate of acoustic link is relatively low (typically on the order of kbps) [4]. Secondly, due to the slow propagation speed of sound wave in water (about 1500m/s for 20 Celsius pure water), the acoustic link suffers from severe communication delay (typically in seconds). Thus it can't support applications which require real-time large volume data exchange. Thirdly, acoustic transceivers are usually bulky, costly and energy consuming. They are not economical for large scale UWSNs implementations [28]. Furthermore, acoustic technology can also impact marine life which uses sound waves in order to accomplish communication and navigation [29].

The underwater RF electromagnetic (EM) communication can be seen as an extension of the terrestrial RF-EM communication. The underwater RF communication has two major advantages. First, compared with acoustic wave and optical wave, the RF wave can perform a relatively smooth transition through air/water interface. This benefit can be used to achieve the cross-boundary communication which combines the terrestrial RF communication system and underwater RF-EM communication system together. Second, RF-EM method is more tolerant to water turbulence and turbidity than optical and acoustic methods [1]. The fatal limitation that impedes the development of underwater RF-EM method is its short link range. Since seawater that contains lots of salt is a conductive transmission media, the RF waves can only propagate a few meters at extra-low fre-

quencies (30-300Hz) [4]. Moreover, the underwater RF-EM systems also require huge transmission antenna and costly, energy-consuming transceivers.

Compared with the acoustic approach and RF-EM approach, UWOC has the highest transmission data rate, lowest link delay and the lowest implementation costs. UWOC can achieve a data rate on the order of Gbps over moderate distances of tens of meters. This high-speed advantage will guarantee the realization of many real-time applications such as underwater video transmission. Since the transmission speed of light in water is much higher than acoustic wave, UWOC links are immune to link latency. UWOC also has higher communication security over the acoustic and RF methods. Most UWOC systems are implemented in LOS configuration, rather than the diffused broadcasting scenario like acoustic and RF wave. It becomes more difficult to be eavesdropped. Furthermore, UWOC is much more energy efficient and cost-effective than its acoustic and RF counterparts. Instead of using large and expensive acoustic and RF transceivers which are highly energy consuming, relatively small and low-cost optical underwater transceivers, such as laser diodes and photo diodes, can be implemented in UWOC systems. This benefit can improve the large scale commercialization of UWOC, and accelerate the implementations of UWSNs.

Although UWOC enjoys many advantages over the acoustic and RF methods, achieving UWOC remains as a challenging task. The main challenges of UWOC are listed as follows.

- a) Optical signal suffers from severe absorption and scattering. Although the wavelength of transmission light has been carefully selected in the blue and green spectrum [15] to minimize the transmission attenuation coefficient, due to the inevitable photon interactions with the water molecules and other particulate matters in water, absorption and scattering still severely attenuate the transmitted light signal and cause multi-path fading. Due to the impact of absorption and scattering, UWOC suffers from poor BER performance over a few hundred meters link distance in turbid water environment. In underwater environment, matters such as chlorophyll are capable of absorbing the blue and red lights. These matters and other colored dissolved organic material (CDOM) can increase the turbidity of the water, and thus shrink the propagation distance of the light. Moreover, the concentration of CDOM will also change with ocean depth variations, thus change the corresponding light attenuation coefficients [30]. These undesirable impacts will increase the complexity of UWOC systems.
- b) Underwater optical links will be temporarily disconnected due to misalignment of optical transceivers. In several UWOC systems, blue/green lasers or LEDs have been implemented as the light

sources due to their narrow divergence feature; however, a precise alignment condition is required. As the underwater environment is turbulent at relatively shallow depths, link misalignment will take place frequently, especially in the vertical buoy-based surface-to-bottom UWOC applications. Random movements of sea surface will cause serious connectivity loss problem.

- c) Implementation of UWOC systems requires reliable underwater devices. The underwater environment is complex. The flow, pressure, temperature and salinity of seawater will strongly impact the performance and lifetime of UWOC devices. Considering that no solar energy can be exploited undersea and the long undersea operation time of UWOC devices, the reliability of device batteries and efficiency of device power consumption are critical.

In Table 1.1, we summarize the benefits and limitations of the three popular techniques choices to achieve UWC.

1.3 Thesis Organization and Contributions

This thesis contains six chapters. A summary of each chapter and its contributions are presented as follows.

Chapter 1 presents several background knowledge and recent development of UWOC. As the demand for high-speed underwater data transmission increases, UWOC becomes a promising alternative technology for underwater applications such as oil exploration and submarine communications. However, the optical signal suffers from severe intensity attenuation introduced by inevitable absorption and scattering effects of water. To overcome these limitations and improve the UWOC link performance, it is imperative to study the characterizations of underwater channel, optimal modulation and coding schemes, as well as the properties of transmission devices.

Chapter 2 focuses on the channel modeling of UWOC. Firstly, we introduce several basic properties of light propagation in water that constructs the fundamental of UWOC channel modeling. Secondly, we present and classify four comprehensive aspects of UWOC channel modeling: LOS aquatic attenuation, NLOS aquatic attenuation, link misalignment, and channel turbulence. In each aspect, detailed channel modeling method and representative research works have been demonstrated. Finally, we summarize the related literatures on the topic of UWOC channel modeling.

In Chapter 3, we study the channel modulation and coding techniques that can be applied in UWOC. Since most UWOC systems are based on intensity modulation and direct detection mechanisms, several conventional intensity modulation schemes, such as on-off keying and pulse

Table 1.1: Comparison of underwater wireless communication technologies [1].

UWC technologies	Benefits	Limitations
Acoustic	<ul style="list-style-type: none"> · Most widely used UWC technology · Long communication range up to 20 km 	<ul style="list-style-type: none"> · Low data transmission rate (on the order of kbps) · Severe communication latency (on the order of second) · Bulky, costly and energy consuming transceivers · Harmful to some marine life
RF	<ul style="list-style-type: none"> · Relatively smooth transition to cross air/water boundaries · More tolerant to water turbulence and turbidity · Loose pointing requirements · Moderate data transmission rate (up to 100 Mb/s) at very close distance 	<ul style="list-style-type: none"> · Short link range · Bulky, costly and energy consuming transceivers
Optical	<ul style="list-style-type: none"> · Ultra-high data transmission rate (up to Gbps) · Immune to transmission latency · Low cost and small volume transceivers 	<ul style="list-style-type: none"> · Can't cross water/air boundary easily · Suffers from severe absorption and scattering · Moderate link range (up to tens of meters)

position modulation, have been widely implemented in both theoretical and experimental UWOC research. Classic forward error correction technologies, such as the Reed-Solomon code and the Turbo code, have also been embedded into many UWOC systems. We will briefly introduce the characterizations of each modulation and coding schemes and demonstrate their applications in UWOC.

In Chapter 4, we study the recent development of experimental setups and prototypes of UWOC. Typical UWOC experimental testbeds that include different link configurations such as point-to-point LOS, diffused LOS, and NLOS are demonstrated. Besides these typical UWOC experiments, we also discuss several popular topics of experimental UWOC research which includes retroreflector-based UWOC, smart transceivers, UWOC for underwater vehicles and hybrid UWOC systems. At the end of this chapter, we also summarize and classify the contributions of experimental UWOC in recent years.

Chapter 5 studies the outage performance of vertical buoy-based UWOC links using intensity modulation/direct detection (IM/DD) on-off keying with zero and non-zero boresight pointing errors. A closed-form expression for the outage probability with zero boresight pointing errors is achieved. We also derive the closed-form bounds for the outage probability with non-zero boresight pointing errors.

Chapter 6 summarizes the entire thesis and states our contributions in this work. In addition, future work and potential research directions of UWOC are also suggested.

Chapter 2

UWOC Channel Modeling

In this chapter, we will firstly present background knowledge related to light propagation properties in the underwater environment. Then, UWOC channel modeling techniques, which include link attenuation modeling, geometric misalignment modeling, and turbulence modeling, will be presented. Finally, we will summarize this chapter and organize the related literatures in one table.

2.1 Light Propagation in Water

Compared with terrestrial FSO communication channels, UWOC channels have several unique characteristics. The existing terrestrial FSO channel models are not suitable for underwater environment; therefore, new reliable channel models must be proposed and studied. In order to derive new channel models for UWOC, we have to firstly understand the basic properties of light propagation in the underwater environment.

According to Mobley's statements in [5], the optical properties of water can be classified into two different groups: inherent optical properties (IOPs) and apparent optical properties (AOPs). IOPs can be understood as the optical parameters that only depend on the transmission medium itself, more specifically the composition of that medium and particulate substances present within it [22]. They are independent of the characterizations of light sources. The major IOPs of water are the absorption coefficient, the scattering coefficient, the attenuation coefficient, and the volume scattering function [31]. AOPs, on the other hand, are known as the optical parameters that depend not only on the the transmission medium itself, but also the geometrical structure of the light field such as diffusion and collimation [22]. The three major AOPs of water are radiance, irradiance and reflectance [31]. In a UWOC system, IOPs are typically used in determining communication link budgets, whereas AOPs are used to calculate ambient light levels for communication systems near the ocean surface [22]. Since IOPs have a greater impact on the link performance. In the rest of this section, we will focus on IOPs. The details of AOPs that include their definitions and measurements can be found in [5, 31–34].

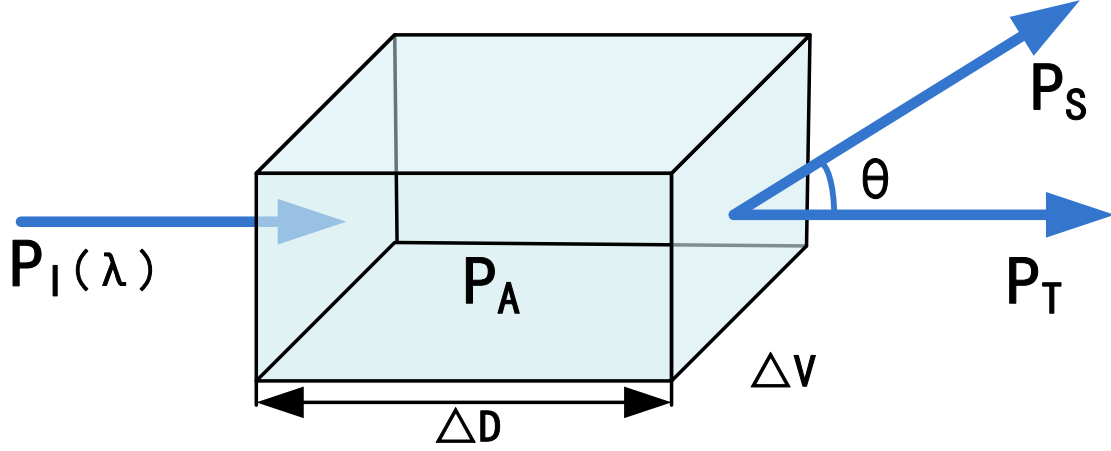


Figure 2.1: Geometry of inherent optical properties for a volume ΔV . Figure 2.1 is adapted from [5].

Absorption and scattering coefficients are the two major IOPs that determine the underwater light attenuation. Absorption is an energy transfer process in which photons lose their energy and convert it into other forms, such as heat and chemical (photosynthesis). Scattering is caused by variations in the refractive index that changes the propagation direction of photons [35]. Generally, the impacts of absorption and scattering to a UWOC system can cause three undesirable effects. First, in the presence of absorption, the total propagation energy of light is continuously decreasing, which will limit the link distance of the UWOC. Second, in the presence of scattering, since the size of optical aperture is finite, scattering will spread the light beam and result in a reduction of the number of photons collected by the receiver. This will lead to degradation of SNR of the system. Third, due to the light scattering in an underwater environment, each photon may arrive at the receiver panel in different time slots, and multi-path dispersions will occur. The undesirable impacts of multi-path phenomenon include inter symbol interference (ISI) and timing jitter.

In order to derive the absorption and scattering coefficients mathematically, we introduce the simple model in Figure 2.1. We assume that a volume of water ΔV with thickness ΔD is illuminated by a collimated light beam with wavelength λ . We denote the power of incident light as P_I . A portion of the incident light power P_A is absorbed by water, and another portion of light power P_S ¹ is scattered. P_T is the remaining light power that will propagate as desired. According to the law

¹The reflected light component is included in P_S .

of conservation, we get [5, 36]

$$P_I = P_A + P_S + P_T. \quad (2.1)$$

Based on (2.1), we define the ratio between absorbed power and incident power $\frac{P_A}{P_I}$ as absorbance. Similarly, the fraction between scattered power and incident power $\frac{P_S}{P_I}$ as scatterance. The subsequent absorption coefficient and scattering coefficient are then calculated by taking the limit of absorbance and scatterance as water thickness ΔD becomes infinitesimally small [5, 36]

$$a(\lambda) = \lim_{\Delta D \rightarrow 0} \frac{P_A}{P_I \Delta D}, \quad (2.2)$$

$$b(\lambda) = \lim_{\Delta D \rightarrow 0} \frac{P_S}{P_I \Delta D}. \quad (2.3)$$

In underwater optics, the overall attenuation effects of absorption and scattering can be described by the attenuation coefficient ² $c(\lambda)$ which can be expressed as [38]

$$c(\lambda) = a(\lambda) + b(\lambda). \quad (2.4)$$

The unit of attenuation coefficient is m^{-1} . In addition, the author of [2] states that the underwater light absorption coefficient can be further represented as the summation of four absorption factors [2]

$$a(\lambda) = a_w(\lambda) + a_{CDOM}(\lambda) + a_{phy}(\lambda) + a_{det}(\lambda) \quad (2.5)$$

where $a_w(\lambda)$ is the absorption due to pure seawater, $a_{CDOM}(\lambda)$ is the absorption due to CDOM, $a_{phy}(\lambda)$ denotes the absorption due to phytoplankton, and $a_{det}(\lambda)$ represents the absorption due to detritus.

The absorption effect of pure seawater is introduced from two sources: the water molecules and dissolved salt in water such as NaCl, MgCl₂, Na₂SO₄, and KCl [39]. Pure seawater is absorptive except around a 400nm-500nm window, the blue-green region of the visible light spectrum. The corresponding absorption spectrum of pure seawater is shown in Figure 2.2(a).

CDOM ³ refers to colored dissolved organic materials with dimensions smaller than 0.2 mm [40]. In Figure 2.2(b), it shows that the CDOM presents highly absorptive to blue wavelengths (420nm-450nm) and less absorptive to yellow and red light [41].

The absorption effects due to phytoplankton are mainly caused by photosynthesising of chlorophyll. For different phytoplankton species, the characteristics of the absorption effect are also

²Also known as extinction coefficient in some optical literatures such as [5, 37]

³In several optical literatures, it's also represented as gelbstoff, yellow substances or gilvin.

different [42]. Figure 2.2(c) shows a typical absorption coefficient profile shared by all species. We can observe that the $a_{phy}(\lambda)$ shows a high absorption in the 400-500 nm region and a further peak at about 660 nm.

Detritus includes living organic particles, such as bacteria, zooplankton, detrital organic matter and suspended inorganic particles such as quartz and clay. These substances are grouped together due to their similar absorption behaviour [43]. Figure 2.2(d) shows a absorption curve similar to that of CDOM.

The scattering coefficient for underwater light propagation can also be presented as a summation of different scattering factors

$$b(\lambda) = b_w(\lambda) + b_{phy}(\lambda) + b_{det}(\lambda) \quad (2.6)$$

where $b_w(\lambda)$ is the scattering due to pure seawater, $b_{phy}(\lambda)$ denotes the scattering due to phytoplankton, and $b_{det}(\lambda)$ represents the scattering due to detritus. Compared with absorption, scattering is relatively independent of wavelength. The dominant factor that impacts scattering is the density of particulate matters.

In pure seawater, since the refractive index will change with the variations of flow, salinity and temperature, the scattering coefficient will also change. Compared with the size of water molecules, the wavelength of light is relatively large, thus the Rayleigh scattering model can be used to describe the scattering induced by pure seawater. The corresponding scattering spectra is shown in Figure 2.3(a).

Phytoplankton and detritus account for more than 40% of the total scattering effects [44]. Since the scattering light caused by phytoplankton and detritus propagates mainly in the forward direction, Mie scattering model can be used to approximate these two types of scattering [5]. In practice, the exact scattering coefficients highly depends on the density of phytoplankton and detritus [45]. In Figure 2.3(b) and Figure 2.3(c), we present the scattering spectra due to phytoplankton and detritus with different densities. A summary of the above discussion on seawater absorption and scattering characteristics is presented in Table 2.1.

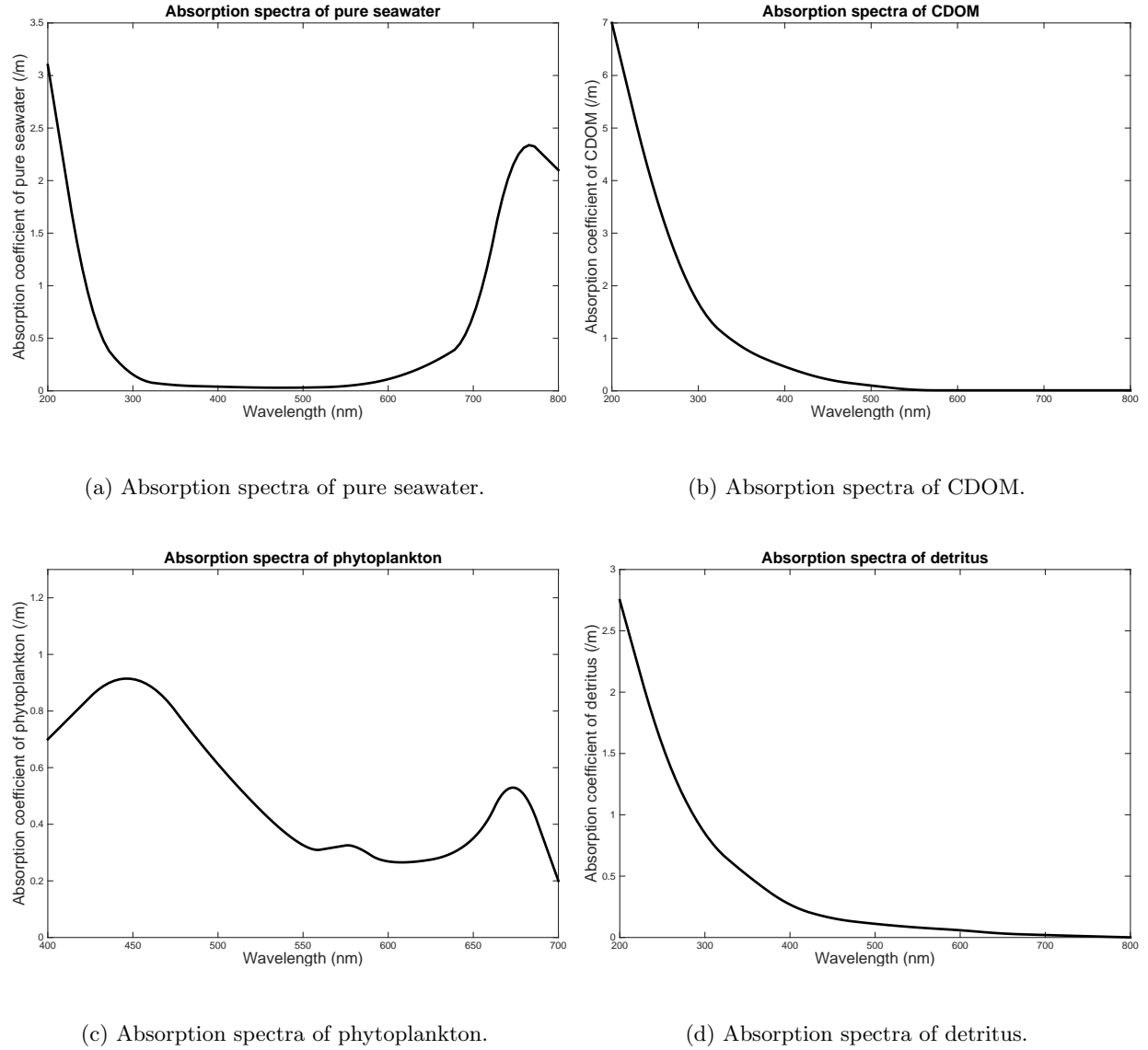
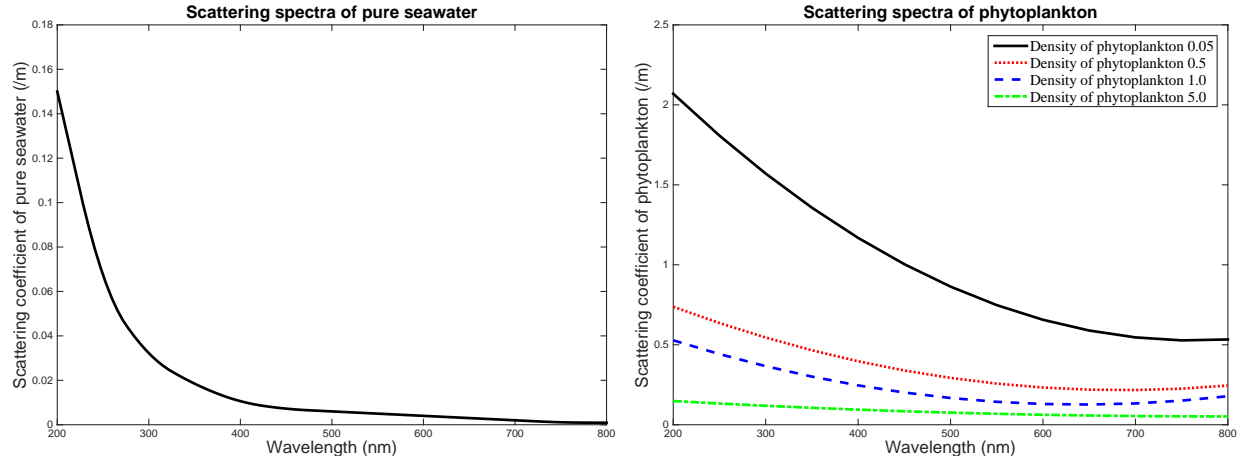
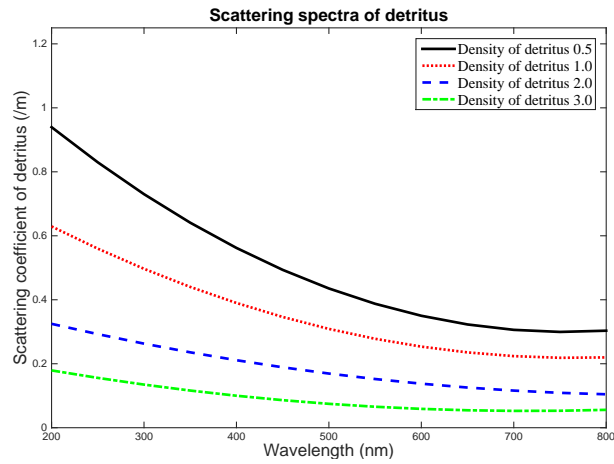


Figure 2.2: Optical absorption spectra for different ocean components. The data in Figure 2.2 is from [6–8].



(a) Scattering spectra of pure seawater.

(b) Scattering spectra of phytoplankton.



(c) Scattering spectra of detritus.

Figure 2.3: Optical scattering spectra for different ocean components. The data in Figure 2.3 is from [6–8].

Table 2.1: Summary of absorption and scattering characteristics of seawater [2]

Compositions	Absorption coefficient	Scattering coefficient
Water	Invariant at constant temperature and pressure. Strongly depends on λ	Rayleigh scattering. Small variance compared with absorption. Strongly depends on λ
Sea salts	Negligible in visible spectrum. Increase towards short λ	Rayleigh scattering. Doesn't depend on λ
CDOM	Variable with the density of CDOM. Increase towards short λ	Negligible
Plankton and detritus	Variable with the density of plankton and detritus. Increase towards short λ	Mie scattering. Variable with the density of plankton and detritus. Increase towards short λ

Based on the attenuation coefficient that has been introduced, Beer-Lambert law provides the simplest and most widely used scenario to describe the light attenuation effects in underwater environment [46] as

$$I = I_0 e^{-c(\lambda)z} \quad (2.7)$$

where I_0 is the power of transmitted light, z denotes the light transmission distance, I represents the power of light after transmitting z distance, and $c(\lambda)$ stands for the attenuation coefficient. The exact value of attenuation coefficient $c(\lambda)$ will change with different water types and water depth. The typical values of $a(\lambda)$, $b(\lambda)$, and $c(\lambda)$ associated with four major water types are given in Table 2.2 [5, 11, 37, 47]. In pure seawater, absorption is the main limiting factor, the low scattering coefficient makes the beam free from divergence. In clear ocean waters, there is a higher concentration of dissolved particles that affects scattering. In coastal ocean water, high concentrations of plankton, detritus and minerals are the dominant sources of absorption and scattering. Turbid harbor water has the highest concentration of dissolved and in-suspension matters, which will severely attenuate

the light propagation [37]. More details of water types and variations of attenuation coefficient with other parameters such as depth, pressure, and salinity can be found in [5, 30, 44, 48, 49].

Table 2.2: Typical values of $a(\lambda)$, $b(\lambda)$, and $c(\lambda)$ for different water types

Water types	$a(\lambda)$ (m^{-1})	$b(\lambda)$ (m^{-1})	$c(\lambda)$ (m^{-1})
Pure sea water	0.053	0.003	0.056
Clear ocean water	0.114	0.037	0.151
Costal ocean water	0.179	0.219	0.298
Turbid harbor water	0.295	1.875	2.17

From (2.4) and (2.7), we know that the Beer lambert's law contains two implicit assumptions. First, the transmitter and receiver are perfectly aligned. Second, all the scattered photons are lost even though in reality some of the scattered photons can still arrive at the receiver after multiple scattering events. This assumption severely underestimates the received optical power, especially in the scattering dominant situation. In order to describe the scattering effects more accurately, another important IOP volume scattering function (VSF) is introduced. It is defined as [36]

$$\beta(\theta, \lambda) = \lim_{\Delta D \rightarrow 0} \lim_{\Delta \Omega \rightarrow 0} \frac{P_S(\theta, \lambda)}{\Delta D \Delta \Omega} \quad (2.8)$$

where $P_S(\theta, \lambda)$ is the fraction of incident power scattered out of the beam through an angle θ into a solid angle $\Delta \Omega$ centered on θ (Figure 2.1). VSF is the scattered intensity per unit incident irradiance per unit volume of water. In the view of physics, the VSF can also be interpreted as the differential scattering cross section per unit volume [36].

Integrating $\beta(\theta, \lambda)$ over all directions (solid angles) gives the scattering coefficient [36]

$$b(\lambda) = \int \beta(\lambda, \theta) d\Omega = 2\pi \int_0^\pi \beta(\lambda, \theta) \sin(\theta) d\theta. \quad (2.9)$$

Normalizing (2.8) with the scattering coefficient, we obtain the scattering phase function (SPF), which is defined as [36]

$$\tilde{\beta}(\theta, \lambda) = \frac{\beta(\lambda, \theta)}{b(\lambda)}. \quad (2.10)$$

The scattering phase function is also an important IOP. Considering the difficulty of measuring scattering phase function (SPF), the Henyey-Greenstein (HG) function is commonly introduced to

present the SPF as [50–54]

$$\tilde{\beta}(\theta, \lambda) = P_{HG}(\theta, g) = \frac{1 - g^2}{4\pi(1 + g^2 - 2g \cos \theta)^{\frac{3}{2}}} \quad (2.11)$$

where g is the average cosine of β in all scattering directions.

To this end, we have introduced the concept of absorption and scattering coefficients, Beer Lambert’s law, as well as VSF. These concepts provide a theoretical basis for more complex UWOC channel models [37]. In a UWOC link, the optical signal launched from the transmitter will experience various losses before reaching the receiver. They include system loss introduced by transceivers, link loss results from water attenuation, geometric misalignment, and water turbulence. Since the loss introduced by the transceiver is mainly characterized by device parameters and design specifications, it is challenging to characterize the loss in a comprehensive and uniform approach. Thus, in Sections 2.2, 2.3 and 2.4, we will focus on the modeling techniques of the aforementioned losses in UWOC links.

2.2 Modeling of Aquatic Optical Attenuation in UWOC

As we have presented in Section 2.1, without considering the link configuration, transceiver architecture and alignment condition, the two major IOPs that will attenuate light propagation in UWOC systems are absorption and scattering. Thus, the modeling of UWOC aquatic optical link attenuation can be regarded as a task that accurately describes the absorption and scattering effects with specific link configurations. In the remaining of this section, we will introduce the models of aquatic optical attenuation in two categories: LOS configuration and NLOS configuration.

2.2.1 Aquatic Optical Attenuation in LOS Configuration

For simplicity, several researchers utilized the Beer Lambert’s law to model LOS UWOC. In [55] and [56], the authors evaluated the performance of a UWOC system based on Beer Lambert’s law in different water types and different communication ranges. The impacts of environmental variability, such as variations of refractive index with depth, were taken into account.

Another general theoretical model of aquatic optical attenuation in UWOC is radiative transfer equation (RTE). As we have presented in Section 2.1, the VSF is an important IOP that describes the scattering characterizations of photons. However, the VSF is difficult to be measured in practice [57]. Furthermore, the VSF can only determine the scattering properties of a single photon at one

single refractive index condition. It's not suitable to model the scattering properties of large number of photons [35]. Considering these two facts, most UWOC researchers employ RTE in their UWOC channel modeling research. Without considering the temporal dispersion of light, the typical two-dimensional RTE can be expressed as [58–60]

$$\vec{n} \cdot \nabla L(\lambda, \vec{r}, \vec{n}) = -cL(\lambda, \vec{r}, \vec{n}) + \int_{2\pi} \beta(\lambda, \vec{n}, \vec{n}') L(\lambda, \vec{r}, \vec{n}') d\vec{n}' + E(\lambda, \vec{r}, \vec{n}) \quad (2.12)$$

where \vec{n} is the direction vector, ∇ is the divergence operator, $L(\lambda, \vec{r}, \vec{n})$ denotes the optical radiance at position \vec{r} towards direction \vec{n} , $\beta(\lambda, \vec{n}, \vec{n}')$ is the VSF, and $E(\lambda, \vec{r}, \vec{n})$ represents the source radiance. RTE is capable of describing the energy conservation of a light wave that is passing through a steady medium [59, 60]. The derivations of RTE are complex and lengthy, and they can be found in [36] and [61]. The RTE can be solved both analytically and numerically. Since the RTE is an integro-differential equation involving several independent variables [58, 60], it is difficult to find an exact analytical solution. Thus only few analytical RTE models have been proposed in recent years. In [62], Jaruwatanadilok devised an analytical solution of RTE employing the modified Stokes vector. This model takes both multiple scattering and light polarization effects into account. Based on this model, numerical results show that the ISI and BER are as functions of data rate and link distance. This finding can be further used to predict several performance parameters of UWOC systems such as the maximum communication distance with certain data rate and BER. In [11] and [63], Cochenour *et al.* proposed a beam-spread function for laser-based UWOC by solving the RTE analytically. The small angle approximation was performed to simplify the derivation. This analytical model reveals the relationship between received optical power versus link range for various transmitter/receiver pointing accuracies. It was also validated through watertank experiments.

Besides utilizing analytical solutions, numerical methods are preferred to solve the RTE. In fact, for many practical UWOC applications, finding an exact analytical solution of RTE is even more challenging [58]. Moreover, since a series of assumptions and approximations have been made to simplify the RTE, the analytical solutions will also suffer from numerous limitations [64]. In view of this, most of the researchers focused on developing powerful numerical RTE solvers [46, 60]. The most popular numerical approach to solve RTE is Monte Carlo simulation. It is a probabilistic method to mimic the loss of underwater light propagation by sending and tracking large number of photons [65, 66]. The Monte Carlo method benefits from its easy programming, accurate solution and high flexibility, but it also suffers from random statistical errors and low simulation efficiency [36]. In [67], Leathers *et al.* from the U.S. Naval Research Laboratory (NRL) reported a practical

guide to generate Monte Carlo computer simulations for typical ocean optics applications. This method has been referred by many other UWOC researchers and has been proved to be robust.

In recent years, lots of researchers have employed Monte Carlo approach to solve the RTE or study the characterization of UWOC channels. In [68], Li *et al.* built a Monte Carlo simulator to model the impulse response of UWOC channel. Within this simulator, several receiver parameters such as aperture size and field of view (FOV) were taken into account. The authors utilized this Monte Carlo simulator in order to evaluate the channel capacity of a UWOC system with different link distances, water conditions, and transceiver parameters [69]. Simulation results indicate that the bandwidth of UWOC for clean water, coastal water and harbor water are on the order of hundreds of MHz, tens of MHz and MHz respectively [69]. Chadi *et al.* from Institut Fresnel utilized a Monte Carlo approach to solve the RTE and provided a channel model that can be used to appropriately predict different design parameters of UWOC systems [37]. As a continuance of [37], the authors in [50] proposed a channel impulse response of UWOC system by solving the RTE through Monte Carlo simulation. The authors quantified the channel time dispersion for different water types, link distances, and transmitter/receiver characteristics. A two-dimensional HG phase function was employed to model the VSF as

$$P_{TTHG}(\theta) = \alpha P_{HG}(\theta, g_{FWD}) + (1 - \alpha) P_{HG}(\theta, -g_{BKWD}) \quad (2.13)$$

where $P_{HG}(\cdot, \cdot)$ is the HG function defined in (2.11); α is the weight of the forward-directed HG function; and g_{FWD} and g_{BKWD} are the asymmetry factors for the forward- and backward-directed HG phase functions, respectively [50]. Based on this numerical channel model, the authors concluded that the channel time dispersion can be neglected when operating at a moderate distance (20m) in a clean water environment. However in highly turbid water, the channel time dispersion can impact the data transmission when operating over a large distance (100m). Based on this conclusion, the system will experience less ISI in the received signal when the transmission distance is short and the water is clear. As a result, complex signal modulation and demodulation can be avoided. In order to validify the Monte Carlo approach for UWOC channel modeling, Frank *et al.* made a comparison between the results of Monte Carlo simulation and laboratory experiments [47]. The results of the Monte Carlo simulation and the water-tank experiment exhibited reasonable agreement. Up to one Gbps data rate was achieved in a two-meter long water pipe. In [70], the authors employed Monte Carlo approach to solve the RTE and calculate the impulse response for a UWOC system over different operation environments. Another similar comparison between Monte

Carlo simulation and experimental measurements can also be found in [51]. The authors devised a numerical Monte Carlo simulation tool that is capable of computing received power of a UWOC system by considering the receiver aperture size, FOV, and pointing-tracking losses. This simulator is based on modeling a complex probability density function (PDF) (such as the lightfield distribution underwater) by its known individual components (such as the scattering distance of photons in water) [51]. By randomly sampling these known processes, the unknown PDF can be approximated using these discrete samples [51]. The accuracy of this simulator was validated through comparing the simulation results with the experimental data from [11, 71]. The author in [72] also made the Matlab source code of this simulation tool available to the public.

Besides the probabilistic Monte Carlo approach, there are also two deterministic methods that can be used to solve the RTE numerically: the discrete ordinates method and the invariant imbedding method [5, 46]. But only few researchers employed these two approaches as alternatives of Monte Carlo simulation. In [59] and [60], Li *et al.* developed an efficient RTE solver based on the deterministic numerical approach. This solver employs the matrix free Gauss-Seidel iterative method in order to calculate the received power of UWOC systems. It can also process highly forward peaked VSF that can not be handled well by the discrete ordinates approach. According to the simulation results, this method can achieve the same accuracy as the Monte Carlo approach but with a much shorter simulation time. The referred Matlab source code of this method can be found in the appendix of [59].

The majorities of aquatic optical attenuation models for UWOC are based on solving the RTE. However, instead of solving RTE, several stochastic models have also been proposed from the probabilistic nature of photon trajectory. In [73], Zhang *et al.* from Tsinghua University demonstrated a stochastic channel model to represent the spatial-temporal probability distribution of propagated photons for non-scattering and single scattering⁴ components of UWOC links. The authors adopted the HG function as the probability density function of light scattering angle to simplify the analysis. The proposed stochastic model also exhibited reasonable agreement with the numerical results of Monte Carlo simulation. Based on [73], the same research group further proposed a more general stochastic UWOC channel model in [74] by taking into account of all three components of propagated photons, which include non-scattering, single scattering and multiple scattering⁵ components.

⁴Single scattering components refer to photons that experience only one scattering event during the propagation from source to destination.

⁵Multiple scattering components refer to photons that experience more than one scattering event during the propagation from source to destination.

This comprehensive channel model fits well with the Monte Carlo simulations in turbid water environment, such as in coastal or in harbor waters. Following the similar stochastic approach of [73] and [74], the Tsinghua researchers also presented a closed-form expression for the angle of arrival (AOA) distribution in [75]. This AOA model characterizes how the received intensity of ballistic and single scattering components is distributed over AOA with respect to unit transmission power [75]. Numerical results have validated the proposed AOA distribution by Monte Carlo approach in clear and turbid coastal and harbor water with relatively short link range.

Semi-analytical modeling approach has also been employed by several UWOC researchers. In [76] and [77], based on the results of a Monte Carlo simulation, Tang *et al.* adopted a closed form double-Gamma function to represent the channel impulse response of the UWOC [76] as

$$h(t) = C_1 \Delta t e^{-C_2 \Delta t} + C_3 \Delta t e^{-C_4 \Delta t}, (t \geq t_0) \quad (2.14)$$

where $\Delta t = t - t_0$. t is the time scale and $t_0 = L/v$ is the propagation time which is the ratio of link range L over light speed v in water [76]. The parameter set (C_1, C_2, C_3, C_4) in (2.14) can be computed from Monte Carlo simulation results as [76]

$$(C_1, C_2, C_3, C_4) = \arg \min \left(\int [h(t) - h_{mc}(t)]^2 dt \right) \quad (2.15)$$

where $h(t)$ is the double Gamma functions model in (2.14) and $h_{mc}(t)$ is the Monte Carlo simulation results of impulse response; $\arg \min(\cdot)$ is the operator to return the argument of the minimum. Eq. (2.15) can be solved through a numerical curve fitting approach [76]. This semi-analytical impulse response is capable of describing the temporal dispersion of light in turbid underwater environments. It can be used to carry out a performance evaluation for calculating the BER and 3-dB channel bandwidth of a UWOC system. As an extension of [76] and [77], the authors applied a similar curve fitting approach to derive the the impulse response for LOS UWOC links with multiple-input multiple-output (MIMO) configuration [78]. Weighted double Gamma functions have been derived as the impulse response of a 2-by-2 LOS MIMO UWOC system in turbid water environment.

During the past ten years, a lot of research has focused on UWOC aquatic optical attenuation modeling. However, to this date, only a few models are capable of providing an end-to-end simulator for the UWOC designers [64]. There's still several "barriers" between the UWOC channel modelers and hardware engineers [64]. In [79], Doniec *et al.* presented an end-to-end model that can simulate the signal strength and communication distance in any propagation directions. This generic model incorporates all the components of a UWOC system that includes information of light source,

detectors, amplifiers, and analog-to-digital converters [79]. The authors also verified this model through an autonomous underwater optical robotic system. Since this model takes into account all the relevant components of a UWOC system as well as the attenuation properties of water, it provides a direct and complete reference for UWOC designers to estimate the overall system performance.

2.2.2 Aquatic Optical Attenuation in NLOS Configuration

As shown in Figure 1.3(d), in NLOS implementations, transceivers can utilize reflection of the sea surface to overcome link obstacles. Compared with channel modeling of LOS UWOC, investigations of NLOS UWOC channel modeling have received less attention. Light propagation in NLOS configuration experiences the same attenuation effects as in LOS configuration. The major difference between LOS and NLOS channels is the reflection effects introduced by wavy sea surface. Thus accurately describing the reflection effect of sea surface is considered as the most critical part of NLOS channel modeling. Several models that describe the slopes of random sea surface can be found in [10, 80, 81]. Similar to channel modeling work of LOS configuration, channel models of NLOS link can also be derived both analytically and numerically. To the best of our knowledge, most channel models of NLOS configuration were derived through numerical approaches such as through Monte Carlo simulations. As an example of an analytical approach, Shlomi *et al.* in [23] and [24] proposed a novel concept of NLOS UWOC network. Each node inside this network can communicate with each other through reflection at the ocean-air interface. Communication from one single node to multiple nodes can also be achieved. The authors derived a mathematical model for the NLOS channel by considering the link attenuation, sea surface slopes and receiver FOV. Numerical simulation was also performed to test the validity of this NLOS UWOC channel model. Simulation results show that an increase in node separation distance dramatically increases the BER of the NLOS UWOC system. By applying the numerical Monte Carlo method, the authors of [25] proposed a path loss model for NLOS UWOC links. The effects of both random sea surface slopes and scattering properties of seawater have been taken into account. Numerical results suggest that the random surface slopes induced by wind or other turbulent sources may strongly corrupt the received signal. However, this effect can be alleviated when the received signal contains multiple dominant scattering light components. In [82] and [83], Jagadeesh *et al.* proposed an impulse response for NLOS UWOC based on Monte Carlo simulation. A two-dimensional HG angle scattering function was employed in this simulation process in order to model the multiple

scattering effects of light. Based on this impulse response, the authors also evaluated the system performance with different water types and receiver FOV.

2.3 Modeling Geometric Misalignment of UWOC

As introduced in Section 1.2, the undiffused point-to-point UWOC links suffer from temporal misalignment. This undesired effect will degrade the system performance and induce temporal communication interruptions. In fact, link misalignment is unavoidable in any UWOC systems, and there are three major reasons that will tighten the system alignment requirements.

- a) Limitations of transceivers: In order to achieve a higher data rate and longer communication range, many UWOC applications utilize the laser diode and photo diodes as transmitters and receivers respectively. However, due to the narrow divergence angle of laser diodes and limited FOV of photo diodes, these UWOC systems require precise alignment.
- b) Relative motions caused by underwater vehicles, ocean current, and other turbulent sources: UWOC links suffer from severe misalignment when communicating with an AUV or ROV. Since the AUV or ROV keeps moving, the transceivers should always keep tracking with each other. Thus, link misalignment is more likely to occur. Ocean currents and wind can introduce random movements of transceivers in underwater environment, possibly causing link interruptions.
- c) Variations of refractive index: The refractive index will change with water depth, temperature, salinity, and other environmental conditions. This phenomenon usually occurs in surface-to-bottom UWOC links and will cause the non-straight light propagation, thus aggravate link misalignment of UWOC [30].

Similar to the modeling work of UWOC aquatic optical attenuation, both analytical and numerical methods can be implemented in the modeling of UWOC link misalignment. For the analytical cases, without focusing on the pointing error caused by slight jitter of the transceivers, the authors in [84] employed the beam spread function to model the link misalignment when the receiver deviates in a larger region [11, 84]

$$BSF(L, r) = E(L, r) \exp(-cL) + \int_0^\infty E(L, v) \exp(-cL) \times \left\{ \exp \left[\int_0^L bs(v(L-z)) dz \right] - 1 \right\} J_0(vr) v dv \quad (2.16)$$

where $BSF(L, r)$ is the irradiance distribution of the receiver plane; $E(L, r)$ and $E(L, v)$ are the irradiance distributions of the laser source in spatial coordinate system and spatial frequency domain, respectively [11]; L presents the distance between the source and the receiver plane; r is the distance between the receiver aperture center and the beam center on the receiver plane which is assumed to be perpendicular to the beam axis; b and c are the attenuation and scattering coefficients respectively; $s(v)$ is the scattering phase function. Through this model, the authors evaluated the BER performance of UWOC under misalignment condition. Numerical results indicated that, regardless of water type, an appropriate amount of misalignment will not cause severe performance degradation with sufficiently large transmission power. A similar conclusion was also drawn from the experiment of [85]. As an extension of [84], Dong *et al.* in [10] have presented a model of random sea surface slopes that concerns the link pointing errors caused by slight jitter of the transceivers for a vertical buoy-based UWOC system. The PDF of random sea surface slopes is expressed as [10]

$$P(s_x, s_y) = \frac{1}{2\pi\sigma_u\sigma_c} \exp \left[- \left(\frac{s_x^2}{2\sigma_u^2} + \frac{s_y^2}{2\sigma_c^2} \right) \right] \quad (2.17)$$

where $s_x = \partial z / \partial x$ and $s_y = \partial z / \partial y$ are defined as wave slopes of up/downwind and crosswind directions in the Cartesian coordinate (x, y, z) respectively; σ_u^2 and σ_c^2 denote the mean square slope in the up/downwind and crosswind directions, respectively. The authors employ this model and beam-spread function to evaluate the BER performance of the system. Numerical results suggest that the BER deteriorates as the pointing errors increase. This performance degradation can be released through an increment in the seawater turbidity. Zhang *et al.* have also employed a similar PDF of random sea-surface slope as [10] but in the form of angle to model the pointing errors of buoy-based downlink UWOC systems [86]. The authors utilized this model and evaluated the channel capacity of downlink buoy-based UWOC multiple-input multiple-output systems. Numerical results suggest that more turbid water, larger link range and larger inter-spacing may reduce the channel capacity, and meanwhile more turbid water and larger link range can weaken the effects of random slopes on the channel capacity [86].

Numerical methods have also been employed to model UWOC link misalignment. By using a Monte Carlo approach, the authors of [87] studied the impact of link misalignment on the received power of a point-to-point LOS UWOC system. This numerical model was validated through water-tank experiments. Since misalignment effects in LOS UWOC can also be caused by variations of refractive index. In [30] and [49], Laura *et al.* proposed a profile of the refractive index with the variation of depth. This profile was then used in a numerical ray-tracing simulation in order to

evaluate the tolerance of UWOC link offset. From the numerical results, a 0.23m link offset was allowed for 500nm laser with 0.57 degree FOV and 200m link distance. This work provides an effective reference for modeling link misalignment induced by refractive index variations [88].

2.4 Modeling Link Turbulence of UWOC

Turbulence in UWOC is defined as the event that makes water experience rapid changes in the refractive index [22]. This phenomena is commonly caused by ocean currents which will induce sudden variations in the water temperature and pressure. Most studies on UWOC channel modeling have focused on providing an accurate description of absorption and scattering effects, but the impact of underwater optical turbulence is commonly ignored. In fact, underwater optical turbulence can also cause considerable degradation to the performance of a UWOC system. Thus, more attention should be paid to this subject. The modeling of underwater optical turbulence is mainly based on research results of atmospheric optical turbulence channel models in free-space optical communications. Considering the similarity of underwater optical turbulence and atmospheric optical turbulence, several researchers directly applied or modified the classical atmospheric optical turbulence models as the underwater optical turbulence models. In [89], Hanson *et al.* adopted the Kolmogorov spectrum model to present the underwater optical turbulence. Motivated by [89], the authors of [90] characterized a UWOC channel model that includes both scattering/absorption and underwater optical turbulence. The proposed underwater optical turbulence model was adopted from the classical lognormal turbulence model used in FSO communication [90]

$$f_I(I) = \frac{1}{\sqrt{2\pi}\sigma_t I} \exp\left(-\frac{(\ln I - \mu)^2}{2\sigma_t^2}\right), \quad I > 0 \quad (2.18)$$

where I is the received optical irradiance, μ is the mean logarithmic light intensity, and σ_t^2 is the scintillation index. Based on this channel model, the authors developed a single-input-multiple-output (SIMO) UWOC system. Monte Carlo numerical simulation was performed to evaluate the system's BER performance. Numerical results show that the SIMO scheme can effectively reduce channel fading and extend communication range. Instead of using classic turbulence models of FSO communication, the authors of [91] employed oceanic turbulence model from [92] and [93] to investigate the temporal statistics of irradiance in the moving ocean with weak turbulence. They derived a closed-form expression that described the relationship of temporal correlation, propagation distance, and average velocity for the moving medium. Based on this expression, the authors also evaluated the temporal correlation of irradiance in specific turbulent ocean environments. Numerical

results show that the velocity of ocean flow is the dominant factor that causes turbulence and affects temporal statistics of irradiance in a UWOC system [91].

2.5 Summary

In this chapter, we presented several background knowledge on light propagation properties in the underwater environment. The concept of absorption, scattering, and VSF were introduced. Then, we demonstrated the UWOC channel modeling techniques in three aspects: link attenuation modeling, geometric misalignment modeling, and turbulence modeling. For link attenuation modeling, we presented the RTE and two viable methods. For geometric misalignment modeling and turbulence modeling, we explained the corresponding modeling mechanisms. At the end of this chapter, we summarized the literature related to channel modeling of UWOC in Table 2.3.

Table 2.3: Summary of literatures on UWOC channel modeling

UWOC channel models	Related references	Comments
Beer Lambert's law	[55, 56, 94]	Simplest UWOC channel model without considering temporal dispersion.
Chlorophyll-based Monte-Carlo model	[30], [42], [53, 95, 96]	Chlorophyll concentration severely affect underwater light attenuation.
Analytical RTE model	[11, 36, 61–63, 68]	Difficult to be solved.
Numerical RTE model	[47], [37], [46], [58], [59], [36], [65–67], [69], [50], [70]	Monte Carlo simulations are widely used.
Analytical Stochastic model	[73]	Derived from the nature of photon trajectory in the sense of probability.
Numerical Stochastic model	[51, 72, 76–78]	Open source simulator in [72]. [77] implemented MIMO.
End-to-end system model	[79]	Incorporates all the components of a UWOC system.
NLOS model	[10, 24, 25, 80–83, 97]	[10], [80], and [81] illustrated probability model of sea surface slopes.
Misalignment model	[10, 49, 84, 85, 87, 88]	Includes transceivers limitations, relative motions, and variations of refraction index.
Turbulence model	[89–93]	Turbulence models of FSO communications can be applied.

Chapter 3

UWOC Channel Modulation and Coding Techniques

In this chapter, we will first give a brief introduction of several digital modulation techniques that implemented in UWOC systems. The advantages and limitations of each modulation scheme will be presented. Then, we will discuss the channel coding techniques of UWOC. Finally, we will summarize this chapter and classify the related literatures on UWOC channel modulation and coding topics.

3.1 Modulation Schemes of UWOC

UWOC channel modulation techniques have attracted much attention in recent years due to its capability to impact the system performance considerably. Since UWOC can be regarded as implementing FSO in underwater environment, the conventional intensity modulation (IM) techniques that used in FSO communication systems can also be applied to UWOC systems. On-off keying (OOK) modulation is the most popular and simplest IM scheme in FSO communication system. This modulation scheme can also be implemented in UWOC systems. The OOK modulation is a binary level modulation scheme. During an OOK transmission, an optical pulse which occupies part of or entire bit duration represents a single data bit “1”. On the other hand, the absence of an optical pulse represents a single data bit “0”. There are two pulse formats in OOK modulation scheme: return-to-zero (RZ) format and non-return-to-zero (NRZ) format. In the RZ format, a pulse with duration that only occupies a part of the bit duration is defined to present “1”; however, the pulse duration occupies the whole bit duration in the NRZ scheme. The RZ-OOK has been proved having higher energy efficiency than the NRZ-OOK, but at the expense of consuming more channel bandwidth. Due to the severe absorption and scattering effects in underwater environment, the transmitted OOK signal suffers from various channel fading. In order to alleviate these impacts and achieve an optimal OOK signal detection, dynamic threshold (DT) techniques can be applied

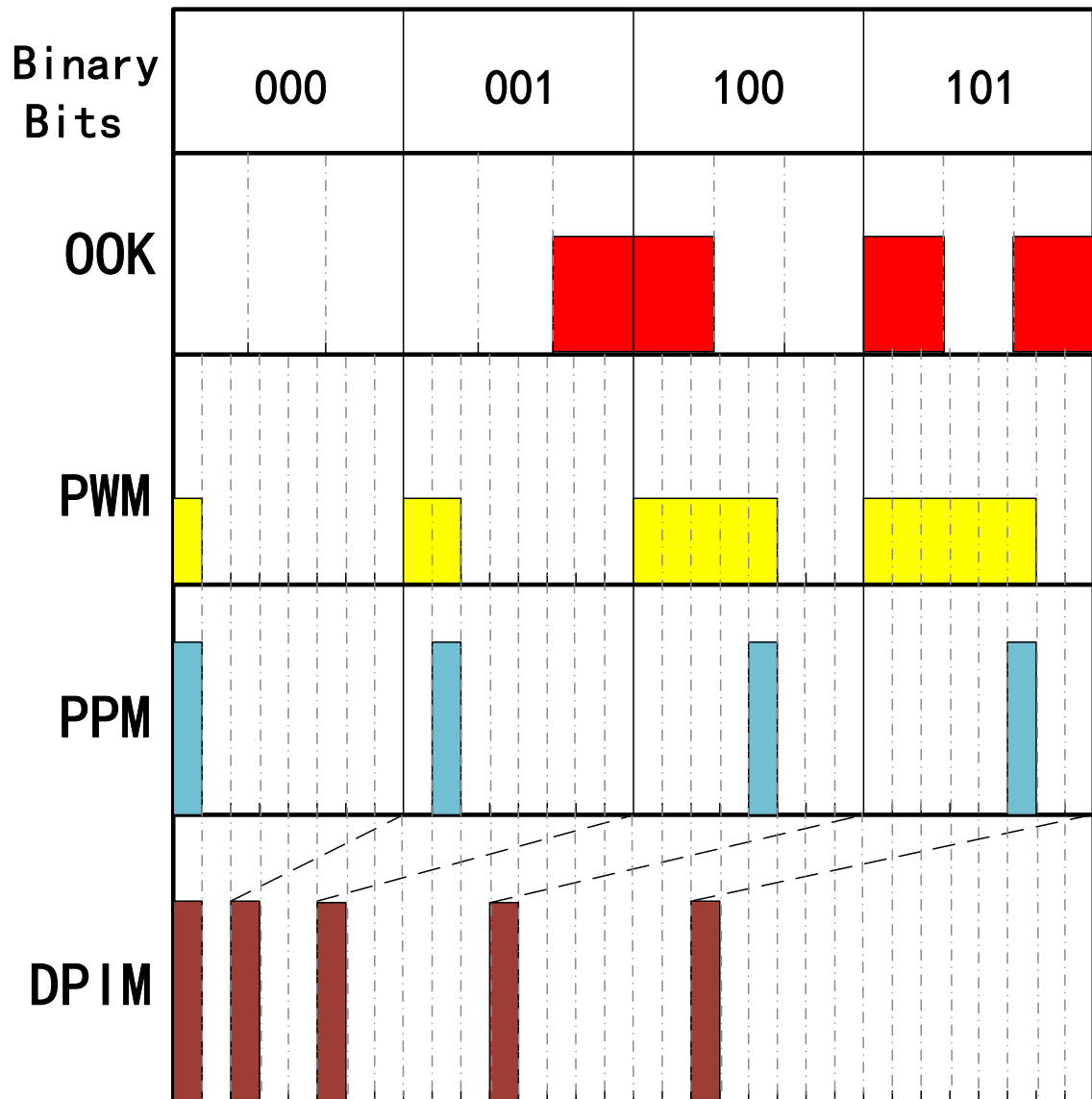


Figure 3.1: Illustration of OOK, PWM, PPM and DPIM. Figure 3.1 is adapted from [9].

in most UWOC OOK receivers. The DT is determined based on the estimation of channel fading. Several channel estimation techniques of FSO communication systems such as pilot symbol method, symbol-by-symbol maximum likelihood (ML) method, and ML sequence method [98] can also be employed by the UWOC OOK systems. The two major drawbacks of UWOC OOK scheme are low energy efficiency and spectral efficiency. But considering its simplicity, OOK modulation is still the most popular IM scheme in UWOC. It has been implemented in a number of theoretical and experimental UWOC research works [62, 99, 100].

Pulse position modulation (PPM) scheme is another popular modulation technique used in UWOC systems. Compared with OOK modulation, PPM has much higher energy efficiency and doesn't require dynamic thresholding, but at the expense of lower bandwidth utilization rate and more complex transceivers. In PPM, every transmitted M bits will be modulated as one single pulse in one of 2^M time slots, and the pulse position represents the transmitted information (Figure 3.1). The main drawback of PPM modulation is the tight timing synchronization requirement. Any timing jitters or asynchronization will severely degrade the BER of system. In recent years, several researchers have studied the performance of PPM scheme over UWOC channel models. The authors of [101] have investigated the performance of 4-PPM scheme over numerical RTE channel model. They have found that the corresponding BER for PPM scheme is almost equal to that of OOK modulation and with much higher energy and spectrum efficiency. More complex PPM such as 8-PPM or 16-PPM can be used to improve higher bandwidth efficiency. In [102], Sui *et al.* proposed a modified PPM scheme for UWOC. This modified PPM can maintain the similar power efficiency and anti-noise performance as the conventional PPM. It also has improved the bandwidth utilization rate of the system. Besides theoretical studies, PPM was also applied in several experimental UWOC implementations. The related literatures can be found in [103–109].

Similar to PPM, pulse width modulation (PWM) also utilizes the relative positions of pulses to represent data symbols. In L -ary PWM, optical pulses will only appear in the first L consecutive time slots to represent one symbol, where L is equal to the decimal of symbol bits (Figure 3.1). Since the PWM extends the total pulse time during the transmission of one symbol, the peak transmission power of each pulse is reduced (Figure 3.1). The PWM scheme also benefits from better spectral efficiency and stronger resistance to ISI. However, these two advantages will be counterbalanced by higher average power requirements that increase with number of slots per symbol [98].

Digital pulse interval modulation (DPIM) is also widely implemented in UWOC. In this modulation, an “On” optical pulse slot is sent and followed by a number of “Off” slots. The number of

“Off” slots depends on the decimal value of the transmitted symbol, and an additional guard slot is commonly added in order to avoid sending consecutive “On” pulses (Figure 3.1) [9]. Compared with PPM and PWM which require slot and symbol level synchronization, digital pulse interval modulation is an asynchronous modulation scheme with variable symbol length [98]. Furthermore, with variable symbol length, DPIM also has higher spectral efficiency than PPM and PWM [98]. The most critical problem of DPIM is the error spread in demodulation. From Figure 3.1, we notice that if an “Off” slot is demodulated as “On”, then all the succeeding symbols will also be wrong. Applications of DPIM can be found in several UWOC applications of ROVs and AUVs such as [110–112].

Similar to the comparison of IM schemes that we have made, the authors of [9] also performed a comparison study on different IM techniques for UWOC. This comparison included OOK, PPM, PWM, DPIM and other derivative IM schemes such as multi-pulse PPM (MPPM) and differential PPM (DPPM). Simulation results show that with the same link distances, PPM is the most energy efficient modulation scheme. DPIM has better bandwidth efficiency over PPM and OOK but at the expense of more complex demodulation devices. Other similar comparison of IM for UWOC can also be found in [108] and [113].

Coherent modulation schemes have also been implemented in several UWOC systems. In contrast to the direct IM schemes, coherent modulations encode the information on the amplitude, polarization or phase of optical carriers. At the receiver side, the same synchronized optical carrier will mix with the received optical signals and accomplish demodulation. Compared with IM, coherent modulations benefit from higher receiver sensitivity, higher system spectral efficiency and better rejection on background noise, but at the expense of higher implementation complexity and higher cost [98]. Due to the high dispersion effect of seawater, coherent modulation at optical frequencies is difficult to be achieved in UWOC systems. In order to overcome this limitation, intensity modulation has to be imposed on the pre-modulated signals [114]. Typical coherent modulations used in UWOC systems include quadrature amplitude modulation (QAM), phase shift keying (PSK), and polarization shift keying (PolSK).

In [114], Cochenour *et al.* presented an experimental comparison study of binary PSK (BPSK), quadrature PSK (QPSK), 16-QAM and 32-QAM in a UWOC system. The authors evaluated the link performance for different coherent modulations with different levels of water turbidity. A summarization of constellation diagrams for each modulation techniques was demonstrated. Similarly, the authors of [115] compared the coherent PSK, frequency shift keying modulations with several

IM schemes such as OOK and PPM. Simulation results have demonstrated that PSK modulation performs the best over other modulation schemes in terms of data rate and BER. But it also suffers from poor power efficiency. A binary PolSK (BPolSK) modulation for UWOC has been introduced in [116]. In BPolSK, the signal is modulated by changing the polarization of the light. Since polarization states of light are less sensitive than the amplitude, phase or intensity of optical signals, BPolSK has higher tolerance to underwater turbulence and other channel interference such as ambient light. This property is ideal for UWOC in low SNR environment. PolSK can also be used to suppress backscatter of the transmitter in a duplex system and has better immunity to phase noise of lasers [98, 116]. Although PolSK is ideal for optical wireless communications, it still suffers from short transmission distance and low data rate. To overcome these limitations, Dong *et al.* presented a novel polarized pulse position modulation (P-PPM) [117, 118]. This modulation scheme combines conventional PPM and PolSK together by transmitting a series of PPM symbol in different polarization directions [118]. Numerical results show that P-PPM benefits from the virtues of both PPM and PolSK. It can increase the transmission bandwidth and distance of a UWOC system.

Another coherent modulation scheme implemented in UWOC is the subcarrier intensity modulation (SIM). The interest of SIM is the much higher spectral efficiency [9]. But SIM also requires complex modulation/demodulation devices and suffers from poor average power efficiency [119]. By using SIM, orthogonal frequency-division multiplexing (OFDM) can also be achieved in UWOC systems [119, 120].

3.2 Channel Coding of UWOC

As was discussed in the previous chapters, due to the severe absorption and scattering effects induced by sea water, the transmitted optical signal will experience considerable attenuation. This undesirable effect will directly degrade the BER performance of UWOC system. In order to mitigate the impact of aquatic optical attenuation and maintain a low BER in low SNR underwater environment, forward error correction (FEC) channel coding techniques can be implemented in UWOC systems.

FEC coding is an error-control technique that adds redundant bits into the transmitted sequence so that the receiver can correct a limited number of errors in the received message. A properly designed FEC code is capable of improving the power efficiency of a communication system, but at the expenses of decreased bandwidth efficiency. For a UWOC system, these benefits are presented as

lower transmitter power requirements or extended link range. Generally, FEC codes can be divided into two categories: block codes and convolutional codes [121]. Researchers have employed several classical block codes into the UWOC systems due to their simplicity and robustness. The first block code that implemented in UWOC system is the Reed-Solomon (RS) code [122]. In [122], Cox *et al.* demonstrated an experimental UWOC system that utilized (255, 129) RS FEC code. This system employed 405 nm laser diode and RZ OOK modulation to achieve a 500 kbps UWOC link in a 3.66 meters long water tank. The experimental results suggested that the coded system can reduce the required power to achieve a BER of 10^{-4} by approximately 8 dB compared with an uncoded OOK system. Based on [122], the same research group from North Carolina State University upgraded their system in [123]. In the upgraded system, a 5 Mbps UWOC link was established also using RS code in three and seven meters long water tanks. The experimental results show that the (255,129) RS and (255,223) RS codes are capable of improving the SNR of received signals about six and four dB respectively at a given BER of 10^{-6} . Another similar experimental UWOC system that utilized (2720,2550) RS and SIM can be found in [120]. In this system, the (2720, 2550) RS code performed an error correction that reduced the input BER of $1.5 \cdot 10^{-3}$ to 10^{-9} .

Besides the RS code, other classical block code and error-detecting code such as Bose-Chaudhuri-Hocquenghem (BCH) code and cyclic redundancy check (CRC) code have also been implemented in UWOC systems to improve the BER performance in low SNR underwater environment. In [124], the authors simulated the anti-noise performance of BCH and RS codes with simple OOK modulation. Numerical results indicated that the RS code outperformed the BCH code in error correction capability, but at the expense of lowering transmission data rate. In [106], a UWOC system based on hardware description language (HDL) was demonstrated. In this system, the authors referred the architecture of IEEE 802.15.4 and IEEE 802.11 protocols and implemented CRC code in the medium access control (MAC) layer of the system. The BER performance at the receiver was improved compared with uncoded systems. Instead of applying one layer of FEC code for byte-level error correction, packet-level error correction coding schemes were also developed to maintain the robustness of UWOC system. In [79] and [125], Doniec *et al.* embedded a two-layer error correction coding scheme into a UWOC video transmission system. In this two-layer channel coding scheme, the transmitted video frames were firstly encoded on Manchester codes and Luby Transform (LT) codes to mitigate packet-level losses, then CRC and RS codes will be employed sequentially for byte-level error correction at the physical layer. Experimental results show that this multi-layer coding scheme can greatly improve the robustness of the UWOC system in a turbid

water environment. But trade-offs may be taken between system performance and complexity.

Although several block codes are simple to be implemented, they are not capable of providing the optimal performance for UWOC, especially in the environment with strong interference. Thus, more complex and powerful channel coding schemes such as low-density parity-check (LDPC) code and Turbo code are employed. LDPC code is a highly efficient linear block code. It is constructed by employing sparse parity check matrices and can provide an error-correction performance close to the Shannon limit [98]. Turbo code is a parallel concatenated code. It combines two or more convolutional codes and an interleaver to produce a block code that can also achieve a BER close to the Shannon limit. Although lots of research works on implementing LDPC and Turbo codes in FSO communication system have been proposed, there is still little investigation on applying LDPC and Turbo codes in UWOC. Everett demonstrated the performance of RS, LDPC and Turbo codes in UWOC systems both theoretically and experimentally [126]. The author explained the mechanism of RS, LDPC and Turbo codes in details, and compared their performance for UWOC such as BER, power efficiency, and link distance extension. This work provides a relatively complete description of implementing channel coding techniques in UWOC.

3.3 Summary

In this chapter, we first introduced several IM schemes that implemented in UWOC systems such as OOK, PPM, PWM, DPIM and so on. Then, applications of coherent modulation techniques in UWOC systems were presented. Besides the modulation schemes applied in UWOC, we also introduced the applications of channel coding methods. These applications include the simple classical block codes such as RS code and BCH code, as well as more powerful LDPC and Turbo codes. At the end of this chapter, we will summarize all the related literatures of UWOC channel modulations and coding techniques in Table 3.1 and Table 3.2 respectively.

Table 3.1: Summary of literatures on UWOC modulation schemes

UWOC modulations	Literature	Comments
OOK	[62], [99], [100], [113]	Simple but with low efficiency.
PPM	[101–109]	High energy efficiency.
DPIM	[9], [110–112]	Higher bandwidth efficiency.
PSK	[114, 115, 119]	Combined with intensity modulation.
QAM	[114]	Combined with intensity modulation.
PolSK	[116–118]	Higher tolerance to underwater turbulence.
SIM	[119, 120]	Increase system capacity; low cost.

Table 3.2: Summary of literatures on UWOC channel coding

UWOC channel codes	Literature	Comments
RS	[79], [124], [125], [127]	Simple and robust block codes.
BCH	[124]	Simple and robust block codes.
CRC	[79], [106], [125]	Simple error-detecting codes.
LT	[79], [125]	Practical fountain code.
LDPC	[126]	Complex linear block code.
Turbo	[126]	Complex convolutional code.

Chapter 4

Experimental Setups and Prototypes of UWOC

In this chapter, we will study the experimental setups and prototypes of UWOC from different aspects. Firstly, we are going to introduce several typical LOS/NLOS experimental setups and prototypes of UWOC. Secondly, we will review the research of UWOC implementations in several specific topics, which include retroreflector, smart transceiver design, UWOC for underwater vehicles and the hybrid UWOC systems. Finally, we will summarize this chapter and propose the literature classification of experimental UWOC systems.

4.1 Typical LOS/NLOS UWOC systems

As we have mentioned in Chapter 1, although a few commercial UWOC products were proposed in the early 2000s, the large scale commercial applications of UWOC systems have not been realized so far. Most of the UWOC systems are experimental demonstrations and prototypes in laboratory environment. In the remaining of this section, we will provide a comprehensive summary of the recent progress on experimental UWOC research. The purpose of this summary is not to introduce all the UWOC experimental literatures in details, but to provide a general description of the most recent works on UWOC experiments that concern different applications and approaches.

According to the link configurations, experimental setups and prototypes of UWOC can be divided into two categories: LOS experimental setups and NLOS experimental setups. Due to the simplicity of implementation, most UWOC experimental systems utilize LOS configuration. In Figure 4.1, a typical laboratory LOS UWOC system based on intensity-modulation direct-detection is demonstrated. The configuration of LOS UWOC link is similar to the FSO communication setups [98]. On the transmitter side, the information bits are generated by a personal computer (PC), and then modulated onto optical carriers. In several UWOC experiments, the modulated optical signal will be further amplified by an optical amplifier and then transmitted through lens that are precisely

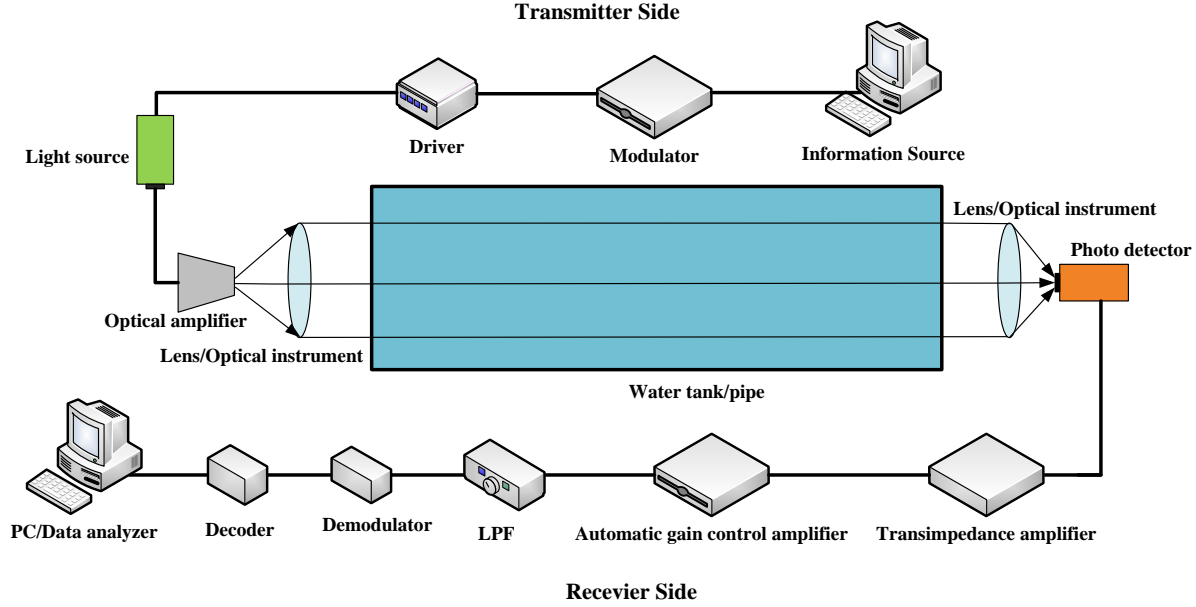


Figure 4.1: A typical laboratory LOS UWOC system based on intensity-modulation direct-detection (IM/DD) technique.

aligned to focus the light. Water tank or pipe is used to model the underwater transmission link. In order to mimic the different refractive condition and turbidity of underwater environment, Maalox is added in the water to act as a scattering agent for attenuating the light beam [94, 127]. On the receiver side, the optical signal will go through an optical filter and focusing lens. It will then be captured by the photodiode. Since photodiode can only transform the variations of light intensity into corresponding current changes, a trans-impedance amplifier is cascaded as the following stage to convert current into voltage. The transformed voltage signals will then go through a low pass filter to reduce the thermal and ambient noise levels [98]. Further signal processing programs that include demodulation and decoding will be performed at the last two stages of the receiver. The recovered original data will finally be collected and analyzed by a PC or BER tester for evaluating several important performance parameters such as BER.

There are two light sources that are commonly used in typical UWOC experimental systems: light-emitting diodes (LEDs) and laser diodes (LDs). As it was stated in Chapter 1, blue or green wavelength has been chosen for the light sources to minimize the aquatic optical attenuation. Compared with LED, LD has higher output power intensity, better collimated properties, narrower spectral spreading, and much faster switching speeds. But at the expense of higher cost, shorter

lifetime and dependence on temperature. Thus LDs are more appropriate to be implemented in applications of high-speed UWOC that has strict alignment requirement. In several LD-based UWOC applications, optical diffusers are implemented to reduce the system pointing requirements. Compared with the LD-based UWOC system without diffusers, this diffused LD-based UWOC system can benefit from both high speed and relatively low pointing requirements. On the other hand, since LEDs offer lower output power intensity, wider divergence angles, and lower bandwidths. They can be installed in several diffused UWOC applications with short-range, low-speed link requirement.

At the receiver, there are also two types of photodiodes that are widely used in UWOC experiments: P-i-N (PIN) diode and avalanche photodiode (APD). The major difference between these two devices is in the noise performance. For PIN photodiodes, the dominant noise is thermal noise, while for the APDs, the performance is mainly limited by shot noise [98]. Since APD can provide higher current gain, it can be implemented in longer UWOC links (tens of meters), but at the expense of more complex auxiliary circuits. Besides PIN diodes and APDs, photomultiplier tubes (PMT) have also been implemented in several UWOC experiments [70, 105, 106, 128–131]. Compared with photodiodes, PMT benefits from higher sensitivity, higher optical gain and lower noise levels. But it also suffers from high voltage supplies (on the order of hundred volts) and high unit cost. Moreover, PMT is susceptible to shocks and vibration. It can be easily damaged by the overexposure to light. The cost of PMTs are also much higher than photodiodes. Thus PMTs are commonly used in static experimental UWOC systems. Based on the typical LOS UWOC link configuration and the critical devices that we have introduced, lots of experimental UWOC links focusing on channel model verification and system performance analysis have been proposed in recent years.

Since LED benefits from its low cost and stable performance in various environments, several researchers preferred to employ it as the light sources in experimental UWOC systems [109, 120, 124, 132]. In [7], Chancey proposed a UWOC system based on high power Gallium Nitride LEDs. This experimental demo is capable of achieving 10 Mbps video transmission over a distance of 12 meters. Also in [8], Simpson from the North Carolina State University demonstrated a UWOC system with signal processing capabilities that utilized high-power LED as the light source. Experimental results show that 1 Mbps data rate is achievable over a distance of 3.66 meter long. Similarly, the author of [133] has also developed a UWOC system that utilized a high-power blue LED as transmitter and a blue enhanced photodiode as receiver. This system successfully accomplished a 3 Mbps data

transmission in a 13-meter long water tank. By using the mirrors folding architecture, the authors of [95] tested their LED based UWOC system over a distance of 91 meters, a maximum data rate of 5 Mbps was accomplished. Recently, researchers from the Massachusetts Institute of Technology (MIT) presented a bidirectional UWOC system named AquaOptical [110]. The transmitter of the system consisted of six five watts LEDs with 480 nm wavelength. The researchers tested this demo system in both pool and ocean environment. Experimental results showed in clear pool water, the AquaOptical can achieve a data rate of 1.2 Mbps at distances up to 30 meters; while in turbid water with only three meters visibility, the system achieved a data rate of 0.6 Mbps over nine meters. As an upgraded version of AquaOptical, AquaOptical II can establish a bidirectional underwater communication link between each transceivers [111]. Since AquaOptical II is designed using a software defined radio, it has more powerful signal processing capabilities than its previous generation and can also achieve a data rate of two Mbps over a distance of 50 meters. Several theoretical channel models have been validated through this testbed [79]. Furthermore, the MIT researchers also performed a real-time video delivery experiment by employing AquaOptical II [125]. Using the same design approach of software defined radio, Cox *et al.* from North Carolina State University have also built up a UWOC experiment based on LED [119]. Since software defined radio system is more configurable than conventional hardware implementations, it is convenient to test various modulation formats or digital filtering schemes on UWOC [119]. The authors examined the performance of BPSK and Gaussian minimum shift keying (GMSK) schemes and accomplished a data rate of one Mbps over a range of 3.66 meters. Most recently, a typical cellular UWOC network prototype based on LEDs was demonstrated in [99]. The authors implemented code division multiplexing access (CDMA) techniques in this prototype and tested the network performance in various water conditions. Besides the experiments that we have already mentioned, other similar recent experimental UWOC systems and prototypes that utilized LEDs as light sources can also be found in [100, 108, 134].

Instead of using LEDs, several experimental setups also utilized lasers as the light sources due to its high bandwidth and lower noise floor [63, 85]. Although laser and laser diodes were invented in the early 1960s, only few early laser-based UWOC experiments have been performed in the 1990s [103, 135]. In recent years, with the cost reduction and popularization of laser devices, there is a surge of laser-based UWOC experimental systems. Cox *et al.* constructed a laboratory testbed based on a 405 nm blue laser diode and PMT. This setup can provide up to one Mbps underwater data transmission in a distance of 12 meters [136]. Hiskett *et al.* proposed a laser-based UWOC

system by utilizing 450nm laser diode and APD [137]. One 40 Mbps wireless communication link was established over one meter water tank. In [128], the authors demonstrated a real-time underwater video transmission system by implementing 488 nm blue laser and PMT. Five Mbps high-speed video stream was successfully transmitted through 4.5 meters long underwater channel. Several researchers employed laser to study the spatial and temporal dispersion effects of UWOC links over different modulations, coding schemes and water conditions [138–141].

Compared with typical LOS UWOC experimental systems, only few UWOC experiments have focused on the diffused and NLOS link configurations. Pontbriand *et al.* from the Woods Hole Oceanographic Institution (WHOI) demonstrated a broadcasting diffused UWOC system [142]. This system can achieve a data rate up to 10 Mbps over a maximum vertical distance of 200 meters and horizontal radius up to 40 meters [142]. In [143], Cochenour *et al.* employed 532 nm laser and a diffuser to generate diffused light. A diffused UWOC link with up to 1 Gbps data rate in 7.72 meters long water tank was established. On the other hand, the experimental NLOS UWOC links are mainly focused on the applications of underwater ranging and imaging. In [144], Alley *et al.* proposed a NLOS imaging system that utilized 488 nm blue laser as the illuminator. Experimental results demonstrate that, compared with the conventional LOS imaging system, this NLOS configuration significantly improves the SNR of imaging. A similar experimental approach that employed modulated pulse laser in NLOS configuration for underwater detection, ranging, imaging, and communications was presented in [145].

4.2 Retroreflectors in UWOC

Retroreflector is an optical device that can reflect arbitrary incident light back to its source (Figure 4.2). Utilizing this beneficial characterization, a modulating retroreflector UWOC system was introduced. In the modulating retroreflector link (Figure 4.3), the active transceiver projects a light beam into the retroreflector. During the reflection process, the modulator will modulate the light beam and add information on it. This information will later be captured and demodulated by the active transceiver. The most significant advantage of modulating retroreflector UWOC system is that most of the power consumption, device weight, volume and pointing requirements are shifted to the active end of the link, thus the passive end will benefit from small dimensions, relatively low power and pointing requirements [146]. There are lots of sensor nodes and underwater vehicles in UWSNs. Each sensor node and underwater vehicle is required to have long enough cruising time due

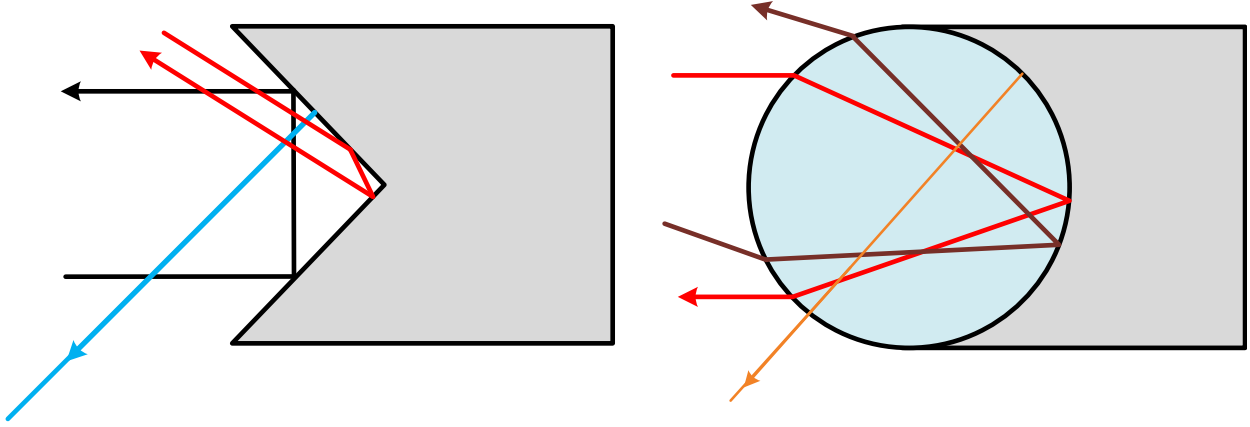


Figure 4.2: Demonstration of corner and spherical retroreflectors.

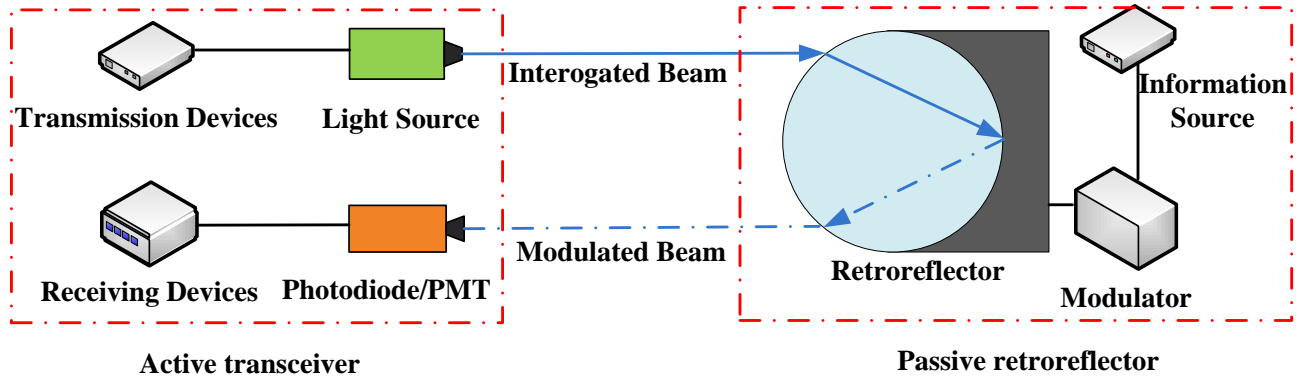


Figure 4.3: Modulating retroreflector link.

to the difficulty of recharging battery. In this sense, modulating retroreflector becomes an attractive choice. In addition to the challenges that involved in a direct UWOC link such as absorption and scattering, retroreflector-based UWOC systems have several additional limitations. Unlike the typical UWOC links, the retroreflector based UWOC links have to transmit through the underwater channel twice, so the link will experience higher attenuation and interference. Furthermore, the backscattered light generated from the interrogating beam can be significant in turbid water where it will eventually surpass the desired retro-reflected signals.

Although the concept of implementing retroreflector into FSO communication system has already been proposed for almost 20 years [147], only few research works on UWOC retroreflector system were demonstrated recently. The first institute that implemented retroreflector FSO

communication in marine environment is the U.S. Naval Research Laboratory (NRL). Since late 1990s, the NRL began to launch the research of retroreflector applications in FSO communication and successfully achieved shore-to-shore, boat-to-shore and sky-to-ground retroreflector FSO links [146, 148, 149]. Based on these achievements, NRL researchers then applied the retroreflector link into underwater environment. In [150] and [151], Mullen *et al.* employed a polarization discrimination technique to overcome the impact of backscattering on the interrogating light. An experimental test was also performed in laboratory water tank to evaluate the system performance. The authors compared the experimental results of polarized and non-polarized setups with different transceiver FOV and link ranges. Experimental results showed that, by utilizing polarization discrimination technique, the backscatter level can be greatly reduced. This fact will then increase the communication range of retro link. In [127], Cox *et al.* from North Carolina State University proposed a blue/green retro-reflecting modulator for UWOC based on micro-electromechanical system (MEMS). The authors deployed the retroreflector link in a 7.7 meters long water tank and evaluated the system performance with various water turbidities. Experimental results show that 1 Mbps and 500 kbps data rates can be achieved in 2.7 attenuation length⁶ and 5 attenuation length respectively.

4.3 Smart Transceivers of UWOC

As shown Figure 4.1, in a UWOC system, the information waveforms are generated by a source and then transferred by an optical transmitter through the water channel to a specific destination. At the other end of the link, the receiver will collect the optical signal and recover the original information. Although the transmission wavelength is carefully selected in blue/green transparent window to minimize the attenuation effect of sea water, several other factors such as misalignment will still severely degrade the link performance. As we have stated in Chapters 1 and 2, most UWOC systems utilize point-to-point configuration, and thus precise pointing and tracking requirements are necessary. However, link misalignment is an inevitable phenomena in underwater environment, any variations of refractive index or turbulence of ocean can cause link misalignment and interrupt communication. Especially in mobile UWOC applications such as AUVs and ROVs, the two ends of a link are all in nonstatic condition, which makes the alignment more difficult to be achieved. Conventionally, there are three common methods to relief the pointing requirements of a UWOC system: using diffused light beam, increasing receiver aperture size, or implementing a dedicated

⁶The attenuation length defined as the product of attenuation coefficient and link distance.

gimbal system. Diffused light beam can effectively increase the illuminated area of a light source, but the communication range also shrinks. Although large aperture can increase the receiver FOV and it has already been implemented in several UWOC systems such as [142], the extra introduced ambient light and limited transceiver size requirement will still restrict the application of this method. Dedicated gimbal system can be used in several applications that have less size limitation and energy requirements, but for compact UWOC systems that don't have much volume and energy budget, this approach is not practical.

Considering the limitations of each compensation method that we have introduced, a compact adaptive smart UWOC transceiver that can relax the misalignment requirement with minimized volume and energy cost. In [152], Simpson *et al.* proposed a novel UWOC front-end that introduced the concept of smart transmitter and receiver. The smart quasi-omnidirectional transmitter can estimate the water condition according to the backscattered light captured by the adjacent smart receiver. Based on specific water conditions, the transmitter can take several actions such as changing transmission light wavelength to improve link performance. The transmitter can also electronically switch the beam direction according to the angle of arrival of detected signal. On the receiver side, segmented lens array architecture was implemented to increase the total FOV. By using the information of angle of arrival estimation, the smart receiver can also adjust and steer the FOV towards the direction of desired signals to improve the SNR of the received signal. Moreover, the CDMA technique has also been implemented in both transmitter and receiver ends to reinforce the system performance in multi-user environment. The authors installed the prototyping smart transceivers in a 3.66-meter long laboratory water tank to evaluate the system performance. Experimental results demonstrate that the smart system can effectively increase the total FOV of the receiver. The preliminary algorithm for angle of arrival estimation and backscatter estimation was also verified to work properly. Other performance aspects such as diversity combining and multi-user CDMA approach were also tested and proved to be effective. This novel trial of smart transceivers provides an adaptive solution to handle the impact of dynamic nature of underwater environment to the UWOC systems. It can be applied to different underwater platforms such as AUVs, ROVs, and other sensor nodes embedded with UWOC system. Several theoretical research works focusing on smart or adaptive UWOC transceivers were also proposed. In [107], Tang *et al.* presented an adaptive gain control scheme for UWOC receivers based on APD. The authors derived a close-form expression that can describe the relationships of optimal gain of APD, link range and receiver offset distance. This result can be further applied to practical design of UWOC transceiver

for improving the link reliability.

4.4 UWOC for Underwater Vehicles

With the increasing demands of human underwater activities, underwater vehicles such as AUVs and ROVs have been widely applied to perform different tasks such as undersea resource exploration, wreck rescue missions and maintenance of oil production facilities. In the perspective of communication methods, underwater vehicles can be divided into three categories: tethered underwater vehicles, wireless underwater vehicles, and hybrid underwater vehicles. Tethered underwater vehicles are usually controlled robots that connected to the surface control platform through an optical fibre or electrical cable. The tethered system has long endurance time and can provide reliable high-speed data communication, but at the expense of higher manufacture cost and limited operation range. On the other hand, conventional wireless underwater vehicles are usually autonomous operated robots that utilize acoustic wave as the viable communication carrier [153]. Since this kind of vehicle is free from the limitations of connection cable, it has more flexibility and can operate in a vast area. The bottle neck of this approach are the low bandwidth, high latency, and complex energy-consuming acoustic transceivers. Hybrid underwater vehicles integrated both tethered and wireless systems together [154, 155]. It has the optimal flexibility and reliability, but it's not suitable for the large-scale implementations in UWSNs due to the high unit cost, bulky instrumentations, and large number of cables.

In order to satisfy the needs of UWSNs for compact, durable, and high-bandwidth underwater vehicles, several researchers have embedded UWOC into AUVs and ROVs to overcome the limitations of conventional underwater vehicles. A team from the Computer Science and Artificial Intelligence Laboratory (CSAIL) of MIT firstly proposed a prototyping AUV system called autonomous modular optical underwater robot (AMOUR) [156]. The AMOUR was designed to perform tasks that including underwater monitoring, exploration, and surveillance. Since AMOUR is based on a stack-up modular design approach, it also has the capabilities to deploy and recover sensor nodes in the sensor networks. The earliest version of AMOUR employs LEDs as the light source and can achieve one Kbps data rate over a distance of two meters. After the presentation of the first AMOUR prototype, CSAIL researchers upgraded the AMOUR system. Several new features based on UWOC such as remote control, localization, and time division multiplexing access (TDMA) have been implemented into this underwater vehicles systems [157, 158]. In [159], the

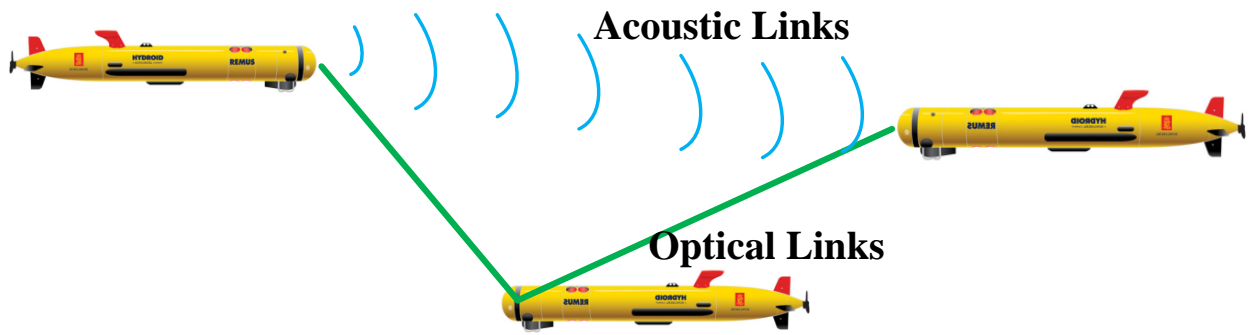
researchers demonstrated a cooperative UWSN that employed AMOUR, another different kind of AUV named Starbug and several underwater sensor nodes [160]. During the experiment, cooperative tasks such as data transmission, cooperative localization and navigation, as well as physical connection were performed. This work has proved the feasibility of cooperations among different underwater vehicles and sensor nodes. It also verified the plausible approach to achieve long-term operation of UWSNs. In [112], an upgraded underwater vehicle system AMOUR VI that embedded with UWOC module to achieve real-time control link was demonstrated. In this experiment, the CSAIL researchers used blue/green LEDs as light source and tested the system in a shallow swimming pool where ambient light existed. Human input device was used to control the orientation of the vehicle. Compared with the conventional acoustic ROVs which has a data rate up to hundred Kbps and latencies of hundred milliseconds, this UWOC system can achieve data rate on the order of Mbps and latencies on the order of one millisecond in a range of tens of meters. The architecture of the vehicle is compact. Both the transmitter and receiver modules are sealed in a transparent plastic cylinder with approximate length of 30cm and weight of two kilograms. The vehicles can also move in arbitrary directions with the embedded thruster system. The details of this thruster algorithm and its corresponding configurations were presented in [161]. Besides these research results that were proposed by MIT CSAIL, other UWOC research groups also presented several demos and prototypes on optical wireless underwater vehicles such as [6, 162, 163]. Hybrid communication systems which included both acoustic and optical modules were also implemented in several underwater vehicles [164, 165]. We will introduce them in the following section.

4.5 Hybrid Acoustic/Optical UWC Systems

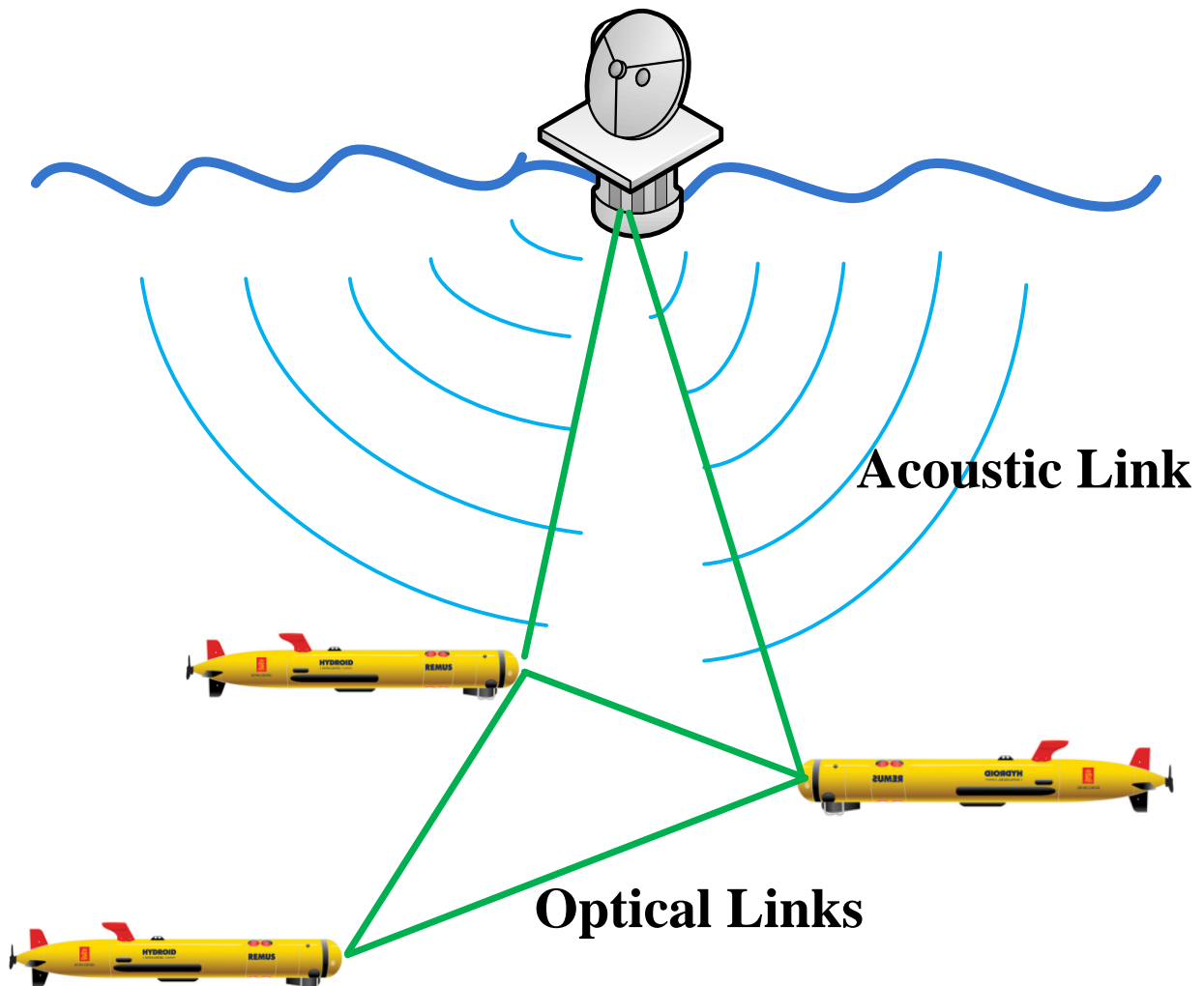
The performance of UWOC systems can be severely degraded by the absorption and scattering effects of sea water, channel turbulence, misalignment errors and other impact factors. All of these undesirable factors can cause frequent communication failure. Thus the reliability of UWOC system should be enhanced. Based on hybrid RF/FSO communication systems [98], one plausible method to increase the reliability of UWOC system is to employ acoustic wave as back-up scenario. Compared with UWOC, underwater acoustic communication method benefits from its mature technology, long link range and lower pointing requirements, but suffers from low data rate, low security and bulky instruments. On the other hand, UWOC systems can achieve high speed point-to-point data transmission, but can't operate in long distance and turbid environment. Considering the pros

and cons of these two methods, two typical hybrid link configurations have been proposed (Figure 4.4). The first configuration (Figure 4.4(a)) utilizes both acoustic wave and optical wave as duplex transmission medium. In this configuration, the two ends of the link are all mobile underwater vehicles that equipped with both acoustic and optical transceivers. When the two nodes of the link are in short distance and water condition is clear, the system will use optical wave as carrier to achieve high speed data transmission. If there is large distance between the two nodes or the water is turbid, the system will instead employ acoustic methods in order to accomplish connectivity. The virtue of this implementation is the high flexibility and reliability, but at the expense of high power consumption and bulky instruments due to acoustic transceivers on both ends. In the second configuration shown in Figure 4.4(b), the system is configured by one static control platform and several mobile sensor nodes. Acoustic wave is used as a broadcasting method to transmit control information in the downlink from control platform to each sensor node. While optical wave is applied in the communication links between each sensor node, as well as uplinks from sensor nodes to main control platform. This hybrid UWC system utilizes the advantages of each communication method. Since acoustic wave has diffusion property and long propagation distance, it can cover the area that is distributed with sensor nodes. Moreover, in the downlink from control platform to sensor nodes the transmitted information are low-speed control signals, which are suitable for acoustic communication. On the other hand, in the uplink of the system the large volume of oceanic monitoring data is transmitted through high speed UWOC links.

Based on these two hybrid UWOC link configurations, several related research have been proposed in recent years. In [164], researchers from the CSAIL of MIT reported a novel hybrid UWSNs that is capable of accomplishing long-term underwater monitoring tasks including video stream of sea floor, real time data of water temperature, pressure and other parameters. This hybrid UWSNs consist of two types of sensor nodes: static nodes and mobile nodes. Point-to-point communication between each node is accomplished using high-speed optical wave, while diffused broadcasting links are achieved through acoustic method. Moreover, the mobile nodes can also locate and move to the static nodes for data muling. The authors also demonstrated several optimizing algorithms and the corresponding hardware implementations of the system. Experimental results show that this hybrid data collection system can provide a much higher power and data transmission efficiency than the conventional acoustic underwater networks with multihop protocol. In [164], Vasilescu *et al.* proposed a more advanced hybrid underwater sensor network [166]. This underwater sensor network consists of several sensor nodes called *AquaNodes*. Each of the nodes contain an RF bluetooth



(a) Mutual hybrid UWOC configuration.



(b) Broadcasting hybrid UWOC configuration.

Figure 4.4: Two types of hybrid acoustic/optical UWC links.

module, an acoustic module and an optical module that operates with green light. Depending on the application environment, the users can communicate with each node through different means. For instance, in clear shallow water using optical signal, in water/air interface using bluetooth method. Furthermore, TDMA and self-synchronization technologies are also implemented in each node. According to the experimental results, this system can achieve a 400-meter long acoustic link with 300 bps data rate in ocean environment and establish an optical link up to eight meters with 330 kbps data rate. Based on this transmission speed, the data collected through the embedded sensors which include temperature, pressure, and water chemistry information can be continuously transmitted to the communication buoy, which will then relay the information to the onshore data center for following processing and analysis. Except these two hybrid UWOC systems demonstrated by MIT, scholars from other research institutions also proposed several discussions on hybrid UWOC topic. Farr *et al.* from the WHOI presented the operation concept of an untethered ROV (UTROV) that employs both optical and acoustic communication methods [167]. This vehicle can accomplish typical survey and reconnaissance tasks over a long distance using a low bandwidth acoustic modem. It can also communicate optically by employing a small ship-based or seafloor-based relay. Based on UTROV, the authors also demonstrated a seafloor borehole observatory system called circulation obviation retrofit kit optical telemetry system (CORK-OTS) in [168]. The CORK-OTS consist of several underwater ROVs and a surface vessel with lowered cable. At the lowered cable end, an acoustic modem was integrated with the optical system to send control information, while optical transceivers were implemented in both ROV and lowered cable end to achieve high speed data transmission. Although the details of testing this platform was not discussed, this research still provided a novel method to achieve seafloor observation.

Besides the experimental setups of hybrid UWOC, little theoretical research on this topic has occurred. In [169], the authors proposed a hybrid duplex optical-acoustic communication system. In this system, the downlink from the base station to the AUVs is a diffused acoustic link with low bandwidth and the uplinks are highly directional optical links with high bandwidth. The authors also discussed the factors that limited the performance of system which include refractive index variation, optical pointing error and acoustic latency. Another theoretical evaluation of hybrid underwater optical-acoustic network can be found in [170]. The researchers proposed a communication node equipped with both acoustic and optical transceivers. A transmission algorithm was designed and applied to each nodes to ensure the link alignment and connectivity. Simulation results show that the hybrid system has better energy efficiency than the pure acoustic system and is more

flexible to be applied in different water conditions.

4.6 Summary

In this chapter, we studied the the experimental setups and prototypes of UWOC from different aspects. We demonstrated the typical experimental setups of LOS UWOC systems and introduced the characterization of light sources and receivers that are commonly used in UWOC. We also discussed the development and state-of-the-art of several popular UWOC applications such as retroreflector, smart transceivers, underwater vehicles and hybrid UWOC systems. At the end of this chapter, we summarize all the discussed experimental UWOC systems in Table 4.1.

Table 4.1: Summary of literatures on experimental setups and prototypes of UWOC

Specified topics	Literatures	Comments
Typical LED-based LOS UWOC	[95], [79], [99, 100], [105, 106], [108–111], [119, 120], [124, 125] [7, 8, 131–134]	Relatively low cost; easy to be implemented; moderate speed and communication range.
Typical Laser-based LOS UWOC	[63, 85, 103, 128, 135–141, 171]	Higher cost; high speed; long communication range; Strict pointing.
Diffused LOS UWOC	[142], [143]	To achieve broadcasting UWOC.
NLOS UWOC	[144], [145]	To overcome underwater obstacles; few experiments were performed.
Retroreflector-based UWOC	[127, 150, 151]	Light and compact architecture with low cost and energy budget.
UWOC smart transceivers	[152], [107]	Adaptive transmission to improve link performance.
UWOC in underwater vehicles	[6, 112, 156–163]	With higher speed and less instruments budgets than acoustic method.
Hybrid UWOC systems	[164–170]	Improve system reliability.

Chapter 5

Outage Performance for Underwater Wireless Optical Links With Pointing Errors

In this chapter, we study the outage performance of vertical buoy-based UWOC links using IM/DD OOK with zero and nonzero boresight pointing errors. Firstly, we introduce the pointing error models with zero and nonzero boresight. Secondly, we introduce the beam spread function which describes the propagation of light in underwater environment. Thirdly, we analyze the outage probability with zero and nonzero boresight pointing errors. A closed-form outage probability with zero boresight pointing errors is achieved. We also derive the closed-form outage probability bounds with nonzero boresight pointing errors. These bounds can be made arbitrarily tight and approach the exact outage probability.

5.1 Pointing Errors Models

Similar to the definition of pointing errors in FSO communication, pointing errors in UWOC also include two components: boresight and jitter. The boresight is the fixed displacement between beam center and center of the detector, and the jitter is the random offset of the beam center at detector plane, which is mainly caused by random sea surface slopes [172]. In this section, we will first present the the pointing errors model with zero boresight, and then introduce the pointing error model with nonzero boresight.

5.1.1 Pointing Errors Model with Zero Boresight

The statistics of sea surface slopes has been studied during the past decades. Cox and Munk first measured the wave slope of random sea surface generated by wind. They concluded that the

surface slope approximately follows the Gaussian distribution with Gram-Charlier series ⁷ correction by taking into account the skewness and kurtosis [174]

$$P_r(s_x, s_y) = \frac{1}{2\pi\sigma_u\sigma_c} \exp \left[- \left(\frac{s_x^2}{2\sigma_u^2} + \frac{s_y^2}{2\sigma_c^2} \right) \right] \left[1 + \sum_{i,j=1}^{\infty} c_{ij} H_i(s_x) H_j(s_y) \right] \quad (5.1)$$

where $s_x = \partial z / \partial x$ and $s_y = \partial z / \partial y$ are defined as wave slopes of up/downwind and crosswind directions in the Cartesian coordinate (x, y, z) respectively; $H_i(s_x)H_j(s_y)$ is the product of Hermite polynomials with coefficients c_{ij} to be determined; σ_u^2 and σ_c^2 denote the variance of slopes in the up/downwind and crosswind directions, respectively. Based on the experimental results of Cox and Munk, σ_u^2 and σ_c^2 for the clean surface can be estimated as

$$\sigma_u^2 = 0.003 + 0.00192U \pm 0.002, \quad \sigma_c^2 = 0.00316U \pm 0.004 \quad (5.2)$$

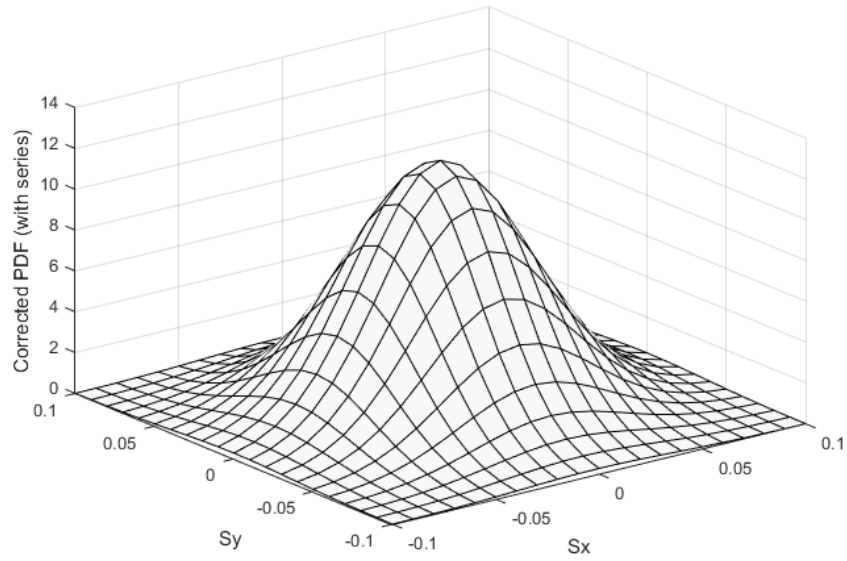
where U is the wind speed which is between 1 m/s and 14 m/s [174]. According to [174, eq. (18)], we expand the first 5 terms of the series in (5.1) as:

$$\begin{aligned} P'_r(s_x, s_y) = & \frac{1}{2\pi\sigma_u\sigma_c} \exp \left[- \left(\frac{s_x^2}{2\sigma_u^2} + \frac{s_y^2}{2\sigma_c^2} \right) \right] \\ & \times \left[1 - \frac{1}{2}c_{21} \left(\frac{s_x^2}{\sigma_u^2} - 1 \right) \frac{s_x^2}{\sigma_c^2} - \frac{1}{6}c_{03} \left(\frac{s_y^3}{\sigma_c^3} - 3\frac{s_x}{\sigma_c} \right) \right. \\ & + \frac{1}{24}c_{40} \left(\frac{s_x^4}{\sigma_u^4} - 6\frac{s_x^2}{\sigma_c^2} + 3 \right) + \frac{1}{4}c_{22} \left(\frac{s_x^2}{\sigma_u^2} - 1 \right) \left(\frac{s_y^2}{\sigma_c^2} - 1 \right) \\ & \left. + \frac{1}{24}c_{04} \left(\frac{s_y^4}{\sigma_c^4} - 6\frac{s_y^2}{\sigma_c^2} + 3 \right) + \dots \right]. \end{aligned} \quad (5.3)$$

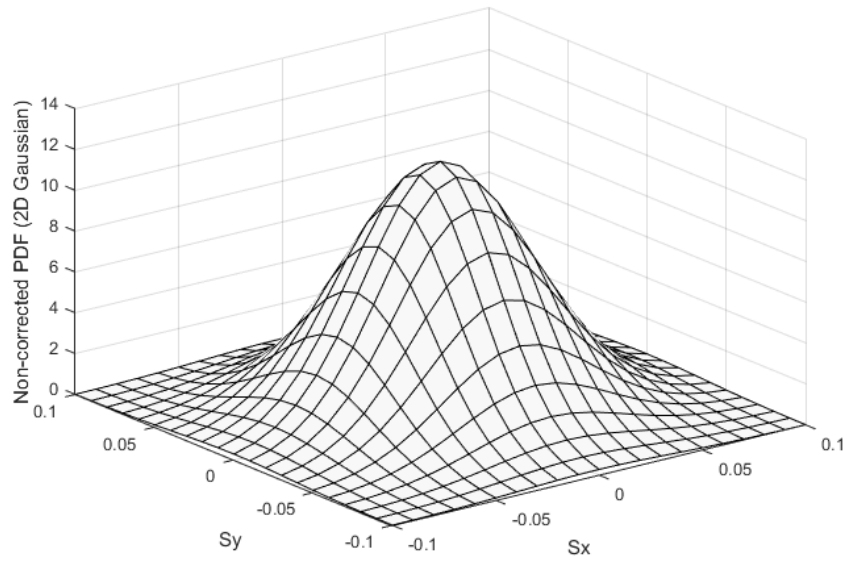
We substitute the values of $c_{21}, c_{03}, c_{40}, c_{22}, c_{04}$ of (5.3) from [174] and let $U = 5m/s$. The curves of (5.3) and two-dimensional Gaussian without multiplying the correction series are demonstrated in Figure 5.14(a) and Figure 5.14(b), respectively. Since σ_u^2 and σ_c^2 are small, the Gaussian function has a sharp peak, which means that the multiplied series have little impact on the PDF values for larger s_x and s_y . Considering these facts, we can simplify (5.3) as two dimensional zero-mean Gaussian distribution with different variances

$$\hat{P}_r(s_x, s_y) = \frac{1}{2\pi\sigma_u\sigma_c} \exp \left[- \left(\frac{s_x^2}{2\sigma_u^2} + \frac{s_y^2}{2\sigma_c^2} \right) \right]. \quad (5.4)$$

⁷Since Gram-Charlier series is an approximation to the unknown probability distribution using well-known distribution(Gaussian) and correction polynomials, the integral of the probability density function needs not integrate to one [173].



(a) Plot of corrected PDF (with series).



(b) Plot of non-corrected PDF (2D Gaussian without series).

Figure 5.1: Comparison between corrected and non-corrected PDF of ocean slopes.

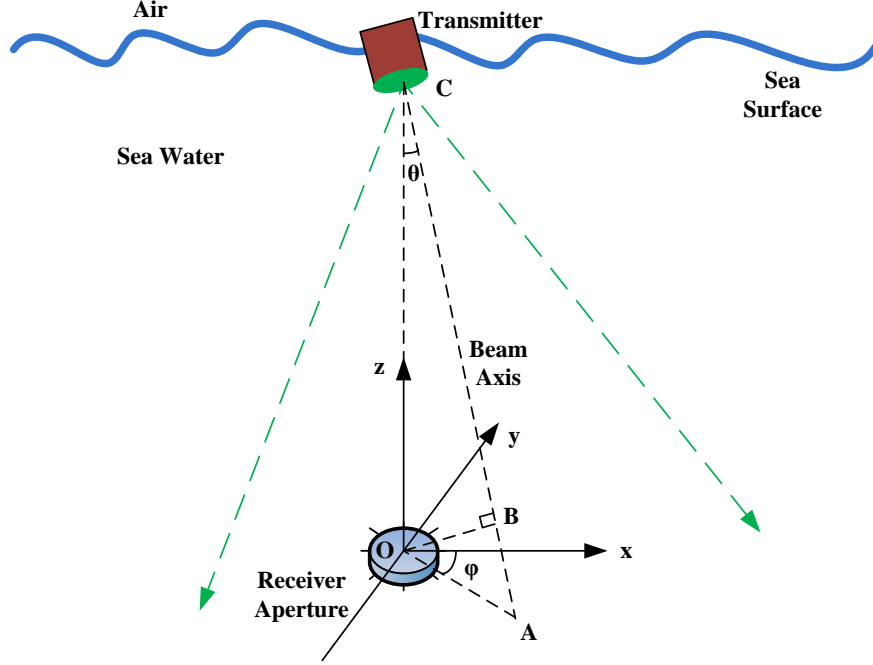


Figure 5.2: Geometry of the buoy-based UWOC. Figure 5.2 is adapted from [10].

According to [10], the geometry of buoy-based UWOC is demonstrated in Figure 5.2. A compact light source is placed on a sea surface buoy illuminating the receiver at the bottom plane. x and y axes represent the up/downwind and crosswind directions respectively [10]. xOy plane is the bottom plane parallel to the horizontal sea surface and z is the vertical axis perpendicular to the xOy plane. The centers of light source and receiver aperture are located at points of C and O respectively. A is the beam center at xOy plane and line AC represents the direction of beam axis with zenith angle θ measured from z axis. Azimuth angle of slope between OA and x axis is denoted as φ . OB is the normal of AC . The beam axis of the source remains the same direction as the normal of sea facet distributed as (5.4). When the surface is calm without any slopes, the link is assumed to be precisely aligned, which means the center of the light source is on the z axis [10].

When the wind speed is low ($1 \leq U \leq 7$ m/s), the slope angles are small, the light source has its center C approximately on z axis during the random slopes, i.e., $BC \approx OC = L$ [10]. Then in the case of small slope angle and the receiver with wide open field of view (FOV), the receiver can be treated as perpendicular to the beam axis with offset distance r from beam axis as $r \approx OB = L\sqrt{x_a^2 + y_a^2}/\sqrt{x_a^2 + y_a^2 + L^2}$ where (x_a, y_a) is the position of A in the Cartesian coordinate [10]. From Figure 5.2, (x_a, y_a) is given by $x_a = L \tan \theta \cos \varphi$ and $y_a = L \tan \theta \sin \varphi$. Then, the surface

slopes can be expressed as $s_x = \partial z / \partial x = \tan \theta \cos \varphi$ and $s_y = \partial z / \partial y = \tan \theta \sin \varphi$, which denote the relationship as $(x_a, y_a) = (Ls_x, Ls_y)$. By substituting this relationship into (5.4), the PDF of (x_a, y_a) can be presented as [10]

$$P_r(x_a, y_a) = \frac{1}{2\pi\sigma_u\sigma_c L^2} \exp \left[-\frac{1}{2L^2} \left(\frac{x_a^2}{\sigma_u^2} + \frac{y_a^2}{\sigma_c^2} \right) \right]. \quad (5.5)$$

From (5.5), we observe that x_a and y_a are independent zero mean Gaussian distributed RVs with different variances, i.e., $x_a \sim \mathcal{N}(0, \sigma_u^2 L^2)$, $y_a \sim \mathcal{N}(0, \sigma_c^2 L^2)$. After several mathematical derivations in Appendix I, the radial displacement $r = \sqrt{x_a^2 + y_a^2}$ which follows Hoyt or Nakagami-q distribution can be expressed as [175]

$$f_{r,HT}(r) = \frac{r}{q_H \sigma_u^2 L^2} \exp \left[-\frac{(1 + q_H^2) r^2}{4q_H^2 \sigma_u^2 L^2} \right] I_0 \left(\frac{(1 - q_H^2) r^2}{4q_H^2 \sigma_u^2 L^2} \right) \quad (5.6)$$

where $q_H = \sigma_c / \sigma_u \in (0, 1]$, $I_0(\cdot)$ is the modified Bessel function of the first kind with order zero. The plot of (5.6) is shown in Figure 5.3.

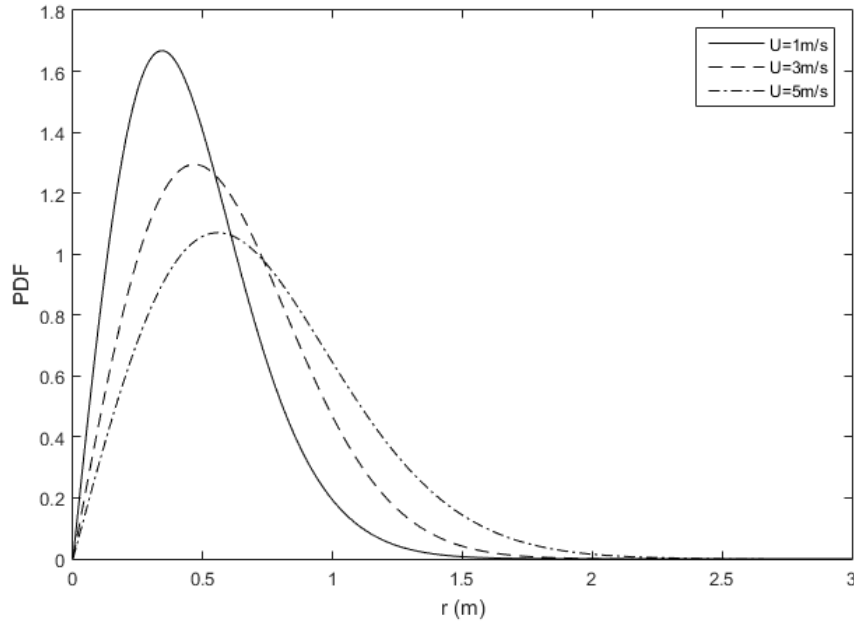


Figure 5.3: PDF of Hoyt distributed radial displacement r with $L = 5m$ and different values of wind speed U .

5.1.2 Pointing Errors Model with Nonzero Boresight

Although typical buoy-based vertical UWOC systems are initially installed with near zero boresight errors, mooring displacement of the buoy, ocean current and wind will still generate considerable boresight errors. Thus, it's necessary to take into account the impact of boresight errors in the vertical buoy-based UWOC system. Based on the foregoing derivations of (5.5), the pointing errors expression with nonzero boresight can be presented as:

$$P_r(x_a, y_a) = \frac{1}{2\pi\sigma_u\sigma_c L^2} \exp \left[-\frac{1}{2L^2} \left(\frac{(x_a - \mu_x)^2}{\sigma_u^2} + \frac{(y_a - \mu_y)^2}{\sigma_c^2} \right) \right] \quad (5.7)$$

where μ_x and μ_y are the means of two independent Gaussian random variables x_a and y_a , respectively. Using polar coordinates, i.e., $x_a = r \cos \theta$ and $y_a = r \sin \theta$, we obtain the radial displacement $r = \sqrt{x_a^2 + y_a^2}$ following the Beckmann distribution

$$f_{r,BM}(r) = \frac{r}{2\pi\sigma_u\sigma_c L^2} \int_0^{2\pi} \exp \left[-\frac{(r \cos \theta - \mu_x)^2}{2\sigma_u^2 L^2} - \frac{(r \sin \theta - \mu_y)^2}{2\sigma_c^2 L^2} \right] d\theta. \quad (5.8)$$

The Beckmann distribution is also known as generalized Rician distribution, which is used to describe the PDF of fading channels in general [172]. It specializes to the Hoyt distribution in (5.6) when $\mu_x = \mu_y = 0$, $\sigma_u \neq \sigma_c$. The plot of (5.8) is shown in Figure 5.4.

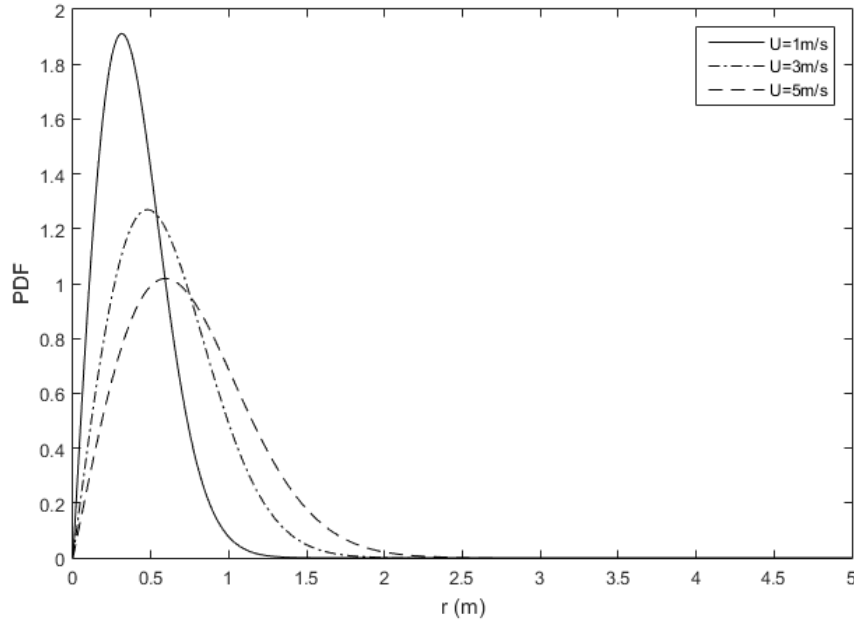


Figure 5.4: PDF of Beckmann distributed radial displacement r with $\mu_x = 0.01$, $\mu_y = 0.02$, $L = 5m$ and different values of wind speed U .

5.2 Beam Spread Function

Light propagation in underwater environment are severely impacted by absorption and scattering. The effects of absorption and scattering can be modeled by the beam-spread function (BSF) as [11]

$$B(L, r) = \frac{P_t}{2\pi\sigma_0^2} \exp\left(\frac{-r^2}{2\sigma_0^2}\right) \exp(-cL) + \frac{1}{2\pi} \int_0^\infty \frac{P_t}{2\pi\sigma_0^2} \exp\left(\frac{-r^2}{2\sigma_0^2}\right) \exp(-cL) \times \left\{ \exp\left[\int_0^L bp(v(L-z)) dz\right] - 1 \right\} J_0(vr) v dv \quad (5.9)$$

where P_t is the transmission power; σ_0^2 is the variance of Gaussian beam; L denotes the link distance, c presents the light attenuation coefficient in underwater environment; b is the light scattering coefficient; and v denotes the spatial frequency. In (5.9) $J_0(\cdot)$ is Bessel function of the first kind of order 0. $p(v) = \frac{1}{2} \int_0^\pi p(\beta) J_0(v\beta) \beta d\beta$ is the Hankel transform of the scattering phase function. The commonly used Henyey-Greenstein (HG) function is adopted as the scattering phase function

$$p(\beta) = \frac{1 - g^2}{4\pi(1 + g^2 - 2g \cos \beta)^{\frac{3}{2}}} \quad (5.10)$$

where g is the average cosine of β in all scattering directions. We adopt $g = 0.924$ [50]. The physical meaning of $B(L, r)$ is the light irradiance with displacement r from the beam center axis with perpendicular distance L (Figure 5.5).

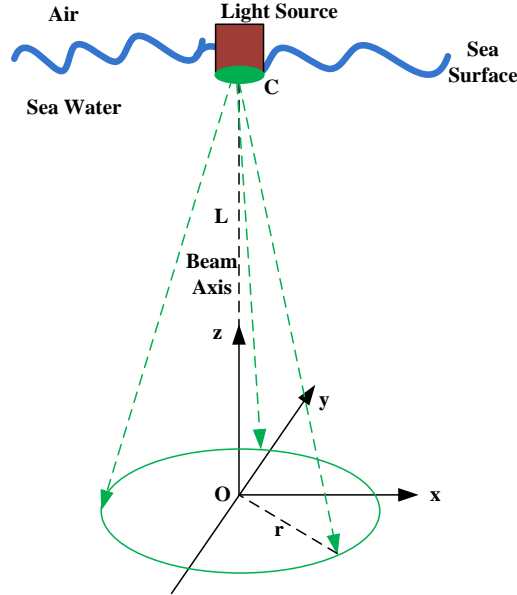


Figure 5.5: Geometry for BSF.

The values of $B(L, r)$ with different values of r have also been calculated and verified through water tank experiments in [11]. The normalized values of (5.9) can be found in Figure 5.6 [11]. We also plot the non-normalized values of (5.9) with respect to r for different transmission power P_t in Figure 5.7.

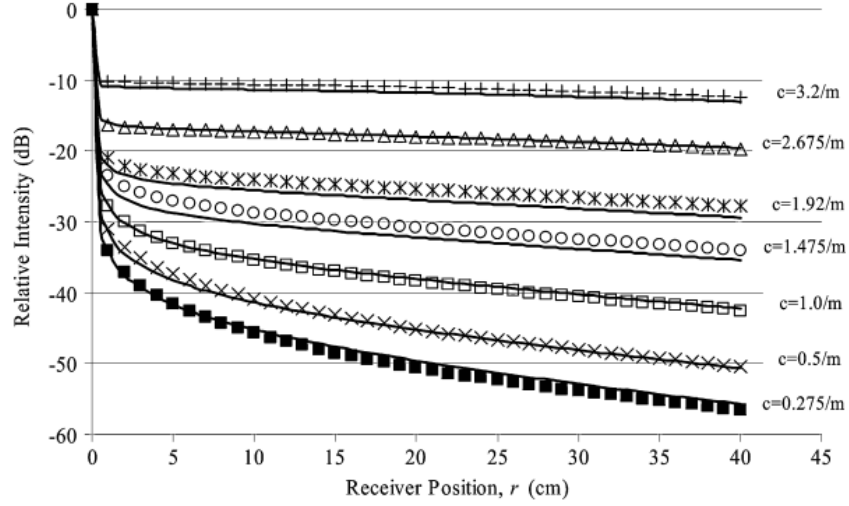


Figure 5.6: BSF results for $L = 3.63m$ with different attenuation coefficients c . Model results shown as lines. Experimental data shown as points. Relative intensity is the received power with displacement r normalized by the power without displacement $B(L, r)/B(L, 0)$ [11]. Figure 5.6 is reprinted from [11].

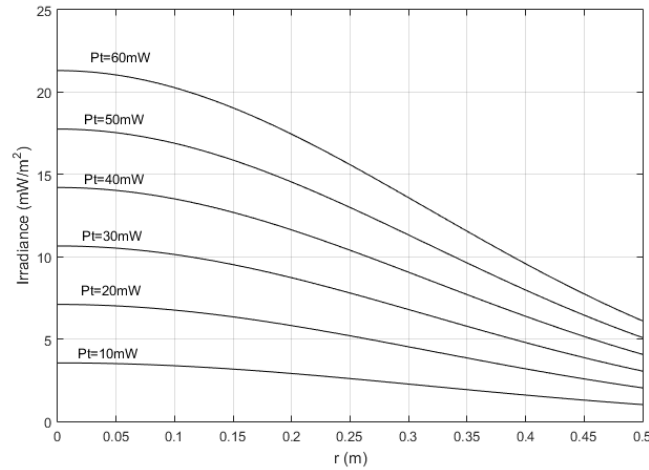


Figure 5.7: BSF values for $L = 5m$ and $c = 0.3$ with different values of transmission power P_t .

For typical optical detector, the receiver aperture is on the order of centimeters which is narrow enough. Hence, we can derive the received power P_r directly from (5.9) without integrating $B(L, r)$ in the aperture area as [10]

$$P_r(r) = \frac{\pi D^2}{4} B(L, r) \quad (5.11)$$

where D is the diameter of the aperture, r is a random variable follows Hoyt or Beckmann distribution in (5.6) and (5.8) respectively.

5.3 Outage Probability with Zero Boresight Pointing Errors

In this section, we derive the outage probability with zero boresight pointing errors. We assume that there's a displacement r on the receiver plane between the beam center and the receiver aperture center. According to (5.11), the received power is $P_r(r)$. When $P_r(r)$ is less than a threshold γ_{th} ⁸, outage occurs. Thus we define the outage probability as

$$P_{out} = \text{Prob}(P_r(r) < \gamma_{th}). \quad (5.12)$$

From Figure 5.6, we observe that $P_r(r)$ is monotonically decreasing in r . Equivalently, we have

$$P_{out} = \text{Prob}(r > P_r^{-1}(\gamma_{th})). \quad (5.13)$$

Since deriving the inverse function $r = P_r^{-1}(\gamma_{th})$ is intractable, we can obtain the value of r by looking up the numerical table of $B(L, r)$ such as Figure 5.7.

In Figure 5.8, the receiver aperture is located at the center of the circle O . The radius of the circle is $P_r^{-1}(\gamma_{th})$. The probability that the beam center doesn't locate inside the circle is the outage probability which can be derived by integrating the PDF of Hoyt distribution in (5.6)

$$P_{out,HT} = \text{Prob}(r > P_r^{-1}(\gamma_{th})) = \int_{P_r^{-1}(\gamma_{th})}^{\infty} f_{r,HT}(r) dr = 1 - \int_0^{P_r^{-1}(\gamma_{th})} f_{r,HT}(r) dr \quad (5.14)$$

where $\int_0^{P_r^{-1}(\gamma_{th})} f_{r,HT}(r) dr$ is the cumulative distribution function (CDF) of Hoyt distribution evaluated at $P_r^{-1}(\gamma_{th})$. After mathematical derivations shown in Appendix II, we obtain the outage

⁸ γ_{th} can be regarded as a constant here. It is determined by the inverse function of instantaneous capacity $C^{-1}(R_0)$ [172], where R_0 is the transmission data rate.

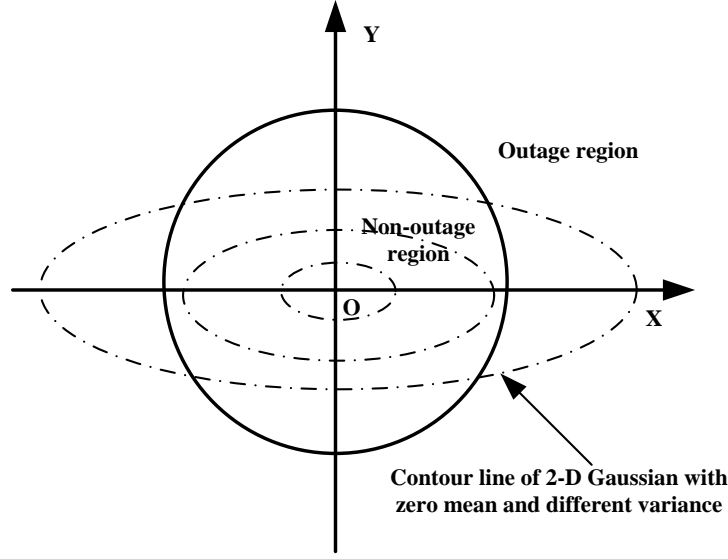


Figure 5.8: Demonstration of outage region.

probability with zero boresight pointing errors as

$$\begin{aligned}
 P_{out,HT} = & 1 - \frac{1}{\sqrt{1+q_H^2}} \left[Q_1 \left(\frac{\sqrt{\frac{1+q_H}{1-q_H}} \sqrt{1-q_H^4 P_r^{-1}(\gamma_{th})}}{2q_H \sqrt{1+q_H^2 \sigma_u L}}, \frac{\sqrt{\frac{1-q_H}{1+q_H}} \sqrt{1-q_H^4 P_r^{-1}(\gamma_{th})}}{2q_H \sqrt{1+q_H^2 \sigma_u L}} \right) \right. \\
 & \left. - Q_1 \left(\frac{\sqrt{\frac{1-q_H}{1+q_H}} \sqrt{1-q_H^4 P_r^{-1}(\gamma_{th})}}{2q_H \sqrt{1+q_H^2 \sigma_u L}}, \frac{\sqrt{\frac{1+q_H}{1-q_H}} \sqrt{1-q_H^4 P_r^{-1}(\gamma_{th})}}{2q_H \sqrt{1+q_H^2 \sigma_u L}} \right) \right] \quad (5.15)
 \end{aligned}$$

where $Q_1(a, b) = \int_b^\infty \exp\left(-\frac{x^2+a^2}{2}\right) I_0(ax) dx$ is the first-order Marcum Q-function.

5.4 Bounds of Outage Probability with Nonzero Boresight Pointing Errors

Following the similar approach of deriving the outage probability with zero boresight pointing errors, we can also express the outage probability with nonzero boresight pointing errors as

$$\begin{aligned}
 P_{out,BM} = & \text{Prob}(r > P_r^{-1}(\gamma_{th})) = \int_{P_r^{-1}(\gamma_{th})}^\infty f_{r,BM}(r) dr = 1 - \int_0^{P_r^{-1}(\gamma_{th})} f_{r,BM}(r) dr \\
 = & 1 - \int_0^{P_r^{-1}} \frac{r}{2\pi\sigma_u\sigma_c L^2} \int_0^{2\pi} \exp\left[-\frac{(r \cos \theta - \mu_x)^2}{2\sigma_u^2 L^2} - \frac{(r \sin \theta - \mu_y)^2}{2\sigma_c^2 L^2}\right] d\theta dr \quad (5.16)
 \end{aligned}$$

where $\int_0^{P_r^{-1}(\gamma_{th})} f_{r,BM}(r)dr$ is the CDF of Beckmann distribution evaluated at $P_r^{-1}(\gamma_{th})$. We notice that the double integral in (5.16) is intractable, thus it's necessary to derive the lower and upper bounds of the outage probability with nonzero boresight instead.

5.4.1 Lower Bound of Outage Probability with Nonzero Boresight

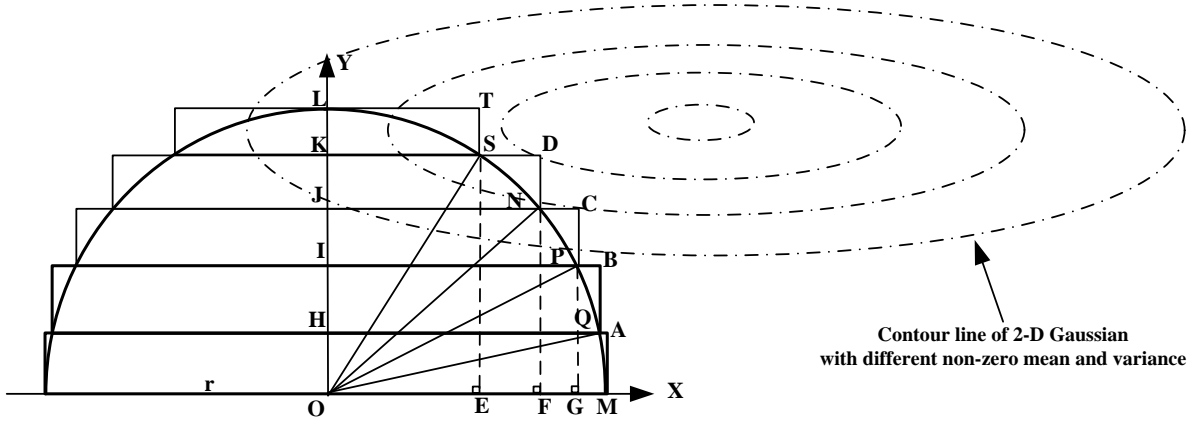


Figure 5.9: Integrating region for lower bound of outage probability.

$$\begin{array}{cc} \left(-\sqrt{r^2 - \left(\frac{(n-1)r}{N} \right)^2}, \frac{nr}{N} \right) A & C \left(\sqrt{r^2 - \left(\frac{(n-1)r}{N} \right)^2}, \frac{nr}{N} \right) \\ \left(-\sqrt{r^2 - \left(\frac{(n-1)r}{N} \right)^2}, \frac{(n-1)r}{N} \right) B & D \left(\sqrt{r^2 - \left(\frac{(n-1)r}{N} \right)^2}, \frac{(n-1)r}{N} \right) \end{array}$$

Figure 5.10: Coordinates of nth circumscribed rectangle on the upper semicircle.

In Figure 5.9, we construct several rectangles with the same height circumscribed the upper semi-circle of non-outage region. Since the radius of the circle is r and $HO = IH = JI = KJ = LK = \frac{r}{5}$, we utilize pythagorean theorem to derive the coordinates of each rectangle vertexes as: $M(r, 0)$, $A(r, \frac{r}{5})$, $Q\left(\sqrt{r^2 - \left(\frac{r}{5}\right)^2}, \frac{r}{5}\right)$, $B\left(\sqrt{r^2 - \left(\frac{r}{5}\right)^2}, \frac{2r}{5}\right)$, $P\left(\sqrt{r^2 - \left(\frac{2r}{5}\right)^2}, \frac{2r}{5}\right)$, $C\left(\sqrt{r^2 - \left(\frac{2r}{5}\right)^2}, \frac{3r}{5}\right)$, $N\left(\sqrt{r^2 - \left(\frac{3r}{5}\right)^2}, \frac{3r}{5}\right)$, $D\left(\sqrt{r^2 - \left(\frac{3r}{5}\right)^2}, \frac{4r}{5}\right)$, $S\left(\sqrt{r^2 - \left(\frac{4r}{5}\right)^2}, \frac{4r}{5}\right)$, $T\left(\sqrt{r^2 - \left(\frac{4r}{5}\right)^2}, \frac{5r}{5}\right)$. Other coordinates of rectangle vertexes in the quadrant II of Figure 5.9 can be obtained through the symmetry property.

Considering the general case, we circumscribe $N(N \geq 2)$ rectangles with the same height of $\frac{r}{N} = \frac{P_r^{-1}(\gamma_{th})}{N}$ on the upper semicircle in Figure 5.9. Following the derivation process of $N = 5$, the vertex coordinates of n th rectangle can be presented as Figure 5.10. Thus the integration of (5.7) over n th rectangle region can be expressed as

$$P_{unit,BM}(P_r^{-1}(\gamma_{th})) = \int_{\frac{(n-1)P_r^{-1}(\gamma_{th})}{N}}^{\frac{nP_r^{-1}(\gamma_{th})}{N}} \int_{-\sqrt{P_r^{-1}(\gamma_{th})^2 - \left(\frac{(n-1)P_r^{-1}(\gamma_{th})}{N}\right)^2}}^{\sqrt{P_r^{-1}(\gamma_{th})^2 - \left(\frac{(n-1)P_r^{-1}(\gamma_{th})}{N}\right)^2}} \frac{1}{2\pi\sigma_u\sigma_c L^2} \times \exp\left[-\frac{1}{2L^2} \left(\frac{(x_a - \mu_x)^2}{\sigma_u^2} + \frac{(y_a - \mu_y)^2}{\sigma_c^2}\right)\right] dx_a dy_a, N \geq 2. \quad (5.17)$$

Since x_a and y_a are independent, we integrate x_a and y_a separately and obtain

$$P_{unit,BM}(P_r^{-1}(\gamma_{th})) = \frac{1}{4} \left[\operatorname{erf}\left(\frac{\mu_y - \frac{(n-1)P_r^{-1}(\gamma_{th})}{N}}{\sqrt{2}\sigma_c L}\right) - \operatorname{erf}\left(\frac{\mu_y - \frac{nP_r^{-1}(\gamma_{th})}{N}}{\sqrt{2}\sigma_c L}\right) \right] \times \left[\operatorname{erf}\left(\frac{\mu_x + \sqrt{P_r^{-1}(\gamma_{th})^2 - \left(\frac{(n-1)P_r^{-1}(\gamma_{th})}{N}\right)^2}}{\sqrt{2}\sigma_u L}\right) - \operatorname{erf}\left(\frac{\mu_x - \sqrt{P_r^{-1}(\gamma_{th})^2 - \left(\frac{(n-1)P_r^{-1}(\gamma_{th})}{N}\right)^2}}{\sqrt{2}\sigma_u L}\right) \right], N \geq 2. \quad (5.18)$$

where $\operatorname{erf}(x) = \frac{2}{\sqrt{\pi}} \int_0^x e^{-t^2} dt$ is the error function. Taking summation to (5.18), we derive the integration of (5.7) over the whole rectangle region circumscribed the upper semicircle in Figure 5.9 as

$$P_{LB1,BM}(P_r^{-1}(\gamma_{th})) = \frac{1}{4} \sum_{n=1}^N \left[\operatorname{erf}\left(\frac{\mu_y - \frac{(n-1)P_r^{-1}(\gamma_{th})}{N}}{\sqrt{2}\sigma_c L}\right) - \operatorname{erf}\left(\frac{\mu_y - \frac{nP_r^{-1}(\gamma_{th})}{N}}{\sqrt{2}\sigma_c L}\right) \right] \times \left[\operatorname{erf}\left(\frac{\mu_x + \sqrt{P_r^{-1}(\gamma_{th})^2 - \left(\frac{(n-1)P_r^{-1}(\gamma_{th})}{N}\right)^2}}{\sqrt{2}\sigma_u L}\right) - \operatorname{erf}\left(\frac{\mu_x - \sqrt{P_r^{-1}(\gamma_{th})^2 - \left(\frac{(n-1)P_r^{-1}(\gamma_{th})}{N}\right)^2}}{\sqrt{2}\sigma_u L}\right) \right], N \geq 2. \quad (5.19)$$

Following the similar process of deriving (5.19), we express the integration of (5.7) over the entire rectangle region circumscribed the lower semicircle as

$$\begin{aligned}
 P_{LB2,BM} (P_r^{-1}(\gamma_{th})) = & \frac{1}{4} \sum_{n=1}^N \left[\operatorname{erf} \left(\frac{\mu_y + \frac{n P_r^{-1}(\gamma_{th})}{N}}{\sqrt{2} \sigma_c L} \right) - \operatorname{erf} \left(\frac{\mu_y + \frac{(n-1) P_r^{-1}(\gamma_{th})}{N}}{\sqrt{2} \sigma_c L} \right) \right] \\
 & \times \left[\operatorname{erf} \left(\frac{\mu_x + \sqrt{P_r^{-1}(\gamma_{th})^2 - \left((n-1) \frac{P_r^{-1}(\gamma_{th})}{N} \right)^2}}{\sqrt{2} \sigma_u L} \right) \right. \\
 & \left. - \operatorname{erf} \left(\frac{\mu_x - \sqrt{P_r^{-1}(\gamma_{th})^2 - \left((n-1) \frac{P_r^{-1}(\gamma_{th})}{N} \right)^2}}{\sqrt{2} \sigma_u L} \right) \right], N \geq 2.
 \end{aligned} \tag{5.20}$$

According to (5.19) and (5.20), the lower bound of Beckmann CDF evaluated at $P_r^{-1}(\gamma_{th})$ is presented as

$$F_{r,LB} (P_r^{-1}(\gamma_{th})) = P_{LB1,BM} (P_r^{-1}(\gamma_{th})) + P_{LB2,BM} (P_r^{-1}(\gamma_{th})). \tag{5.21}$$

Thus the lower bound of outage probability with nonzero boresight pointing errors can be expressed as

$$P_{out,BM} \geq 1 - F_{r,LB} (P_r^{-1}(\gamma_{th})) = 1 - P_{LB1,BM} (P_r^{-1}(\gamma_{th})) - P_{LB2,BM} (P_r^{-1}(\gamma_{th})). \tag{5.22}$$

5.4.2 Upper Bound of Outage Probability with Nonzero Boresight

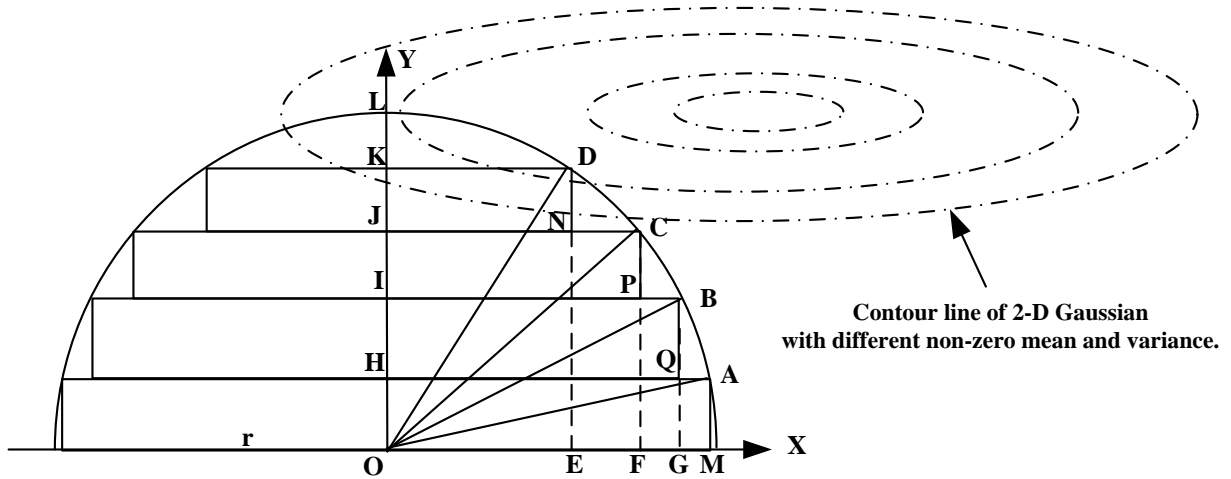


Figure 5.11: Divide half of the non-outage region into several rectangles with the same height.

In Figure 5.11, we construct several rectangles with the same height inscribed in the upper semi-circle of the non-outage region. Since the radius of the circle is r and $OH = IH = JI = KJ =$

$LK = \frac{r}{5}$, we utilize pythagorean theorem to derive the coordinates of each rectangle vertexes as: $M \left(\sqrt{r^2 - \left(\frac{r}{5}\right)^2}, 0 \right)$, $A \left(\sqrt{r^2 - \left(\frac{r}{5}\right)^2}, \frac{r}{5} \right)$, $B \left(\sqrt{r^2 - \left(\frac{2r}{5}\right)^2}, \frac{2r}{5} \right)$, $Q \left(\sqrt{r^2 - \left(\frac{2r}{5}\right)^2}, \frac{r}{5} \right)$, $C \left(\sqrt{r^2 - \left(\frac{3r}{5}\right)^2}, \frac{3r}{5} \right)$, $P \left(\sqrt{r^2 - \left(\frac{3r}{5}\right)^2}, \frac{2r}{5} \right)$, $D \left(\sqrt{r^2 - \left(\frac{4r}{5}\right)^2}, \frac{4r}{5} \right)$, $N \left(\sqrt{r^2 - \left(\frac{4r}{5}\right)^2}, \frac{3r}{5} \right)$. Other coordinates of rectangle vertexes in the quadrant *II* of Figure 5.11 can be obtained through the symmetry property.

Considering the general case, we inscribe $N - 1$ ($N \geq 2$) rectangles with the same height of $\frac{r}{N} = \frac{P_r^{-1}(\gamma_{th})}{N}$ on the upper semicircle in Figure 5.11. Following the derivation process of $N = 5$, the vertex coordinates of n th rectangle can be presented as Figure 5.12.

$$\begin{aligned}
 & \left(-\sqrt{r^2 - \left(\frac{nr}{N}\right)^2}, \frac{nr}{N} \right) A \quad \left(\sqrt{r^2 - \left(\frac{nr}{N}\right)^2}, \frac{nr}{N} \right) C \\
 & \left(-\sqrt{r^2 - \left(\frac{nr}{N}\right)^2}, \frac{(n-1)r}{N} \right) B \quad \left(\sqrt{r^2 - \left(\frac{nr}{N}\right)^2}, \frac{(n-1)r}{N} \right) D
 \end{aligned}$$

Figure 5.12: Coordinates of n th inscribed rectangle on the upper semicircle.

Following the similar process in Section 5.4.1, we express the integration of (5.7) over the entire rectangle region inscribed the upper semicircle as

$$\begin{aligned}
 P_{UB1,BM} (P_r^{-1}(\gamma_{th})) &= \frac{1}{4} \sum_{n=1}^{N-1} \left[\operatorname{erf} \left(\frac{\mu_y - \frac{(n-1)P_r^{-1}(\gamma_{th})}{N}}{\sqrt{2}\sigma_c L} \right) - \operatorname{erf} \left(\frac{\mu_y - \frac{nP_r^{-1}(\gamma_{th})}{N}}{\sqrt{2}\sigma_c L} \right) \right] \\
 &\quad \times \left[\operatorname{erf} \left(\frac{\mu_x + \sqrt{P_r^{-1}(\gamma_{th})^2 - \left(n \frac{P_r^{-1}(\gamma_{th})}{N}\right)^2}}{\sqrt{2}\sigma_u L} \right) \right. \\
 &\quad \left. - \operatorname{erf} \left(\frac{\mu_x - \sqrt{P_r^{-1}(\gamma_{th})^2 - \left(n \frac{P_r^{-1}(\gamma_{th})}{N}\right)^2}}{\sqrt{2}\sigma_u L} \right) \right], N \geq 2.
 \end{aligned} \tag{5.23}$$

For the integration over the entire rectangle region inscribed the lower semicircle, we have

$$\begin{aligned}
 P_{UB_2,BM} (P_r^{-1}(\gamma_{th})) &= \frac{1}{4} \sum_{n=1}^{N-1} \left[\operatorname{erf} \left(\frac{\mu_y + \frac{n P_r^{-1}(\gamma_{th})}{N}}{\sqrt{2} \sigma_c L} \right) - \operatorname{erf} \left(\frac{\mu_y + \frac{(n-1) P_r^{-1}(\gamma_{th})}{N}}{\sqrt{2} \sigma_c L} \right) \right] \\
 &\quad \times \left[\operatorname{erf} \left(\frac{\mu_x + \sqrt{P_r^{-1}(\gamma_{th})^2 - \left(n \frac{P_r^{-1}(\gamma_{th})}{N} \right)^2}}{\sqrt{2} \sigma_u L} \right) \right. \\
 &\quad \left. - \operatorname{erf} \left(\frac{\mu_x - \sqrt{P_r^{-1}(\gamma_{th})^2 - \left(n \frac{P_r^{-1}(\gamma_{th})}{N} \right)^2}}{\sqrt{2} \sigma_u L} \right) \right], N \geq 2.
 \end{aligned} \tag{5.24}$$

According to (5.23) and (5.24), the upper bound of Beckmann CDF evaluated at $P_r^{-1}(\gamma_{th})$ is presented as

$$F_{r,UB} (P_r^{-1}(\gamma_{th})) = P_{UB_1,BM} (P_r^{-1}(\gamma_{th})) + P_{UB_2,BM} (P_r^{-1}(\gamma_{th})). \tag{5.25}$$

Thus the upper bound of outage probability with nonzero boresight pointing errors can be expressed as

$$P_{out,BM} \geq 1 - F_{r,UB} (P_r^{-1}(\gamma_{th})) = 1 - P_{UB_1,BM} (P_r^{-1}(\gamma_{th})) - P_{UB_2,BM} (P_r^{-1}(\gamma_{th})). \tag{5.26}$$

5.4.3 Discussion on the Tightness of the Outage Probability Bounds

In (5.22) and (5.26), we have, respectively, showed the lower and upper bounds of outage probability with nonzero boresight pointing errors. In order to prove that the outage probability bounds can be made arbitrarily tight and approach the exact outage probability, we are required to prove that the bounds of Beckmann CDF approaches the exact CDF of Beckmann distribution. Thus, we need to prove that for any given radius of circle $r (r \geq 0)$

$$\lim_{N \rightarrow \infty} |F_{r,LB} (r) - F_{r,UB} (r)| = 0 \tag{5.27}$$

or equivalently,

$$\lim_{N \rightarrow \infty} \left[\sum 2 (S_{LB} - S_{UB}) \right] = 0 \tag{5.28}$$

where S_{LB} and S_{UB} denote the integration area of one rectangle for calculating lower and upper bounds of Beckmann CDF respectively (Figure 5.13).

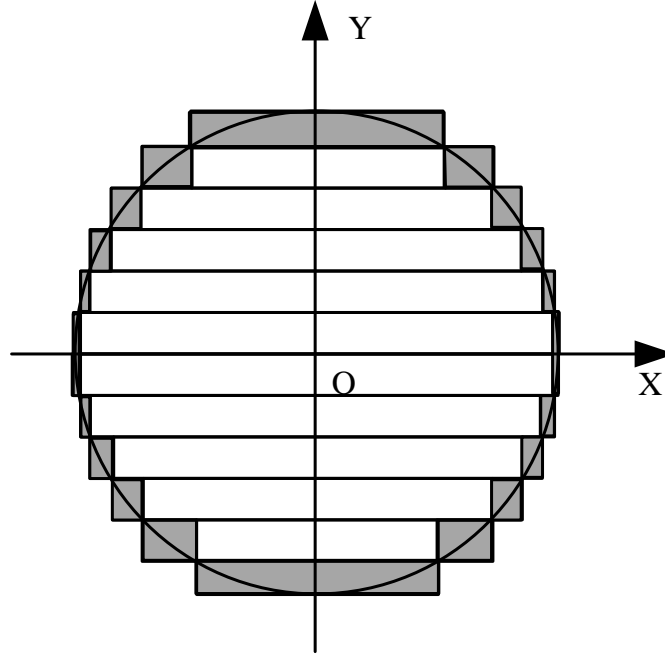


Figure 5.13: Demonstration of the area $S_{shade} = \sum 2(S_{LB} - S_{UB})$. A factor of 2 indicates the symmetry of rectangle area in lower and upper semicircles.

In Figure 5.9, the area of one rectangle is $S_{LB} = \frac{2r}{N} \sqrt{r^2 - (n-1)^2 \frac{r^2}{N^2}}$. Similarly, we can also obtain the area of one rectangle in Figure 5.11 as $S_{UB} = \frac{2r}{N} \sqrt{r^2 - n^2 \frac{r^2}{N^2}}$. Thus (5.28) can be expressed as

$$\begin{aligned} \lim_{N \rightarrow \infty} \sum 2(S_{LB} - S_{UB}) &= \lim_{N \rightarrow \infty} \left[\sum_{n=1}^{N-1} \left(\frac{4r}{N} \sqrt{r^2 - (n-1)^2 \frac{r^2}{N^2}} - \frac{4r}{N} \sqrt{r^2 - n^2 \frac{r^2}{N^2}} \right) + \frac{4r^2}{N^2} \right] \\ &= \lim_{N \rightarrow \infty} \left[\sum_{n=1}^{N-1} \frac{4r^2}{N^2} \left(\sqrt{N^2 - (n-1)^2} - \sqrt{N^2 - n^2} \right) + \frac{4r^2}{N^2} \right] \end{aligned} \quad (5.29)$$

where $\sum_{n=1}^{N-1} \left(\sqrt{N^2 - (n-1)^2} - \sqrt{N^2 - n^2} \right) = N - \sqrt{2N-1}$. Then (5.29) can be presented as:

$$\begin{aligned} \lim_{N \rightarrow \infty} 2(S_{LB} - S_{UB}) &= \lim_{N \rightarrow \infty} \left[\frac{4r^2}{N^2} (N - \sqrt{2N-1}) + \frac{4r^2}{N^2} \right] \\ &= \lim_{N \rightarrow \infty} \left[\frac{4r^2}{N^2} (N - \sqrt{2N-1}) \right] + \lim_{N \rightarrow \infty} \left(\frac{4r^2}{N^2} \right) \\ &= 0. \end{aligned} \quad (5.30)$$

Thus we have $\lim_{N \rightarrow \infty} \sum 2(S_{LB} - S_{UB}) = 0$. We conclude that the limit in (5.27) holds and that the lower and upper bounds of Beckmann CDF in (5.21) and (5.25) can be made approach the exact CDF of Beckmann distribution. The bounds of outage probability in (5.22) and (5.26) can also approach the exact outage probability in (5.16) with arbitrary accuracy.

5.5 Numerical Results

In this section, we adopt a 532 nm laser source and the system settings shown in Table 5.1 [10, 11]. Based on these parameters, we carry out the outage performance of a vertical bouy-based UWOC system.

Table 5.1: Summary of simulation parameters

Parameters	$c(\lambda)$	σ_0	L	D	γ_{th}	Rx FOV	Tx divergence
Values	$2.19/0.3m^{-1}$	0.1	$5m/10m$	5 cm	0.01	180°	0.01°

5.5.1 Outage Probability with Zero Boresight Pointing Errors

The outage probability with nonzero boresight pointing errors in (5.15) is evaluated and verified through Monte Carlo simulation in both coastal and harbor water. Figures 5.14 and 5.15 demonstrate the outage probability with different transmit power for 5m and 10m link distance in costal and harbor water, respectively.

By comparing Figure 5.14 and Figure 5.15, we have found that the decrement of transmit power or increment of wind speed can increase the outage probability. We also observe that, with the same transmit power, the increase of water turbidity and link distance will also degrade the outage performance. In Figure 5.15, the outage probability increases from 10^{-10} to 10^{-2} approximately as the wind speed U increases from 2 m/s to 5 m/s when the transmit power is fixed at 15 dBm in coastal water. While in harbor water which is more turbid, the outage probability changes from 10^{-11} to 10^{-7} as U varies for a fixed transmit power of 18 dBm, which indicates that the outage probability is less sensitive to the wind speed in harbor water than that in coastal water. Similar phenomena can be observed from Figure 5.14 for a relatively short link range of 5 m. Hence, the increment of seawater turbidity may diminish the outage performance degradation caused by the wind and enhances the link reliability. This is due to the fact that the multiple scattering process in turbid medium may strongly spread the beam spatially [10].

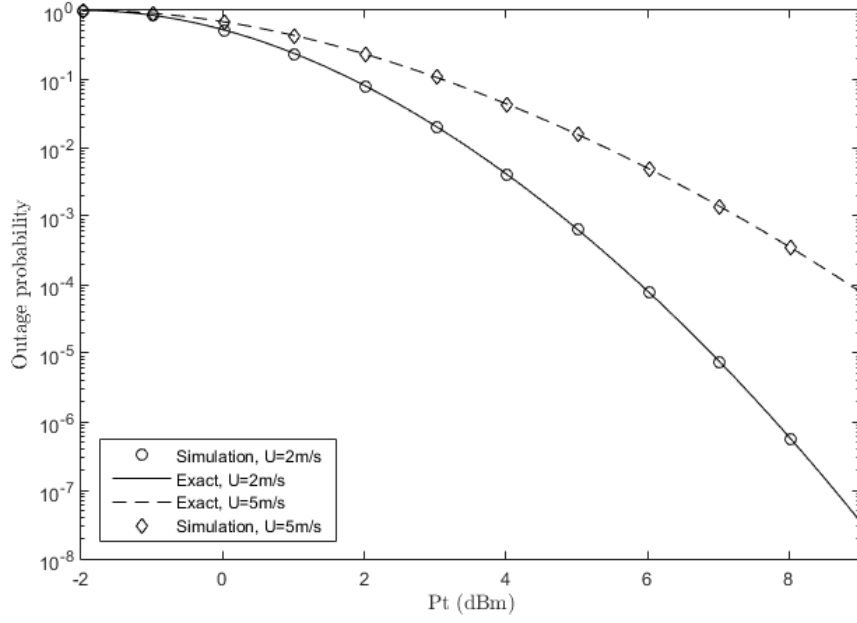
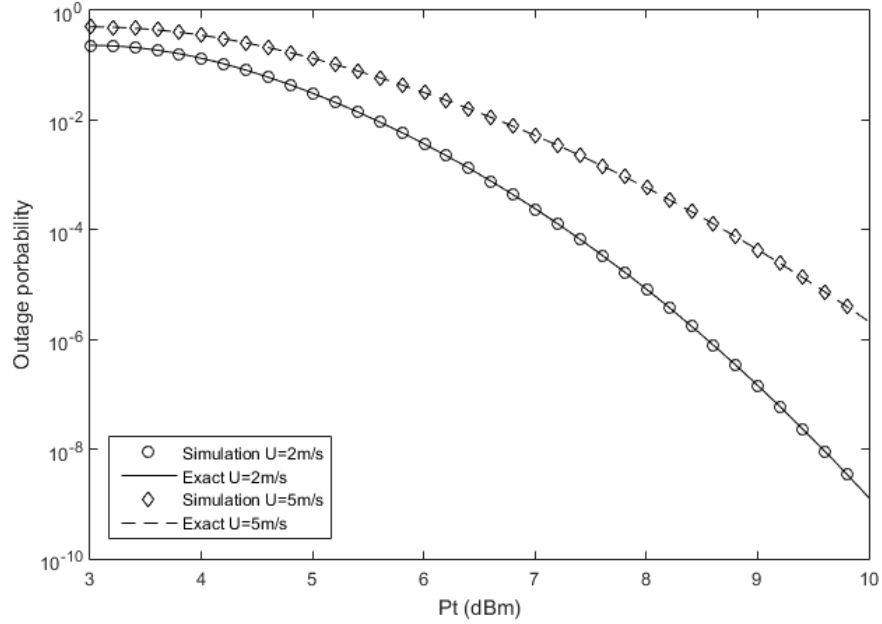

 (a) Coastal water $c = 0.3/m$.

 (b) Harbor water $c = 2.19/m$.

Figure 5.14: Outage probability of a vertical buoy-based UWOC system with zero boresight pointing errors. Link distance $L = 5m$

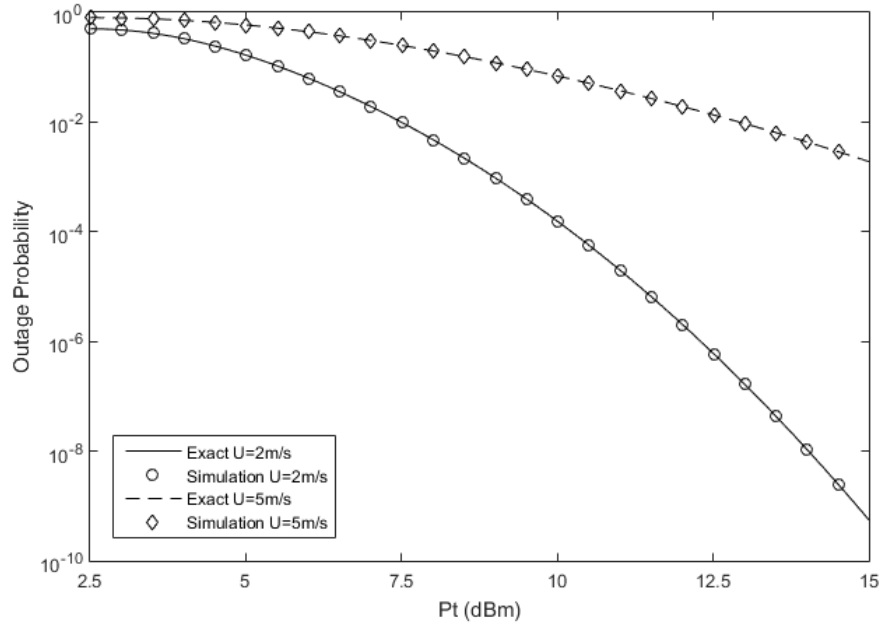
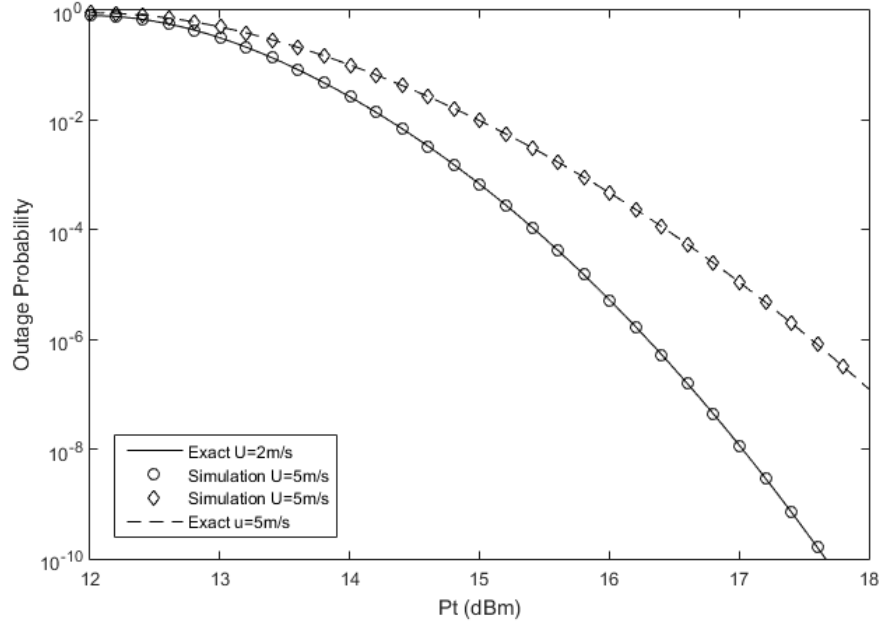

 (a) Coastal water $c = 0.3/m$.

 (b) Harbor water $c = 2.19/m$.

Figure 5.15: Outage probability of a vertical buoy-based UWOC system with zero boresight pointing errors. Link distance $L = 10m$

5.5.2 Outage Probability Bounds with Nonzero Boresight Pointing Errors

In Figure 5.16(a), we plot the exact outage probability with nonzero boresight pointing errors in (5.16) and its bounds in (5.22) and (5.26) respectively. In this case, we let $N = 15$.

In order to show the tightness of the bounds can be improved with the increment of N , we also demonstrate the bounds with $N = 100$ in Figure 5.16(b). From Figure 5.16(b), we observe that the bounds become much tighter than in Figure 5.16(a). When N approaches infinity, the lower and upper bounds of outage probability will converge to the exact outage probability with nonzero boresight pointing errors.

By comparing Figure 5.16 with Figure 5.14(a), we have also found that, the UWOC system with impact of zero boresight pointing errors needs to consume 8dBm transmit power to maintain an outage probability of 10^{-5} . But for the system with the impact of non-zero pointing errors, 10dBm transmit power is needed to maintain the same outage probability of 10^{-5} . This phenomenon indicates that the UWOC system requires higher transmit power to maintain the same outage probability level with the impact of nonzero boresight pointing errors.

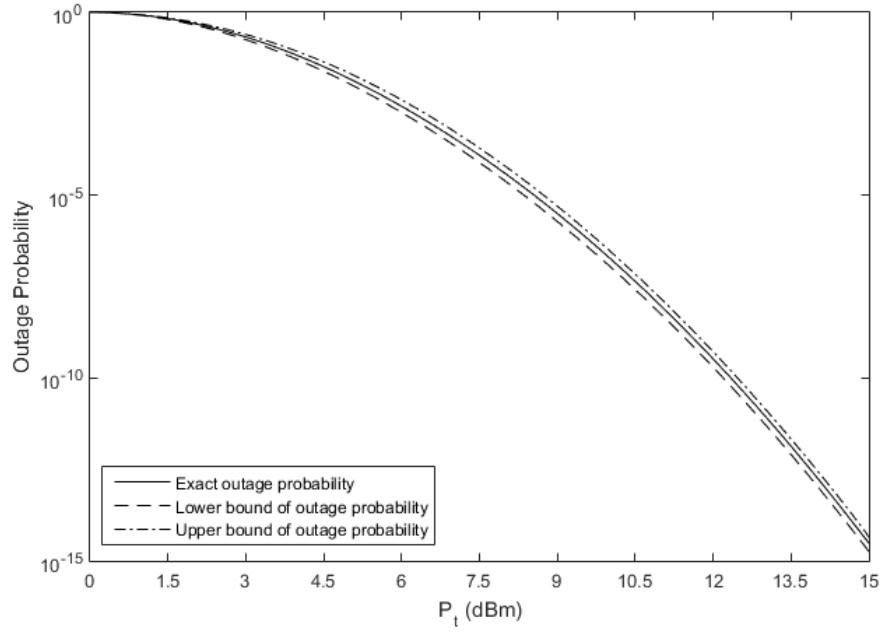
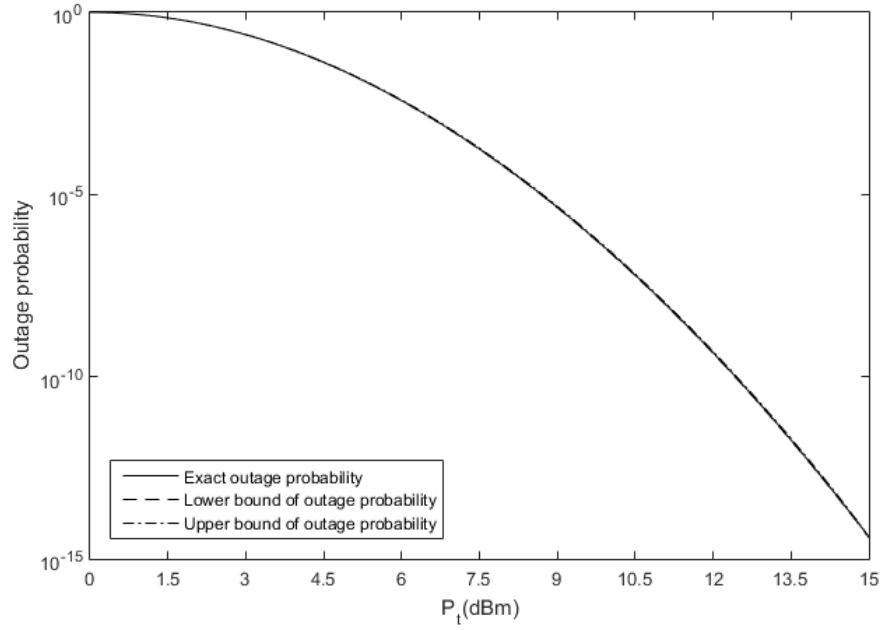

 (a) $N = 15$.

 (b) $N = 100$.

Figure 5.16: Outage probability and its bound with nonzero boresight pointing errors. $\mu_x = 0.01$, $\mu_y = 0.02$, $U = 2m/s$, $c = 0.3m^{-1}$, $L = 5m$, $D = 5cm$, $\gamma_{th} = 0.01$.

5.6 Summary

In this chapter, we introduced the pointing error models for the buoy-based UWOC system. Based on this model, we developed a novel method to derive the outage probability of vertical buoy-based UWOC links using IM/DD OOK. A closed-form expression for the outage probability with zero boresight pointing errors was obtained. We also derived the closed-form bounds of outage probability with nonzero boresight pointing errors. The bounds were proved to converge to the exact outage probability when N approaches infinity. At the end of this chapter, we demonstrated the numerical results of the derived outage performance.

Chapter 6

Conclusions

In this chapter, we conclude the thesis by summarizing the contributions of this work and suggesting some potential further research topics.

6.1 Summary of Contributions

In this thesis, we have provided a comprehensive technical survey for the research of UWOC. This survey covers three comprehensive aspects of the state-of-the-art of UWOC research in the perspective of communication engineering: UWOC channel modeling, modulation and coding technologies, and experimental UWOC discoveries. The summarization that we've made can provide a comprehensive overview of UWOC as well as potential research directions for the scholars and engineers who are working on this area. In order to conclude the thesis, we will summarize the contributions as follows:

- In Chapter 1, we have introduced the history and current development of UWOC. Several significant discoveries of UWOC have been stated. We have also carried out four link configurations that are widely implemented in UWOC systems: point-to-point LOS, diffused LOS, retroreflector-based LOS and NLOS configurations. The corresponding characterizations and application scenarios of each link configurations have also been explained. In the second part of this chapter, we have introduced the advantages and limitations of UWOC by comparing it with other conventional UWC carriers such as acoustic and RF waves.
- Chapter 2 has investigated the channel modeling of UWOC. We have firstly introduced several basic properties of light propagation in water which provide a foundation for UWOC channel modeling. The concept of absorption and scattering coefficients as well as their characterizations in different water types have been stated. Secondly, we have presented the modeling work of aquatic optical attenuation in LOS and NLOS configurations. Several UWOC channel modeling approaches that include analytical and numerical solutions of RTE, stochastics

modeling of aquatic optical attenuation have been introduced. Finally, we have demonstrated the modeling of link misalignment and turbulence in UWOC. A summary of each UWOC channel modeling work has been given at the end of this Chapter.

- In Chapter 3, we have studied the channel modulation and coding techniques that applied in UWOC. Several conventional intensity modulation schemes such as OOK, PPM, DPIM and their applications in UWOC systems have been presented. We have also presented the implementations of both simple and complex error correction codes in UWOC. The characterization and performance of each codes in UWOC system have also been presented.
- Chapter 4 has demonstrated the recent progress of UWOC experimental research. Firstly, we have explained the architecture of a typical LOS UWOC experimental system. The recent research works based on this architecture have been introduced. We have also presented the UWOC experimental demonstrations with other link configurations such as diffused LOS and NLOS. Secondly, we have discussed several popular topics of experimental UWOC research which include retroreflector, smart transceivers, UWOC for underwater vehicles and hybrid UWOC systems. The recent progress in each of these topics has been presented in details. Finally, we have summarized the literatures of experimental UWOC in recent years.
- Chapter 5 has studied the outage performance of vertical buoy-based UWOC links using IM/DD OOK with zero and nonzero boresight pointing errors. Firstly, we have introduced the pointing error models with zero and nonzero boresight. Secondly, we have introduced the beam spread function which describes the propagation of light in underwater environment. Thirdly, we have analyzed the outage probability with zero and nonzero boresight pointing errors. A closed-form outage probability with zero boresight pointing errors has been achieved. We have also derived the closed-form outage probability bounds with nonzero boresight pointing errors. These bounds can be made arbitrarily tight and approach the exact outage probability.

6.2 Suggested Future Work

Although considerable research work on UWOC have already been proposed during the past few years, large scale commercial applications of UWOC systems have not been realized so far. There are still several challenges in this technology that need to be overcome. According to the previous survey and investigation of UWOC systems, we provide several potential directions for

future UWOC research as follows:

- On the aspect of UWOC channel modeling, although lots of modeling work focusing on the horizontal LOS configuration have been demonstrated, few channel models have considered the vertical link. Compared with horizontal link configuration, vertical links take into account the variations of refractive index with the depth and temperature, which is a challenging task for future UWOC research. In FSO communications, there are a lot of works considering channel turbulence. However, in UWOC research, turbulence of water has not been fully considered. Another issue is to derive an accurate model for the NLOS UWOC. The modeling of LOS UWOC are relatively mature, several close-to-reality models have already been demonstrated. But for NLOS UWOC, such accurate models have not been proposed so far.
- There are also several potential research directions in the aspect of UWOC transceivers. For most theoretical UWOC research, the impact of transceiver noise to UWOC has not been fully investigated. It's necessary to study the noise model of UWOC transceivers and use them to evaluate the system performance. As we have presented in the previous chapters, link misalignment is an inevitable phenomena. Although a few research works on smart transceivers for overcoming link misalignment have been proposed, considering the rapid growing of UWSNs, there's still a need for developing highly intelligent UWOC transceivers. The next generation UWSNs require high bandwidth, energy-efficient, and compact UWOC transceivers to be large-scaly implemented in AUVs, ROVs, and underwater sensor nodes. Thus, there's huge research potential for developing more advanced and low-cost transmission light sources, receiving devices, as well as energy preservation system for the next-generation UWSNs.
- The design of appropriate modulation and coding schemes that can adapt the characterizations of underwater environment is another potential research direction. In recent years, researchers have implemented almost all the conventional optical modulation and coding techniques in UWOC. These schemes have been proved useful and improved the system performance. However, few implementations have considered to design a modulation or coding scheme that can dynamically adapt to the link characterization. Since most UWOC systems are embedded on a battery-powered platform, the energy efficiency is thus considered to be important. If there is a mechanism can adaptively switch modulation and coding schemes according to the turbidity of water (applying simple weak error coding scheme in clear water, complex powerful error coding scheme in turbid water), then the system will save considerable energy and have

longer cruising time.

- Suitable network protocols are also needed for the UWOC. To this end, most of the research work on UWOC are mainly focusing on the physical layer such as channel modeling, modulation and channel coding. Only few studies on UWOC networks have been demonstrated so far [176, 177]. Considering the unique characterization of wireless optical channel in underwater environment, novel efficient network protocols need to be proposed.
- In Chapter 5, we have derived the closed form bounds of Beckmann CDF. But a closed-form bounds or approximation of Beckmann PDF have not been proposed. Therefore, a future research topic is to develop accurate closed-form approximation or bounds of Beckmann PDF. These approximation and bounds can be used to analyze BER performance of vertical buoy-based UWOC system with boresight pointing errors.

Bibliography

- [1] X. Che, I. Wells, G. Dickers, P. Kear, and X. Gong, “Re-evaluation of RF electromagnetic communication in underwater sensor networks,” *IEEE Communications Magazine*, vol. 48, pp. 143–151, Dec. 2010. → pages vi, 7, 10
- [2] N. G. Jerlov, *Marine Optics*. New York: Elsevier Scientific Publishing, 1976. → pages vi, 14, 18
- [3] T. Jacobson, “Phys104,” 2008. [Online]. Available: <http://www.physics.umd.edu/grt/taj/104a/104anotessupps.html> → pages vii, 3
- [4] D. Pompili and I. F. Akyildiz, “Overview of networking protocols for underwater wireless communications,” *IEEE Communications Magazine*, vol. 47, pp. 97–102, Jan. 2009. → pages vii, 2, 4, 7, 8
- [5] C. D. Mobley, *Light and Water: Radiative Transfer in Natural Waters*. San Diego, CA: Academic press, 1994. → pages vii, 12, 13, 14, 15, 18, 19, 23
- [6] D. Anguita, D. Brizzolara, G. Parodi, and Q. Hu, “Optical wireless underwater communication for auv: Preliminary simulation and experimental results,” in *Proc. MTS/IEEE OCEANS (OCEANS’11)*, Santander, Spain, Jun. 2011, pp. 1–5. → pages vii, 16, 17, 48, 53
- [7] M. A. Chancey, *Short Range Underwater Optical Communication Links*. North Carolina State University: M.S. Thesis, 2005. → pages 41, 53
- [8] J. A. Simpson, *A 1 Mbps Underwater Communications System using LEDs and Photodiodes with Signal Processing Capability*. North Carolina State University: M.S. Thesis, 2007. → pages vii, 16, 17, 41, 53
- [9] C. Gabriel, M. Khalighi, S. Bourennane, P. Léon, and V. Rigaud, “Investigation of suitable modulation techniques for underwater wireless optical communication,” in *Proc. International*

- Workshop on Optical Wireless Communications (IWOW'12)*, Pisa, Italy, Oct. 2012, pp. 1–3.
→ pages vii, 32, 34, 35, 38
- [10] Y. Dong, S. Tang, and X. Zhang, “Effect of random sea surface on downlink underwater wireless optical communications,” *IEEE Communications Letters*, vol. 17, pp. 2164–2167, Nov. 2013. → pages vii, 25, 27, 30, 57, 58, 62, 70
- [11] B. M. Cochenour, L. J. Mullen, and A. E. Laux, “Characterization of the beam-spread function for underwater wireless optical communications links,” *IEEE Journal of Oceanic Engineering*, vol. 33, pp. 513–521, Oct. 2008. → pages viii, 18, 21, 23, 26, 27, 30, 60, 61, 70
- [12] A. G. Bell, “On the production and reproduction of sound by light,” *American Journal of Sciences*, vol. 3, pp. 305–324, Oct. 1880. → pages 1
- [13] D. Killinger, “Free space optics for laser communication through the air,” *Optics & Photonics News*, vol. 13, pp. 36–42, Oct. 2002. → pages 1
- [14] B. A. Lengyel, *Lasers: Generation of Light by Stimulated Emission*. London, UK: Wiley, 1962. → pages 1
- [15] S. Q. Duntley, “Light in the sea,” *Journal of the Optical Society of America A*, vol. 53, pp. 214–233, Feb. 1963. → pages 1, 8
- [16] G. Gilbert, T. Stoner, and J. Jernigan, “Underwater experiments on the polarization, coherence, and scattering properties of a pulsed blue-green laser,” in *Proc. Underwater Photo Optics I*, vol. 7, Santa Barbara, USA, Jan. 1966, p. 3. → pages 1
- [17] S. Karp, “Optical communications between underwater and above surface (satellite) terminals,” *IEEE Transactions on Communications*, vol. 24, pp. 66–81, Jan. 1976. → pages 2
- [18] M. Callahan, “Submarine communications,” *IEEE Communications Magazine*, vol. 19, pp. 16–25, Nov. 1981. → pages 2
- [19] J. Puschell, R. Giannaris, and L. Stotts, “The autonomous data optical relay experiment: first two way laser communication between an aircraft and submarine,” in *Proc. National Telesystems Conference (NTC'92)*, Washington, DC, May 1992, pp. 14/27–14/30. → pages 2

- [20] T. Wiener and S. Karp, “The role of blue/green laser systems in strategic submarine communications,” *IEEE Transactions on Communications*, vol. 28, pp. 1602–1607, Sep. 1980. → pages 2
- [21] M.-A. Khalighi, C. Gabriel, T. Hamza, S. Bourennane, P. Leon, and V. Rigaud, “Underwater wireless optical communication; recent advances and remaining challenges,” in *Proc. 16th International Conference on Transparent Optical Networks (ICTON’14)*, Jul. 2014, pp. 1–4. → pages 2
- [22] L. J. Johnson, F. Jasman, R. J. Green, and M. S. Leeson, “Recent advances in underwater optical wireless communications,” *Underwater Technology*, vol. 32, pp. 167–175, Nov. 2014. → pages 2, 6, 12, 28
- [23] S. Arnon, “Underwater optical wireless communication network,” *Optical Engineering*, vol. 49, pp. 015 001–1, Jan. 2010. → pages 6, 25
- [24] S. Arnon and D. Kedar, “Non-line-of-sight underwater optical wireless communication network,” *Journal of Optical Society of America A*, vol. 26, pp. 530–539, Jan. 2009. → pages 6, 25, 30
- [25] S. Tang, Y. Dong, and X. Zhang, “On path loss of NLOS underwater wireless optical communication links,” in *Proc. MTS/IEEE OCEANS (OCEANS’13)*, Bergen, Norway, Jun. 2013, pp. 1–3. → pages 6, 25, 30
- [26] B. Truax, *Acoustic Communication*. Santa Barbara, CA: Greenwood Publishing Group, 2001. → pages 7
- [27] E. M. Sozer, M. Stojanovic, and J. G. Proakis, “Underwater acoustic networks,” *IEEE Journal of Oceanic Engineering*, vol. 25, pp. 72–83, Jan. 2000. → pages 7
- [28] J. Partan, J. Kurose, and B. N. Levine, “A survey of practical issues in underwater networks,” *ACM SIGMOBILE Mobile Computing and Communications Review*, vol. 11, pp. 23–33, Sep. 2007. → pages 7
- [29] W. W. Au, P. E. Nachtigall, and J. L. Pawloski, “Acoustic effects of the atoc signal (75 hz, 195 db) on dolphins and whales,” *The Journal of the Acoustical Society of America*, vol. 101, pp. 2973–2977, Jan. 1997. → pages 7

- [30] L. J. Johnson, R. J. Green, and M. S. Leeson, "Underwater optical wireless communications: depth dependent variations in attenuation," *Applied Optics*, vol. 52, pp. 7867–7873, Oct. 2013.
→ pages 8, 19, 26, 27, 30
- [31] R. W. Spinrad, K. L. Carder, and M. J. Perry, *Ocean Optics*. Oxford: Clarendon Press, 1994. → pages 12
- [32] A. Morel and H. Loisel, "Apparent optical properties of oceanic water: dependence on the molecular scattering contribution," *Applied Optics*, vol. 37, no. 21, pp. 4765–4776, Jul. 1998.
→ pages
- [33] H. R. Gordon, O. B. Brown, and M. M. Jacobs, "Computed relationships between the inherent and apparent optical properties of a flat homogeneous ocean," *Applied Optics*, vol. 14, pp. 417–427, Feb. 1975. → pages
- [34] R. E. Green and H. M. Sosik, "Analysis of apparent optical properties and ocean color models using measurements of seawater constituents in new england continental shelf surface waters," *Journal of Geophysical Research: Oceans (1978–2012)*, vol. 109, Mar. 2004. → pages 12
- [35] L. Johnson, R. Green, and M. Leeson, "A survey of channel models for underwater optical wireless communication," in *Proc. 2nd International Workshop on Optical Wireless Communications (IWOW'13)*, Newcastle upon Tyne, UK, Oct. 2013, pp. 1–5. → pages 13, 21
- [36] C. Mobley, E. Boss, and C. Roesler, "Ocean optics web book," 2010. [Online]. Available: <http://www.oceanopticsbook.info/> → pages 14, 19, 21, 30
- [37] C. Gabriel, M. Khalighi, S. Bourennane, P. Leon, and V. Rigaud, "Channel modeling for underwater optical communication," in *Proc. IEEE Global Communications Conference (GLOBECOM'11)*, Houston, TX, Dec. 2011, pp. 833–837. → pages 14, 18, 19, 20, 22, 30
- [38] K. Shifrin, *Physical Optics of Ocean Water*. New York: American Institute of Physics, 1988.
→ pages 14
- [39] R. C. Smith and K. S. Baker, "Optical properties of the clearest natural waters (200–800 nm)," *Applied Optics*, vol. 20, pp. 177–184, Jan. 1981. → pages 14
- [40] A. Bricaud, A. Morel, and L. Prieur, "Absorption by dissolved organic matter of the sea (yellow substance) in the uv and visible domains," *Limnology and Oceanography*, vol. 26, pp. 43–53, Jan. 1981. → pages 14

- [41] W. Breves and R. Reuter, “Bio-optical properties of gelbstoff in the arabian sea at the onset of the southwest monsoon,” *Journal of Earth System Science*, vol. 109, pp. 415–425, Dec. 2000. → pages 14
- [42] V. I. Haltrin, “Chlorophyll-based model of seawater optical properties,” *Applied Optics*, vol. 38, pp. 6826–6832, Nov. 1999. → pages 15, 30
- [43] D. A. Hansell and C. A. Carlson, *Biogeochemistry of Marine Dissolved Organic Matter*. San Diego, CA: Academic Press, 2014. → pages 15
- [44] J. R. Apel, *Principles of Ocean Physics*. London, UK: Academic Press, 1987. → pages 15, 19
- [45] M. Kishino, N. Okami, M. Takahashi, and S.-e. Ichimura, “Light utilization efficiency and quantum yield of phytoplankton in a thermally stratified sea,” *Limnology and Oceanography*, vol. 31, pp. 557–566, Dec. 1986. → pages 15
- [46] C. D. Mobley, B. Gentili, H. R. Gordon, Z. Jin, G. W. Kattawar, A. Morel, P. Reinersman, K. Stamnes, and R. H. Stavn, “Comparison of numerical models for computing underwater light fields,” *Applied Optics*, vol. 32, pp. 7484–7504, Dec. 1993. → pages 18, 21, 23, 30
- [47] F. Hanson and S. Radic, “High bandwidth underwater optical communication,” *Applied Optics*, vol. 47, pp. 277–283, Jan. 2008. → pages 18, 22, 30
- [48] A. L. Alldredge and M. W. Silver, “Characteristics, dynamics and significance of marine snow,” *Progress in Oceanography*, vol. 20, pp. 41–82, Apr. 1988. → pages 19
- [49] L. J. Johnson, R. J. Green, and M. S. Leeson, “Underwater optical wireless communications: depth-dependent beam refraction,” *Applied Optics*, vol. 53, pp. 7273–7277, Oct. 2014. → pages 19, 27, 30
- [50] C. Gabriel, M.-A. Khalighi, S. Bourennane, P. Léon, and V. Rigaud, “Monte-carlo-based channel characterization for underwater optical communication systems,” *IEEE/OSA Journal of Optical Communications and Networking*, vol. 5, pp. 1–12, Jan. 2013. → pages 20, 22, 30, 60
- [51] W. Cox and J. Muth, “Simulating channel losses in an underwater optical communication system,” *Journal of the Optical Society of America A*, vol. 31, pp. 920–934, May 2014. → pages 23, 30

- [52] D. Toubhanc, “Henyeey-greenstein and mie phase functions in monte carlo radiative transfer computations,” *Applied Optics*, vol. 35, pp. 3270–3274, Jun. 1996. → pages
- [53] V. I. Haltrin, “One-parameter two-term henyeey-greenstein phase function for light scattering in seawater,” *Applied Optics*, vol. 41, pp. 1022–1028, Feb. 2002. → pages 30
- [54] —, “Two-term henyeey-greenstein light scattering phase function for seawater,” in *Proc. IEEE International Geoscience and Remote Sensing Symposium (IGARSS’99)*, Hamburg, Germany, Jun. 1999, pp. 1423–1425. → pages 20
- [55] J. Smart, “Underwater optical communications systems part 1: variability of water optical parameters,” in *Proc. IEEE Military Communications Conference (MILCOM’05)*, Atlantic City, NJ, Oct. 2005, pp. 1140–1146. → pages 20, 30
- [56] J. W. Giles and I. N. Bankman, “Underwater optical communications systems. part 2: basic design considerations,” in *Proc. IEEE Military Communications Conference (MILCOM’05)*, Atlantic City, NJ, Oct. 2005, pp. 1700–1705. → pages 20, 30
- [57] H. Tan, R. Doerffer, T. Oishi, A. Tanaka *et al.*, “A new approach to measure the volume scattering function,” *Optics Express*, vol. 21, pp. 18 697–18 711, Aug. 2013. → pages 20
- [58] S. Arnon, J. Barry, G. Karagiannidis, R. Schober, and M. Uysal, *Advanced Optical Wireless Communication Systems*, New York, 2012. → pages 21, 30
- [59] C. Li, K.-H. Park, and M.-S. Alouini, “A direct radiative transfer equation solver for path loss calculation of underwater optical wireless channels,” CEMSE division, KAUST, Thuwal, Saudi Arabia, Tech. Rep. 333892, May 2014. → pages 21, 23, 30
- [60] —, “On the use of a direct radiative transfer equation solver for path loss calculation in underwater optical wireless channels,” *IEEE Communications Letters*, 2015, accepted for publication. → pages 21, 23
- [61] H. C. Van de Hulst, *Multiple Light Scattering: Tables, Formulas, and Applications*. New York: Academic Press, 2012. → pages 21, 30
- [62] S. Jaruwatanadilok, “Underwater wireless optical communication channel modeling and performance evaluation using vector radiative transfer theory,” *IEEE Journal on Selected Areas in Communications*, vol. 26, pp. 1620–1627, Dec. 2008. → pages 21, 33, 38

- [63] B. Cochenour, L. Mullen, and A. Laux, "Spatial and temporal dispersion in high bandwidth underwater laser communication links," in *Proc. IEEE Military Communications Conference (MILCOM'08)*, San Diego, CA, Nov. 2008, pp. 1–7. → pages 21, 30, 42, 53
- [64] J. Potter *et al.*, "Ucomms: A conference and workshop on underwater communications, channel modeling, and validation," *IEEE Journal of Oceanic Engineering*, vol. 38, pp. 603–613, Oct. 2013. → pages 21, 24
- [65] L. Wang, S. L. Jacques, and L. Zheng, "Monte carlo modeling of light transport in multi-layered tissues," *Computer Methods and Programs in Biomedicine*, vol. 47, pp. 131–146, Jul. 1995. → pages 21, 30
- [66] R. M. Lerner and J. D. Summers, "Monte carlo description of time- and space-resolved multiple forward scatter in natural water." *Applied Optics*, vol. 21, pp. 861–869, Mar. 1982. → pages 21
- [67] R. A. Leathers, T. V. Downes, C. O. Davis, and C. D. Mobley, "Monte carlo radiative transfer simulations for ocean optics: a practical guide," Naval Research Laboratory, Washington, DC, Tech. Rep. NRL/MR/5660–04-8819, Sep. 2004. → pages 21, 30
- [68] J. Li, Y. Ma, Q. Zhou, B. Zhou, and H. Wang, "Monte carlo study on pulse response of underwater optical channel," *Optical Engineering*, vol. 51, pp. 066 001–1, Jun. 2012. → pages 22, 30
- [69] J. Li, Y. Ma, Q. Zhou, H. Wang, and B. Zhou, "Channel capacity study of underwater wireless optical communications links based on monte carlo simulation," *Journal of Optics*, vol. 14, p. 015403, Dec. 2011. → pages 22, 30
- [70] F. R. Dalglish, F. M. Caimi, A. K. Vuorenkoski, W. B. Britton, B. Ramos, T. E. Giddings, J. J. Shirron, and C. H. Mazel, "Efficient laser pulse dispersion codes for turbid undersea imaging and communications applications," *Proceedings of SPIE*, vol. 7678, pp. 76 780I–76 780I, Apr. 2010. → pages 22, 30, 41
- [71] B. Edouard, *Multiple Scattering of Light in Optical Diagnostics of Dense Sprays and Other Complex Turbid Media*. Cranfield University: Ph.D Thesis, 2006. → pages 23
- [72] W. Cox, "Photonator," 2012. [Online]. Available: <https://github.com/gallamine/Photonator> → pages 23, 30

- [73] H. Zhang, Y. Dong, and X. Zhang, "On stochastic model for underwater wireless optical links," in *Proc. IEEE/CIC International Conference on Communications in China (ICCC'14)*, Shanghai, China, Oct. 2014, pp. 156–160. → pages 23, 24, 30
- [74] H. Zhang and Y. Dong, "General stochastic channel model and performance evaluation for underwater wireless optical links," *IEEE Transactions on Communications*, 2015, accepted for publication. → pages 23, 24
- [75] H. Zhang, L. Hui, and Y. Dong, "Angle of arrival analysis for underwater wireless optical links," *IEEE Communications Letters*, 2015, accepted for publication. → pages 24
- [76] S. Tang, X. Zhang, and Y. Dong, "On impulse response for underwater wireless optical links," in *Proc. MTS/IEEE OCEANS (OCEANS'13)*, Bergen, Norway, Jun. 2013, pp. 1–4. → pages 24, 30
- [77] S. Tang, Y. Dong, and X. Zhang, "Impulse response modeling for underwater wireless optical communication links," *IEEE Transactions on Communications*, vol. 62, pp. 226–234, Jan. 2014. → pages 24, 30
- [78] Y. Dong, H. Zhang, and X. Zhang, "On impulse response modeling for underwater wireless optical mimo links," in *Proc. 2014 IEEE/CIC International Conference on Communications in China (ICCC'14)*, Shanghai, China, Oct. 2014, pp. 151–155. → pages 24, 30
- [79] M. Doniec, M. Angermann, and D. Rus, "An end-to-end signal strength model for underwater optical communications," *IEEE Journal of Oceanic Engineering*, vol. 38, pp. 743–757, Oct 2013. → pages 24, 25, 30, 36, 38, 42, 53
- [80] C. Cox and W. Munk, "Slopes of the sea surface deduced from photographs of sun glitter," Tech. Rep., Sep. 1956. → pages 25, 30
- [81] W. J. Plant, "A new interpretation of sea-surface slope probability density functions," *Journal of Geophysical Research: Oceans*, vol. 108, pp. 111–113, Sep. 2003. → pages 25, 30
- [82] A. Choudhary, V. Jagadeesh, and P. Muthuchidambaranathan, "Pathloss analysis of nlos underwater wireless optical communication channel," in *Proc. International Conference on Electronics and Communication Systems (ICECS'14)*, Coimbatore, India, Feb. 2014, pp. 1–4. → pages 25

- [83] A. Choudhary, F. M. Bui, and P. Muthuchidambaranathan, “Characterization of channel impulse responses for nlos underwater wireless optical communications,” in *Proc. Fourth International Conference on Advances in Computing and Communications (ICACC’2014)*, Kochi, India, Aug. 2014, pp. 77–79. → pages 25, 30
- [84] S. Tang, Y. Dong, and X. Zhang, “On link misalignment for underwater wireless optical communications,” *IEEE Communications Letters*, vol. 16, pp. 1688–1690, Oct. 2012. → pages 26, 27, 30
- [85] B. Cochenour, L. Mullen, and J. Muth, “Temporal response of the underwater optical channel for high-bandwidth wireless laser communications,” *IEEE Journal of Oceanic Engineering*, vol. 38, pp. 730–742, Oct. 2013. → pages 27, 30, 42, 53
- [86] H. Zhang, L. Hui, and Y. Dong, “On capacity of downlink underwater wireless optical mimo systems with random sea surface,” *IEEE Communications Letters*, 2015, accepted for publication. → pages 27
- [87] C. Gabriel, M.-A. Khalighi, S. Bourennane, P. Léon, and V. Rigaud, “Misalignment considerations in point-to-point underwater wireless optical links,” in *Proc. MTS/IEEE OCEANS (OCEANS’13)*, Bergen, Norway, Jun. 2013, pp. 1–5. → pages 27, 30
- [88] L. J. Johnson, R. J. Green, and M. S. Leeson, “The impact of link orientation in underwater optical wireless communication systems,” in *Proc. MTS/IEEE OCEANS (OCEANS’14)*, St. John’s, NL, Sep. 2014, pp. 1–8. → pages 28, 30
- [89] F. Hanson and M. Lasher, “Effects of underwater turbulence on laser beam propagation and coupling into single-mode optical fiber,” *Applied Optics*, vol. 49, pp. 3224–3230, May 2010. → pages 28, 30
- [90] W. Liu, Z. Xu, and L. Yang, “Simo detection schemes for underwater optical wireless communication under turbulence,” *Photonics Research*, vol. 3, pp. 48–53, Jun. 2015. → pages 28
- [91] S. Tang, X. Zhang, and Y. Dong, “Temporal statistics of irradiance in moving turbulent ocean,” in *Proc. MTS/IEEE OCEANS (OCEANS’13)*, Bergen, Norway, Jun. 2013, pp. 1–4. → pages 28, 29

- [92] V. Nikishov and V. Nikishov, "Spectrum of turbulent fluctuations of the sea-water refraction index," *International Journal of Fluid Mechanics Research*, vol. 27, pp. 82–98, Nov. 2000. → pages 28
- [93] O. Korotkova, N. Farwell, and E. Shchepakina, "Light scintillation in oceanic turbulence," *Waves in Random and Complex Media*, vol. 22, pp. 260–266, Feb. 2012. → pages 28, 30
- [94] A. Laux, R. Billmers, L. Mullen, B. Concannon, J. Davis, J. Prentice, and V. Contarino, "The a, b, cs of oceanographic lidar predictions: a significant step toward closing the loop between theory and experiment," *Journal of Modern Optics*, vol. 49, pp. 439–451, Mar. 2002. → pages 30, 40
- [95] N. Fair, A. Chave, L. Freitag, J. Preisig, S. White, D. Yoerger, and F. Sonnichsen, "Optical modem technology for seafloor observatories," in *Proc. MTS/IEEE OCEANS (OCEANS'06)*, Boston, MA, Sep. 2006, pp. 1–6. → pages 30, 42, 53
- [96] W. Liu, D. Zou, P. Wang, Z. Xu, and L. Yang, "Wavelength dependent channel characterization for underwater optical wireless communications," in *IEEE International Conference on Signal Processing, Communications and Computing (ICSPCC'14)*, Guilin, China, Aug. 2014, pp. 895–899. → pages 30
- [97] W. Liu, D. Zou, Z. Xu, and J. Yu, "Non-line-of-sight scattering channel modeling for underwater optical wireless communication," in *IEEE International Conference on Cyber Technology in Automation, Control, and Intelligent Systems (CYBER'2015)*, Shenyang, China, Jun. 2015, pp. 1265–1268. → pages 30
- [98] M. Khalighi and M. Uysal, "Survey on free space optical communication: A communication theory perspective," *IEEE Communications Surveys and Tutorials*, vol. 16, pp. 2231–2258, Apr. 2014. → pages 33, 34, 35, 37, 39, 40, 41, 48
- [99] F. Akhoundi, J. Salehi, A. Tashakori *et al.*, "Cellular underwater wireless optical cdma network: Performance analysis and implementation concepts," *IEEE Transactions on Communications*, vol. 63, pp. 882–891, Feb. 2015. → pages 33, 38, 42, 53
- [100] Z. Ahmad and R. Green, "Link design for multi-hop underwater optical wireless sensor network," in *Proc. 7th International Conference on Systems and Networks Communications (IC-SNC'12)*, Lisbon, Portugal, Nov. 2012, pp. 65–70. → pages 33, 38, 42, 53

- [101] X. He and J. Yan, "Study on performance of M-ary PPM underwater optical communication systems using vector radiative transfer theory," in *Proc. 10th International Symposium on Antennas, Propagation & EM Theory (ISAPE'12)*, Xian, China, Oct. 2012, pp. 566–570. → pages 33, 38
- [102] S. Meihong, Y. Xinsheng, and Z. Zhangguo, "The modified ppm modulation for underwater wireless optical communication," in *Proc. International Conference on Communication Software and Networks, (ICCSN'09)*, Macau, China, Feb. 2009, pp. 173–177. → pages 33
- [103] H. Sari and B. Woodward, "Underwater voice communications using a modulated laser beam," in *Proc. MTS/IEEE OCEANS (OCEANS'98)*, Nice, France, Oct. 1998, pp. 1183–1188. → pages 33, 42, 53
- [104] M. Chen, S. Zhou, and T. Li, "The implementation of ppm in underwater laser communication system," in *Proc. International Conference on Communications, Circuits and Systems (ICCCAS'06)*, Guilin, China, Jun. 2006, pp. 1901–1903. → pages
- [105] D. Anguita, D. Brizzolara, and G. Parodi, "Vhdl modeling of phy and mac layer modules for underwater optical wireless communication," in *Proc. 5th European Conference on Circuits and Systems for Communications (ECCSC'2010)*, Belgrade, Serbia, Nov. 2010, pp. 185–188. → pages 41, 53
- [106] D. Anguita, D. Brizzolara, and G. Parodi, "Optical wireless communication for underwater wireless sensor networks: Hardware modules and circuits design and implementation," in *Proc. MTS/IEEE OCEANS (OCEANS'10)*, Seattle, WA, Sep. 2010, pp. 1–8. → pages 36, 38, 41, 53
- [107] S. Tang, Y. Dong, and X. Zhang, "Receiver design for underwater wireless optical communication link based on apd," in *Proc. 8th International Conference on Communications and Networking in China (CHINACOM'13)*, Kunming, China, Aug. 2012, pp. 301–305. → pages 46, 53
- [108] P. Swathi and S. Prince, "Designing issues in design of underwater wireless optical communication system," in *Proc. International Conference on Communications and Signal Processing (ICCSP'14)*, Melmaruvathur, India, Apr. 2014, pp. 1440–1445. → pages 34, 42, 53

- [109] R. M. Hagem, D. V. Thiel, S. G. O’Keefe, and T. Fickenscher, “Optical wireless communication for real time swimmers feedback: A review,” in *Proc. International Symposium on Communications and Information Technologies (ISCIT’12)*, Gold Coast, QLD, Oct. 2012, pp. 1080–1085. → pages 33, 38, 41
- [110] M. Doniec, I. Vasilescu, M. Chitre, C. Detweiler, M. Hoffmann-Kuhnt, and D. Rus, “Aquaoptical: A lightweight device for high-rate long-range underwater point-to-point communication,” in *Proc. MTS/IEEE OCEANS (OCEANS’09)*, Biloxi, MS, Oct. 2009, pp. 1–6. → pages 34, 38, 42
- [111] M. Doniec and D. Rus, “Bidirectional optical communication with aquaoptical ii,” in *Proc. IEEE International Conference on Communication Systems (ICCS’10)*, Singapor, Nov. 2010, pp. 390–394. → pages 42, 53
- [112] M. Doniec, C. Detweiler, I. Vasilescu, and D. Rus, “Using optical communication for remote underwater robot operation,” in *Proc. IEEE/RSJ International Conference on Intelligent Robots and Systems (IROS’10)*, Taipei, China, Oct. 2010, pp. 4017–4022. → pages 34, 38, 48, 53
- [113] Z. Wang, Y. Dong, X. Zhang, and S. Tang, “Adaptive modulation schemes for underwater wireless optical communication systems,” in *Proc. 7th ACM International Conference on Underwater Networks and Systems (WUWNet’12)*. → pages 34, 38
- [114] B. Cochenour, L. Mullen, and A. Laux, “Phase coherent digital communications for wireless optical links in turbid underwater environments,” in *Proc. MTS/IEEE OCEANS (OCEANS’07)*, Vancouver, BC, Canada, Sep. 2007, pp. 1–5. → pages 34, 38
- [115] M. Sui, X. Yu, and F. Zhang, “The evaluation of modulation techniques for underwater wireless optical communications,” in *Proc. International Conference on Communication Software and Networks (ICCSN’09)*, Macau, China, Feb. 2009, pp. 138–142. → pages 34, 38
- [116] W. C. Cox, B. L. Hughes, and J. F. Muth, “A polarization shift-keying system for underwater optical communications,” in *Proc. MTS/IEEE OCEANS (OCEANS’09)*, Biloxi, MS, Oct. 2009, pp. 1–4. → pages 35, 38
- [117] Y. Dong, T. Zhang, and X. Zhang, “Polarized pulse position modulation for wireless optical

- communications,” in *Proc. 47th Annual Conference on Information Sciences and Systems (CISS’13)*, Baltimore, MD, Mar. 2013, pp. 1–5. → pages 35
- [118] X. Zhang, Y. Dong, and S. Tang, “Polarization differential pulse position modulation,” in *Proc. 7th ACM International Conference on Underwater Networks and Systems (WUWNet’12)*, Los Angeles, CA, Nov. 2012, pp. 41:1–41:2. → pages 35, 38
- [119] W. C. Cox, J. A. Simpson, and J. F. Muth, “Underwater optical communication using software defined radio over led and laser based links,” in *Proc. IEEE Military Communications Conference (MILCOM’11)*, Baltimore, MD, Nov. 2011, pp. 2057–2062. → pages 35, 38, 42, 53
- [120] G. Cossu, R. Corsini, A. Khalid, S. Balestrino, A. Coppelli, A. Caiti, and E. Ciaramella, “Experimental demonstration of high speed underwater visible light communications,” in *Proc. 2nd International Workshop on Optical Wireless Communications (IWOW’13)*, Newcastle upon Tyne, UK, Oct. 2013, pp. 11–15. → pages 35, 36, 38, 41, 53
- [121] J. G. Proakis and M. Salehi, *Digital Communications*, 5th ed. New York: McGraw-Hill, 2007. → pages 36
- [122] W. C. Cox, J. A. Simpson, C. P. Domizioli, J. F. Muth, and B. L. Hughes, “An underwater optical communication system implementing reed-solomon channel coding,” in *Proc. MT-S/IEEE OCEANS (OCEANS’08)*, Quebec City, QC, Canada, Sep. 2008, pp. 1–6. → pages 36
- [123] J. A. Simpson, W. C. Cox, J. R. Krier, B. Cochenour, B. Hughes, and J. Muth, “5 mbps optical wireless communication with error correction coding for underwater sensor nodes,” in *Proc. MTS/IEEE OCEANS (OCEANS’10)*, Seattle, WA, pp. 6–9. → pages 36
- [124] W.-P. Wang and B. Zheng, “The simulation design of led-based close-range underwater optical communication system,” in *Proc. 10th International Computer Conference on Wavelet Active Media Technology and Information Processing (ICCWAMTIP’13)*, Chengdu, China, Dec. 2013, pp. 283–285. → pages 36, 38, 41, 53
- [125] M. Doniec, A. Xu, and D. Rus, “Robust real-time underwater digital video streaming using optical communication,” in *Proc. IEEE International Conference on Robotics and Automation (ICRA)’13*, Karlsruhe, Germany, May 2013, pp. 5117–5124. → pages 36, 38, 42, 53

- [126] J. Everett, *Forward-Error Correction Coding for Underwater Free-space Optical Communication*. North Carolina State University: M.S. Thesis, 2009. → pages 37, 38
- [127] W. C. Cox, K. F. Gray, J. A. Simpson, B. Cochenour, B. L. Hughes, and J. F. Muth, “A mems blue/green retroreflecting modulator for underwater optical communications,” in *Proc. MTS/IEEE OCEANS (OCEANS’10)*, Seattle, WA, USA, Sep. 2010, pp. 1–4. → pages 38, 40, 45, 53
- [128] M. Sun, B. Zheng, L. Zhao, X. Zhao, and F. Kong, “A design of the video transmission based on the underwater laser communication,” in *Proc. MTS/IEEE OCEANS (OCEANS’14)*, St. John’s, NL, Sep. 2014, pp. 1–4. → pages 41, 43, 53
- [129] L. Mullen, A. Laux, and B. Cochenour, “Time-dependent underwater optical propagation measurements using modulated light fields,” in *SPIE Defense, Security, and Sensing*. International Society for Optics and Photonics, 2009, pp. 73 170D–73 170D. → pages
- [130] —, “Propagation of modulated light in water: implications for imaging and communications systems,” *Applied Optics*, vol. 48, pp. 2607–2612, Apr. 2009. → pages
- [131] F. Schill, U. R. Zimmer, and J. Trumpf, “Visible spectrum optical communication and distance sensing for underwater applications,” in *Proc. Australasian Conference on Robotics and Automation (ACRA’04)*, Canberry, Australia, Dec. 2004, pp. 1–8. → pages 41, 53
- [132] R. M. Hagem, S. G. O’Keefe, T. Fickenscher, and D. V. Thiel, “Self contained adaptable optical wireless communications system for stroke rate during swimming,” *IEEE Sensors Journal*, vol. 13, pp. 3144–3151, Aug. 2013. → pages 41
- [133] H. Brundage, *Designing a Wireless Underwater Optical Communication System*. Massachusetts Institute of Technology: M.S. Thesis, 2010. → pages 41
- [134] A. Destrez, Z. Toffano, and P. Leon, “Underwater high bit-rate optical free-space communication system,” in *Proc. International Workshop on Optical Wireless Communications (IWOW’12)*, Pisa, Italy, Oct. 2012, pp. 1–3. → pages 42, 53
- [135] J. B. Snow, J. P. Flatley, D. E. Freeman, M. A. Landry, C. E. Lindstrom, J. R. Longacre, and J. A. Schwartz, “Underwater propagation of high-data-rate laser communications pulses,” *Proceedings of SPIE*, vol. 1750, pp. 419–427, Jul. 1992. → pages 42, 53

- [136] W. C. Cox Jr, *A 1 Mbps Underwater Communication System Using a 405 nm Laser Diode and Photomultiplier Tube*. North Carolina State University: M.S. Thesis, 2008. → pages 42
- [137] P. A. Hiskett and R. A. Lamb, “Underwater optical communications with a single photon-counting system,” *Proceedings of SPIE*, vol. 9114, pp. 91 140P–91 140P–15, May 2014. → pages 43
- [138] I. Mizukoshi, N. Kazuhiko, and M. Hanawa, “Underwater optical wireless transmission of 405nm, 968mbit/s optical im/dd-ofdm signals,” in *Proc. OptoElectronics and Communication Conference and Australian Conference on Optical Fibre Technology (OECC/ACOFT’14)*, Melbourne, VIC, Australia, Jul. 2014, pp. 216–217. → pages 43
- [139] J. A. Simpson, B. L. Hughes, J. F. Muth *et al.*, “A spatial diversity system to measure optical fading in an underwater communications channel,” in *Proc. MTS/IEEE OCEANS (OCEANS’09)*, Biloxi, MS, Oct. 2009, pp. 1–6. → pages
- [140] G. Baiden, Y. Bissiri, and A. Masoti, “Paving the way for a future underwater omni-directional wireless optical communication systems,” *Ocean Engineering*, vol. 36, pp. 633–640, Jul. 2009. → pages
- [141] B. M. Cochenour, *Experimental Measurements of Temporal Dispersion for Underwater Laser Communications and Imaging*. North Carolina State University: Ph.D. Thesis, 2013. → pages 43, 53
- [142] C. Pontbriand, N. Farr, J. Ware, J. Preisig, and H. Popenoe, “Diffuse high-bandwidth optical communications,” in *Proc. MTS/IEEE OCEANS (OCEANS’08)*, Quebec City, QC, Canada, Sep. 2008, pp. 1–4. → pages 43, 46, 53
- [143] B. Cochenour and L. Mullen, “Channel response measurements for diffuse non-line-of-sight (n-los) optical communication links underwater,” in *Proc. MTS/IEEE OCEANS (OCEANS’11)*, Waikoloa, HI, Sep. 2011, pp. 1–5. → pages 43, 53
- [144] D. Alley, L. Mullen, and A. Laux, “Compact, dual-wavelength, non-line-of-sight (nlos) underwater imager,” in *Proc. MTS/IEEE OCEANS (OCEANS’11)*, Santander, Spain, Jun. 2011, pp. 1–5. → pages 43, 53

- [145] B. Cochenour, L. Mullen, and J. Muth, “A modulated pulse laser for underwater detection, ranging, imaging, and communications,” *Proceedings of SPIE*, vol. 8372, pp. 83 720S–1–83 720S–10, Jun. 2012. → pages 43, 53
- [146] P. G. Goetz, W. S. Rabinovich, R. Mahon, M. S. Ferraro, J. L. Murphy, H. Burris, M. Stell, C. I. Moore, M. R. Suite, W. Freeman *et al.*, “Modulating retro-reflector devices and current link performance at the naval research laboratory,” in *Proc. IEEE Military Communications Conference (MILCOM’07)*, Orlando, FL, USA, Oct. 2007, pp. 1–7. → pages 43, 45
- [147] W. S. Rabinovich, R. Mahon, H. R. Burris, G. C. Gilbreath, P. G. Goetz, C. I. Moore, M. Stell, M. J. Vilcheck, J. L. Witkowski, L. Swingen *et al.*, “Free-space optical communications link at 1550 nm using multiple-quantum-well modulating retroreflectors in a marine environment,” *Optical Engineering*, vol. 44, pp. 056 001–056 001, May 2005. → pages 44
- [148] P. G. Goetz, W. S. Rabinovich, R. Mahon, J. L. Murphy, M. S. Ferraro, M. Suite, W. R. Smith, H. R. Burris, C. I. Moore, W. W. Schultz *et al.*, “Modulating retro-reflector lasercom systems for small unmanned vehicles,” *IEEE Journal on Selected Areas in Communications*, vol. 30, pp. 986–992, Jun. 2012. → pages 45
- [149] P. G. Goetz, W. S. Rabinovich, R. Mahon, J. L. Murphy, M. S. Ferraro, M. Suite, W. Smith, B. Xu, H. Burris, C. Moore *et al.*, “Modulating retro-reflector lasercom systems at the naval research laboratory,” in *Proc. IEEE Military Communications Conference (MILCOM’10)*, San Jose, CA, Oct. 2010, pp. 1601–1606. → pages 45
- [150] L. Mullen, B. Cochenour, W. Rabinovich, R. Mahon, and J. Muth, “Backscatter suppression for underwater modulating retroreflector links using polarization discrimination,” *Applied Optics*, vol. 48, pp. 328–337, Jan. 2009. → pages 45, 53
- [151] B. Cochenour, L. Mullen, W. Rabinovich, and R. Mahon, “Underwater optical communications with a modulating retro-reflector,” *Proceedings of SPIE*, vol. 7317, pp. 73 170G–73 170G, Apr. 2009. → pages 45, 53
- [152] J. Simpson, B. L. Hughes, J. F. Muth *et al.*, “Smart transmitters and receivers for underwater free-space optical communication,” *IEEE Journal on Selected Areas in Communications*, vol. 30, pp. 964–974, Jun. 2012. → pages 46, 53

- [153] H. Yoshida, T. Aoki, H. Osawa, S. Tsukioka, S. Ishibashi, Y. Watanabe, J. Tahara, T. Miyazaki, T. Hyakudome, T. Sawa *et al.*, “Newly-developed devices for the two types of underwater vehicles,” in *Proc. MTS/IEEE OCEANS (OCEANS’07)*, Aberdeen, UK, Jun. 2007, pp. 1–6. → pages 47
- [154] A. Bowen, D. Yoerger, C. Taylor, R. McCabe, J. Howland, D. Gomez-Ibanez, J. Kinsey, M. Heintz, G. McDonald, D. Peters *et al.*, “The nereus hybrid underwater robotic vehicle,” *Underwater Technology*, vol. 28, pp. 79–89, Jul. 2009. → pages 47
- [155] A. Bowen, D. Yoerger, C. Taylor, R. McCabe, J. Howland, D. Gomez-Ibanez, J. Kinsey, M. Heintz, G. McDonald, D. Peters, J. Bailey, E. Bors, T. Shank, L. Whitcomb, S. Martin, S. Webster, M. Jakuba, B. Fletcher, C. Young, J. Buescher, P. Fryer, and S. Hulme, “Field trials of the nereus hybrid underwater robotic vehicle in the challenger deep of the mariana trench,” in *Proc. MTS/IEEE OCEANS (OCEANS’09)*, Biloxi, MS, Oct 2009, pp. 1–10. → pages 47
- [156] I. Vasilescu, P. Varshavskaya, K. Kotay, and D. Rus, “Autonomous modular optical underwater robot (amour) design, prototype and feasibility study,” in *Proc. IEEE International Conference on Robotics and Automation (ICRA’05)*, Barcelona, Spain, Apr. 2005, pp. 1603–1609. → pages 47, 53
- [157] P. Corke, C. Detweiler, M. Dunbabin, M. Hamilton, D. Rus, and I. Vasilescu, “Experiments with underwater robot localization and tracking,” in *Proc. IEEE International Conference on Robotics and Automation (ICRA’07)*, Roma, Italy, Apr. 2007, pp. 4556–4561. → pages 47
- [158] I. Vasilescu, C. Detweiler, M. Doniec, D. Gurdan, S. Sosnowski, J. Stumpf, and D. Rus, “Amour v: A hovering energy efficient underwater robot capable of dynamic payloads,” *The International Journal of Robotics Research*, vol. 29, pp. 547–570, Apr. 2010. → pages 47
- [159] M. Dunbabin, P. Corke, I. Vasilescu, and D. Rus, “Experiments with cooperative control of underwater robots,” *The International Journal of Robotics Research*, vol. 28, pp. 815–833, Jun. 2009. → pages 47
- [160] M. Dunbabin, J. Roberts, K. Usher, G. Winstanley, and P. Corke, “A hybrid auv design for shallow water reef navigation,” in *Proc. IEEE International Conference on Robotics and Automation (ICRA’05)*, Barcelona, Spain, Apr. 2005, pp. 2105–2110. → pages 48

- [161] M. Doniec, I. Vasilescu, C. Detweiler, and D. Rus, “Complete se 3 underwater robot control with arbitrary thruster configurations,” in *Proc. IEEE International Conference on Robotics and Automation (ICRA’10)*, Anchorage, AK, May 2010, pp. 5295–5301. → pages 48
- [162] B. Tian, F. Zhang, and X. Tan, “Design and development of an led-based optical communication system for autonomous underwater robots,” in *Proc. IEEE/ASME International Conference on Advanced Intelligent Mechatronics (AIM’13)*, Wollongong, Australia, Jul. 2013, pp. 1558–1563. → pages 48
- [163] M. Tabacchiera, S. Betti, and S. Persia, “Underwater optical communications for swarm unmanned vehicle network,” in *Proc. Fotonica AEIT Italian Conference on Photonics Technologies*, Naples, Italy, May 2014, pp. 1–3. → pages 48, 53
- [164] I. Vasilescu, K. Kotay, D. Rus, M. Dunbabin, and P. Corke, “Data collection, storage, and retrieval with an underwater sensor network,” in *Proc. 3rd International Conference on Embedded Networked Sensor Systems*, San Diego, CA, Nov. 2005, pp. 154–165. → pages 48, 49, 53
- [165] M. Dunbabin, P. Corke, I. Vasilescu, and D. Rus, “Data muling over underwater wireless sensor networks using an autonomous underwater vehicle,” in *Proc. IEEE International Conference on Robotics and Automation (ICRA’06)*, Orlando, FL, May 2006, pp. 2091–2098. → pages 48
- [166] I. Vasilescu, C. Detweiler, and D. Rus, “Aquanodes: an underwater sensor network,” in *Proc. The second workshop on Underwater networks (WuWNet’07)*, Montral, Qubec, Canada., Sep. 2007, pp. 85–88. → pages 49
- [167] N. Farr, A. Bowen, J. Ware, C. Pontbriand, and M. Tivey, “An integrated, underwater optical/acoustic communications system,” in *Proc. MTS/IEEE OCEANS (OCEANS’10)*, Sydney, NSW, Australia, May 2010, pp. 1–6. → pages 51
- [168] N. Farr, J. Ware, C. Pontbriand, and M. Tivey, “Demonstration of wireless data harvesting from a subsea node using a ship of opportunity,” in *Proc. MTS/IEEE OCEANS (OCEANS’13)*, San Diego, CA, Sep. 2013, pp. 1–5. → pages 51
- [169] L. J. Johnson, R. J. Green, and M. S. Leeson, “Hybrid underwater optical/acoustic link design,” in *Proc. 16th International Conference on Transparent Optical Networks (ICTON’14)*, Graz, Austria, Jul. 2014, pp. 1–4. → pages 51

- [170] S. Han, Y. Noh, R. Liang, R. S. Chen, Y.-J. Cheng, and M. Gerla, "Evaluation of underwater optical-acoustic hybrid network," *China Communications*, vol. 11, pp. 49–59, May 2014. → pages 51, 53
- [171] A. Lin, W. Lu, J. Xu, H. Song, F. Qu, J. Han, X. Gu, and J. Leng, "Underwater wireless optical communication using a directly modulated semiconductor laser," in *Proc. MTS/IEEE OCEANS (OCEANS'15)*, Genova, Italy, May 2015, pp. 1–4. → pages 53
- [172] F. Yang, J. Cheng, T. Tsiftsis *et al.*, "Free-space optical communication with nonzero boresight pointing errors," *IEEE Transactions on Communications*, vol. 62, pp. 713–725, Feb. 2014. → pages 54, 59, 62
- [173] P. Cheah, D. Fraser, and N. Reid, "Some alternatives to edgeworth," *The Canadian Journal of Statistics*, vol. 5, pp. 131–138, Feb. 1993. → pages 55
- [174] C. Cox and W. Munk, "Measurement of the roughness of the sea surface from photographs of the suns glitter," *Journal of the Optical Society of America*, vol. 44, pp. 838–850, Nov. 1954. → pages 55
- [175] W. Gappmair, S. Hranilovic, and E. Leitgeb, "Ook performance for terrestrial fso links in turbulent atmosphere with pointing errors modeled by hoyt distributions," *IEEE Communications Letters*, vol. 15, pp. 875–877, Aug. 2011. → pages 58
- [176] A. Mora, D. Ganger, G. Wells, J. Zhang, X. Hu, C. Zhou, A. Richa, and C. Youngbull, "Ad-hoc multi-hop underwater optical network for deep ocean monitoring," in *Proc. MTS/IEEE OCEANS (OCEANS'13)*, San Diego, CA, 2013, pp. 1–5. → pages 79
- [177] A. Vavoulas, H. Sandalidis, and D. Varoutas, "Underwater optical wireless networks: A k -connectivity analysis," *IEEE Journal of Oceanic Engineering*, vol. 39, pp. 801–809, Oct. 2014. → pages 79
- [178] I. S. Gradshteyn and I. M. Ryzhik, *Table of Integrals, Series, and Products*, 7th ed. San Diego: Academic Press, 2007. → pages 101
- [179] J. F. Paris, "Nakagami-q (hoyt) distribution function with applications," *Electronics Letters*, vol. 45, pp. 210–211, Feb. 2009. → pages 102

- [180] J. F. Paris and D. Morales-Jimenez, “Outage probability analysis for nakagami-q (hoyt) fading channels under rayleigh interference,” *IEEE Transactions on Wireless Communications*, vol. 9, pp. 1272–1276, Apr. 2010. → pages 102

Appendix

Appendix A

We convert x_a and y_a in (5.5) into polar coordinates as $x_a = r \cos \theta$ and $y_a = r \sin \theta$. Then (5.5) can be expressed as

$$P_r(r, \theta) = \frac{r}{2\pi\sigma_u\sigma_c L^2} \exp\left(-\frac{\sigma_c^2 r^2 \cos^2 \theta + \sigma_u^2 r^2 \sin^2 \theta}{2L^2\sigma_u^2\sigma_c^2}\right). \quad (\text{A.1})$$

Let $\sin^2 \theta = 1 - \cos^2 \theta$ and $q_H = \sigma_c/\sigma_u$, we have

$$P_r(r, \theta) = \frac{r}{2\pi q_H \sigma_u^2 L^2} \exp\left(\frac{r^2 (1 - q_H^2) \cos^2 \theta - r^2}{2q_H^2 \sigma_u^2 L^2}\right). \quad (\text{A.2})$$

Integrating (A.2) with respect to θ , the PDF of r can be expressed as

$$f_r(r) = \int_0^{2\pi} \frac{r}{2\pi q_H \sigma_u^2 L^2} \exp\left(\frac{r^2 (1 - q_H^2) \cos^2 \theta - r^2}{2q_H^2 \sigma_u^2 L^2}\right) d\theta. \quad (\text{A.3})$$

Applying an integral identity [178, Eq. (3.339)] and double-angle formula $\cos^2 \theta = \frac{\cos 2\theta + 1}{2}$ to (A.3), we have

$$f_r(r) = \frac{r}{q_H \sigma_u^2 L^2} \exp\left[-\frac{(1 + q_H^2) r^2}{4q_H^2 \sigma_u^2 L^2}\right] I_0\left(\frac{(1 - q_H^2) r^2}{4q_H^2 \sigma_u^2 L^2}\right). \quad (\text{A.4})$$

Appendix B

In [179] and [180], the PDF of Hoyt fading channel are expressed as

$$f_x(x) = \frac{(1 + q_H^2)x}{q_H \Omega_x} \exp \left[-\frac{(1 + q_H^2)^2 x^2}{4q_H^2 \Omega_x} \right] I_0 \left(\frac{(1 - q_H^4)x^2}{4q_H^2 \Omega_x} \right). \quad (\text{B.1})$$

Based on (B.1), the closed-form CDF of Hoyt distribution has also been given in [179] and [180] as

$$\begin{aligned} F_x(x) = & Q_1 \left(\frac{\sqrt{\frac{1+q_H}{1-q_H}} \sqrt{1 - q_H^4} x}{2q_H \sqrt{\Omega_x}}, \frac{\sqrt{\frac{1-q_H}{1+q_H}} \sqrt{1 - q_H^4} x}{2q_H \sqrt{\Omega_x}} \right) \\ & - Q_1 \left(\frac{\sqrt{\frac{1-q_H}{1+q_H}} \sqrt{1 - q_H^4} x}{2q_H \sqrt{\Omega_x}}, \frac{\sqrt{\frac{1+q_H}{1-q_H}} \sqrt{1 - q_H^4} x}{2q_H \sqrt{\Omega_x}} \right). \end{aligned} \quad (\text{B.2})$$

We substitute $r = \sqrt{1 + q_H^2}x$ in (5.6) and convert (5.6) as

$$f_r(r) = \frac{1}{\sqrt{1 + q_H^2}} \frac{(1 + q_H^2)x}{q_H \sigma_u^2 L^2} \exp \left[-\frac{(1 + q_H^2)^2 x^2}{4q_H^2 \sigma_u^2 L^2} \right] I_0 \left(\frac{(1 - q_H^4)r^2}{4q_H^2 \sigma_u^2 L^2} \right) \quad (\text{B.3})$$

which has the similar form of (B.1). Substitute $\Omega_x = \sigma_u^2 L^2$ and $x = \frac{r}{\sqrt{1+q_H^2}}$ in (B.2), we have the CDF of (5.6) as:

$$\begin{aligned} F_r(r) = & \frac{1}{\sqrt{1 + q_H^2}} \left[Q_1 \left(\frac{\sqrt{\frac{1+q_H}{1-q_H}} \sqrt{1 - q_H^4} r}{2q_H \sqrt{1 + q_H^2} \sigma_u L}, \frac{\sqrt{\frac{1-q_H}{1+q_H}} \sqrt{1 - q_H^4} r}{2q_H \sqrt{1 + q_H^2} \sigma_u L} \right) \right. \\ & \left. - Q_1 \left(\frac{\sqrt{\frac{1-q_H}{1+q_H}} \sqrt{1 - q_H^4} r}{2q_H \sqrt{1 + q_H^2} \sigma_u L}, \frac{\sqrt{\frac{1+q_H}{1-q_H}} \sqrt{1 - q_H^4} r}{2q_H \sqrt{1 + q_H^2} \sigma_u L} \right) \right]. \end{aligned} \quad (\text{B.4})$$

Thus, outage probability with zero boresight pointing errors is

$$\begin{aligned} P_{out,HT} = & 1 - \frac{1}{\sqrt{1 + q_H^2}} \left[Q_1 \left(\frac{\sqrt{\frac{1+q_H}{1-q_H}} \sqrt{1 - q_H^4} P_r^{-1}(\gamma_{th})}{2q_H \sqrt{1 + q_H^2} \sigma_u L}, \frac{\sqrt{\frac{1-q_H}{1+q_H}} \sqrt{1 - q_H^4} P_r^{-1}(\gamma_{th})}{2q_H \sqrt{1 + q_H^2} \sigma_u L} \right) \right. \\ & \left. - Q_1 \left(\frac{\sqrt{\frac{1-q_H}{1+q_H}} \sqrt{1 - q_H^4} P_r^{-1}(\gamma_{th})}{2q_H \sqrt{1 + q_H^2} \sigma_u L}, \frac{\sqrt{\frac{1+q_H}{1-q_H}} \sqrt{1 - q_H^4} P_r^{-1}(\gamma_{th})}{2q_H \sqrt{1 + q_H^2} \sigma_u L} \right) \right]. \end{aligned} \quad (\text{B.5})$$